Effect of Nanoscale Surface Structures on Microbe-Surface Interactions

Zhou Ye

Dissertation submitted to the faculty of the Virginia Polytechnic Institute and State University in partial fulfillment of the requirements for the degree of

Doctor of Philosophy

in

Mechanical Engineering

Chair: Behkam, Bahareh

Co-Chair: Ellis, Michael W.

Mukhopadhyay, Biswarup

Nain, Amrinder S.

von Spakovsky, Michael R.

Blacksburg, VA

February 20, 2017

Keywords: nanopatterning, microbial fuel cell, biophysical model, bacterial adhesion

Effect of Nanoscale Surface Structures on Microbe-Surface Interactions

Zhou Ye

Abstract

Bacteria in nature predominantly grow as biofilms on living and non-living surfaces. The development of biofilms on non-living surfaces is significantly affected by the surface micro/nano topography. The main goal of this dissertation is to study the interaction between microorganisms and nanopatterned surfaces. In order to engineer the surface with well-defined and repeatable nanoscale structures, a new, versatile and scalable nanofabrication method, termed Spun-Wrapped Aligned Nanofiber lithography (SWAN lithography) was developed. This technique enables high throughput fabrication of micro/nano-scale structures on planar and highly non-planar 3D objects with lateral feature size ranging from sub-50 nm to a few microns, which is difficult to achieve by any other method at present. This nanolithography technique was then utilized to fabricate nanostructured electrode surfaces to investigate the role of surface nanostructure size (i.e. 115 nm and 300 nm high) in current production of microbial fuel cells (MFCs). Through comparing the *S. oneidensis* attachment density and current density (normalized by surface area), we demonstrated the effect of the surface feature size which is independent of the effect on the surface area. In order to better understand the mechanism of microorganism adhesion on nanostructured surfaces, we developed a biophysical model that calculates the total energy of adhered cells as a function of nanostructure size and spacing. Using this model, we predict the attachment density trend for *Candida albicans* on nanofiber-textured surfaces. The model can be applied at the population level to design surface nanostructures that reduce cell attachment on medical catheters. The biophysical model was also utilized to study the motion of a single *Candida albicans* yeast cell and to identify the optimal attachment location on nanofiber coated surfaces, thus leading to a better understanding of the cell-substrate interaction upon attachment.

Effect of Nanoscale Surface Structures on Microbe-Surface Interactions

Zhou Ye

General Audience Abstract

Formation of surface associated multicellular communities of microorganisms known as biofilms is of concern in medical settings as well as in industries such as oil refineries and marine engineering. It has been shown that micro/nanoscale surface features can highly regulate the process of biofilm formation and the attached cell activities. In this dissertation, we study the interaction between surface nanoscale structures and bacterial adhesion by experiments and biophysical modelling. We develop the Spun-Wrapped Aligned Nanofiber (SWAN) lithography, a versatile, scalable, and high throughput technique for masterless nanopatterning of hard materials. Using this technique, we demonstrate high fidelity whole surface single step nanopatterning of bulk and thin film surfaces of regularly and irregularly shaped 3D objects. SWAN lithography is used to texturize the electrode surface of microbial fuel cells (MFCs), which are envisioned as an alternative sustainable energy source. Compared to the non-patterned electrodes, the electrodes with 115 nm surface patterns facilitate larger biofilm coverage and 40% higher current production. We also develop a biophysical model to optimally texturize the surface of central venous and uretic medical catheters to prevent biofilm formation by fungal pathogen, *Candida albicans*. We show that the surface structures that result the highest cell total energy retained the least *C. albicans*. Furthermore, the adhesion behaviour of a single yeast cell is also experimentally studied in conjunction with the developed model.

Acknowledgements

Foremost, I would like to sincerely thank my advisors Prof. Bahareh Behkam and Prof. Michael W. Ellis for giving me the opportunity to work in their labs, their constant and relentless support for my Ph.D. work, and their patience, understanding and enthusiasm. I have learned and grown both professionally and personally. I would also like to thank my committee members; Prof. Amrinder Nain deserves special recognition, his advices, encouragements, trainings and relentless support have greatly helped me during my Ph.D. training; Prof. Biswarup Mukhopadhyay and Prof. Michael von Spakovsky deserve many thanks for their helpful discussion, support and encouragement along the way.

I would also like to thank all the members and alumni of the MicroN BASE laboratory, especially Chris Suh, Eric Leaman, Carolyn Mottley, Apratim Mukherjee, Ying Zhan, Carmen Damico, AhRam Kim, Ali Sahari, Mahama Aziz Traore, and Mehdi Kargar for making the lab an enjoyable working place and their support and intellectual input. I also thank the REU undergraduates, Krishan Patel, Lizette Carrasco, Hajar Chokhmane, for their help of the experiments during the summers. I would also like to acknowledge Karthik Radhakrishnan, Jeremy Beach, Bo Chen, Ji Wang, Junbo Hou for their help and discussions during my research. I would like to thank Prof. Alan R. Esker and Candace Wall for their help and meaningful discussions in contact angle measurements and surface energy calculations.

Virginia Tech has been a wonderful place for me to complete my Ph.D. studies. I would like to acknowledge the financial support from Robert E. Hord, Jr. Mechanical Engineering Graduate Fellowship and the Institute of Critical Technology and Applied Sciences (ICTAS) at Virginia

Tech. I would also like to acknowledge the facilities provided by the ECE department cleanroom, NCFL at ICTAS, and the sample preparation room of MSE department. I would specially thank Donald Leber for the microfabrication training and Steve McCartney for SEM and AFM training.

Lastly, I would like to thank my family, especially my parents and wife, for their endless support and love.

Contents

List of figures

List of tables

Nomenclature

E_{tot}	total energy
E_{ad}	adhesion energy
E_{str}	stretching energy
E_c	bending energy
w_{ad}	work of adhesion
A_{ad}	cell-substrate contact surface area
k_{str}	stretching modulus
A	total surface area of the stretched cell
A_0	original cell surface area
Y	average Young's modulus of the cell wall
h	average cell wall thickness
γ_{SL}	solid-liquid surface energy
γ_{SV}	solid-vapor surface energy
γ_{LV}	liquid-vapor surface energy
γ^d	dispersive component of surface energy
γ^p	polar component of surface energy
$\boldsymbol{D_{cell}}$	cell diameter
$\boldsymbol{D_{fiber}}$	fiber diameter
$\boldsymbol{S}$	fiber edge-to-edge spacing
Δx	distance between the cell centroid and the fiber centerline
$\boldsymbol{D_{crit}}$	critical cell diameter
$E_{tot}(flat)$	total energy of a cell attached on flat surfaces

$\overline{E_{tot}}$	average total energy
Π	ratio of stretching modulus by work of adhesion
$\boldsymbol{\delta}$	distance between the cell center and the fiber spacing center

Chapter 1: Introduction

1.1 Motivation and problem statement

In the natural environment, most microorganisms exist as biofilms attached to surfaces. A biofilm is an adherent community of cells and their self-produced matrix of extracellular polymeric substances (EPS), which is composed of polysaccharides, proteins, nucleic acids and lipids[1]. EPS can help cells to attach and aggregate on the surfaces. Biofilms can protect cells from unfavorable environmental factors (e.g. high shear force, disinfectants, and antibiotics)[2]. In nature, food industries and hospitals, biofilms comprised of pathogens can cause infections, illnesses and even death. However, many microorganisms are beneficial to the natural environment and human society. They can remove toxins in water and soil, degrade organic matter from dead plants and animals, and aid digestion in the human body. Some bacteria can also form biofilms on electrode surfaces, which can generate electricity and treat wastewater in microbial fuel cells (MFC) and generate hydrogen or methane from organic matter in microbial electrolysis cells (MEC).

Biofilm formation is a complex process including several steps[3] (Figure 1.1) and cell-to-cell signaling[4]. This process will inevitably be affected by the physical chemistry of the attached surface, hydrodynamics and composition of the aqueous medium, and the physiology and geometries of the cells[5]. Bacteria usually attach more rapidly to hydrophobic (e.g. polystyrene, polyethylene) and nonpolar surfaces than to hydrophilic materials (e.g. glass and polyethylene oxide). A surface will inevitably be conditioned or coated by macromolecules from the aqueous

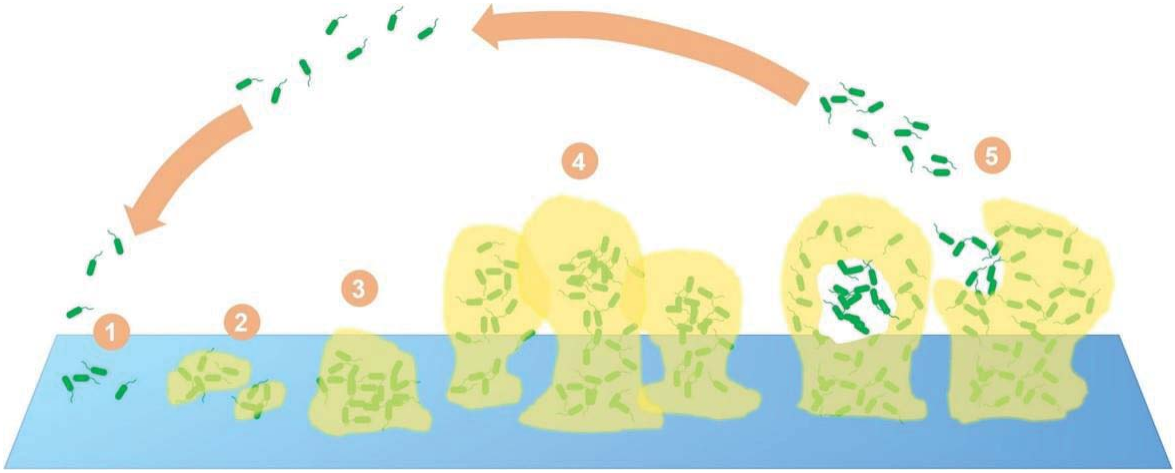

Figure 1. 1 Steps of biofilm formation, including (1) bacterial attachment to a surface, (2) microcolony formation, (3) (4) biofilm maturation, (5) bacterial dispersal.

medium, which will affect the attachment of bacteria as well. Besides the surface chemistry, the roughness and topography of the surface also highly affect the biofilm and the constituent cells.

Micro and nanoscale topographies of the surface can affect the biofilm formation in many respects, including the cell attachment density, biofilm 3D structures, morphology of cells, and genomic and proteomic expressions of cells. An understanding of the role of surface topography in biofilm formation can facilitate the design of optimum surface architectures to prevent pathogenic biofilms or to support beneficial biofilms. However, a complete understanding of the effect of the nanostructure geometry, size and configuration on the single cell attachment and the biofilm formation is lacking. This research is focused on improving the understanding of the role of nanostructure characteristics on biofilm formation through four main **objectives**:

1) **Developing a new multiscale fabrication technique to engineer surfaces with micro and nanoscale features to include:**
    - Fabrication of micro/nanostructures on glassy carbon.
    - Fabrication of micro/nanostructures on thin gold films.

- Characterizations of this new nanolithography method.

2) **Understanding the effect of micro and nanoscale topography on *Shewanella oneidensis* attachment and current production on the surface of a MFC anode to include:**
    - Design, fabrication and characterization of glassy carbon electrodes (GCE) with different surface topographies.
    - Experimental characterization of the current production from *Shewanella oneidensis* on different GCEs in a half-cell.
    - Investigation of the relationship between bacterial attachment density and current production.
3) **Developing a biophysical model for adhesion of the fungal pathogen *Candida albicans* on nanofiber-textured surfaces to include:**
    - Development of the model and governing equations.
    - Evaluation of the model by experiments on polystyrene (PS) sheets textured by PS fibers.
    - Evaluation of the model by experiments on medical catheters textured by PS fibers.
4) **Investigating the applicability of the biophysical model to the description of the motion of a single *Candida albicans* yeast on nanofiber-textured surfaces:**
    - Study of the motion of a yeast cell on one nanofiber and the underlying substrate.
    - Study of the motion of a yeast cell on two nanofibers and the underlying substrate.
    - Study of the motion of a UV-treated yeast cell.

1.2 Background

1.2.1 Bacterial adhesion and biofilm formation on surfaces with micro/nano topographies

A rough surface is usually thought to be more favorable for bacterial attachment and biofilm formation, since it has more surface area and can shelter bacteria from unfavorable environments. The desired roughness, R_a, (characterized by the arithmetic average of the absolute values of the profile height deviations from the mean line) for hygienic surfaces is usually less than 1 μm (e.g. desired R_a for stainless steel is 0.8 μm or less)[6]. However, roughness does not fully represent the surface topographies. For example, three engineered surfaces shown in Figure 1.2 have the same roughness, but they have significantly different topographies and might also show differences in microorganism attachment. Furthermore, sizes and shapes of the engineered features (e.g. linear features, pits, pillars, or more complex shapes) and the geometries of the microorganisms (e.g. cocci, bacilli, or spiral) also have an influence on the cell attachment. Prior work has shown that features or the spacing of features that are significantly larger than the microorganism sizes will have little effect on their retention[7]. For features with similar sizes to the microorganisms, the shape of the features and the geometry of the cells both influence the microbial-surface interaction. Verran *et al.* coated a thin uniform titanium layer (1 μm thick) on the top of unwritten compact discs (CD) and digital video discs (DVD) with linear features of widths of 0.52 μm and 1.02 μm[8]. Coccal cells (*Staphylococcus sciuri*) had significantly higher retention on the 1.02 μm feature surfaces, but rod-shaped cells (*Listeria monocytogenes*) were retained significantly more on the 0.52 μm feature surfaces. On the other hand, Whitehead *et al.* fabricated pits with diameters of 0.2, 0.5, 1 and 2 μm and with depths of 0.2, 0.5, 0.75 and 1 μm respectively[9]. When pits (instead of linear features) were used as the surface pattern, coccal cells (*Staphylococcus aureus*; 1 μm in

diameter) and rod-shaped cells (*Pseudomonas aeruginosa*; 1 μm in diameter × 3 μm in length) showed similar retention on these patterns with different feature sizes. Both coccal cells and rod-shaped cells were retained the most on 2 μm pits. Previous work from our lab deposited aligned nanofibers on a flat surface to study the attachment of rod-shaped cell *Pseudomonas aeruginosa*, and found that the minimum attachment density occurred when the fiber diameter was comparable to the bacteria diameter and the edge-to-edge spacing of fibers was smaller than the bacteria diameter[10]. Other micro-patterns have been designed to explore biofilm formation on engineered surfaces, including Sharklet AF™ topography[11], periodic pillars[12,13], and colloidal crystals[14]. Most of these studies attributed the difference in microorganism attachment to the changing of available cell attachment surface area by these micro topographies.

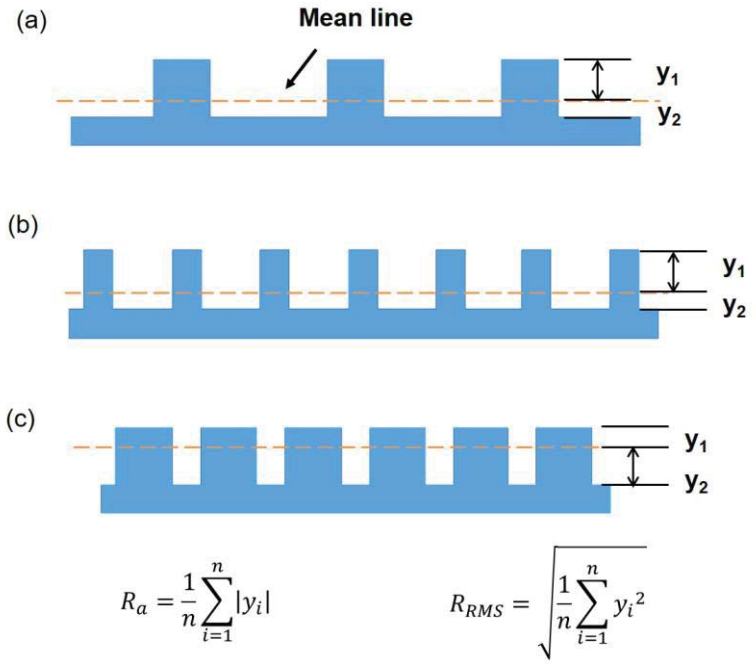

Figure 1. 2 Three different surface patterns with the same surface roughness.

However, even when the surface pattern size is much smaller than the bacterial sizes and the surface area is negligibly changed, biofilm formation is still significantly affected by the surface topography. Singh *et al.* studied the formation of biofilms on TiO_2 nanoparticles coated films with root-mean-square roughness (R_q) of 16.2, 21.7, 25.5 and 32.2 nm[15]. Neither the highest nor the lowest roughness, but the 21.7 nm roughness retained the maximum number of both *Escherichia coli* and *Staphylococcus aureus*. In addition, some nanotopographies not only affect the attachment of the microorganism, but also can effectively kill bacteria. For example, nanopillars on the surface of cicada wings (200 nm tall, 100 nm in diameter at the base) are able to kill *Pseudomonas aeruginosa* within about 3 minutes. This bactericidal activity was not from the surface chemistry, because a coating of thin gold film did not reduce the efficiency of this bactericidal ability[16,17].

1.2.2 Bacterial morphology and gene expression modified by surface topography

Surface topography not only affects biofilm formation, but also affects the single cell morphology, proliferation rate and gene expression. Mitik-Dineva *et al.* found that bacteria on glass substrates with different nanoscale roughness showed changes in cell morphologies and EPS production, which indicated a change in cellular metabolic activity[18]. They compared bacterial attachment on as-received glass (R_a = 2.1 nm) and etched glass (R_a = 1.3 nm), and found that the number of bacteria adhering to the etched glass increased by a factor of three. The size (length and diameter) of the bacteria on etched glass is also larger than that on as-received glass, and more EPS was observed on etched glass by confocal scanning laser microscope (CSLM). This phenomenon of changing of cell morphologies and EPS production by surface nanoscale roughness was also observed by Díaz *et al.*[19]. Furthermore, the shapes and sizes of the nanoscale features are also important for the alteration of cellular morphologies, even with similar nanoscale roughness. Circular wells, thin rectangular wells, and wide rectangular wells yielded different bacterial

lengths and diameters, different numbers of appendages, and different appendage lengths and thicknesses in the study by Hsu *et al*[20]. Nanoscale roughness can also highly affect the genomic and proteomic expressions of *E. coli*[21]. Type-1 fimbriae disappeared in *E. coli* when adherent to gold nanostructured substrates, which was due to the genetic variation of the fimbrial operon regulation. Different expression levels of proteins involved in biosynthesis, peptide transport, metabolic pathway, and DNA repair system were also observed.

1.3 Organization of this dissertation

The overall goal of this research is to quantitatively study the effect of the nanostructure geometry, size and spacing on the biofilm development by **(1)** engineering surface topography using a versatile and scalable nanofabrication method, **(2)** studying the relationship between the electrode biofilm formation and the electrode surface topography in a MFC, and **(3)** developing a biophysical model to explain the topography effect. We invented a new nanofabrication method termed Spun-Wrapped Aligned Nanofiber (SWAN) lithography, which can pattern 3D objects in a single lithography step. Electrode surfaces were textured by SWAN lithography and were used to explore the effect of topography on electrode biofilm formation. Furthermore, we explored the nanofiber-*Candida albicans* yeast interaction through the development of a biophysical model. Consistent with these tasks, the remainder of this document is organized as follows:

Chapter 2:

In this chapter, we describe a versatile nanofabrication method that patterns nanostructures of sub 50 nm to a few microns on both planar and nonplanar 3D objects. Aligned nanofibers with uniform diameter and spacing were deposited on the substrate as a mask by the non-eletrospinning STEP

technique [22,23]. The contact surface area between the nanofiber mask and the substrate was controlled by a solvent vapor treatment process. The nanopattern was transferred from the mask to the substrate by etching. This simple nanofabrication method offers a high throughput (>10^{-7} m^2/s) and low capital cost (<$50,000) and can be operated in standard laboratory settings. This technique can contribute in the fields of photonics, plasmonics, electronics, and biotechnology. This work was published in *Nanoscale* **8**, 12780-12786, 2016.

Chapter 3:

Glassy carbon (GC) electrodes were fabricated and nanopatterned by SWAN lithography. A three-electrode system was implemented to study the biofilm formation of *Shewanella oneidensis* on the nanopatterned and smooth electrode surfaces. Current production was monitored at a constant potential, which indicated the electron transport from bacteria to the electrode surface. Biofilm coverage was characterized by quantitative colony plate, fluorescent microscopy, and scanning electron microscopy. This work was published in *J. Power Sources* **347**, 270-276, 2017.

Chapter 4:

A biophysical model that focuses on minimizing the energy in the adhered state was developed to study the adhesion of the model human pathogen *Candida albicans* on nanofiber-textured surfaces. The total energy of a yeast cell was composed by adhesion energy and stretching energy, which was dependent on the adhesion interaction between the cell and the substrate as well as the cell wall property. The model was validated by the attachment density of *C. albicans* yeasts on polystyrene (PS) fiber-textured PS sheets. The application of this model was also validated by the cell attachment on PS fiber-textured medical catheters.

Chapter 5:

In this chapter, we report an observed phenomenon of the directional motion of *C. albicans* yeasts on nanofiber-textured surface. From the biophysical model described in Chapter 5, the equilibrium adhesion location of the cell is the location with the lowest total energy. This process was found to be a biologically driven behavior since the UV-treated cell distributed equally in every adhesion location.

Chapter 6:

The original contributions of this Ph.D. dissertation are summarized and concluding remarks are presented in this chapter. Future directions towards completion and development of this research are also described in this chapter.

Chapter 2: Spun-wrapped Aligned Nanofiber Lithography (SWAN) for Fabrication of Micro/Nano-Structures on 3D Objects

2.1 Abstract

Fabrication of micro/nano-structures on irregularly shaped substrates and three-dimensional (3D) objects is of significant interest in diverse technological fields. However, it remains a formidable challenge thwarted by limited adaptability of the state-of-the-art nanolithography techniques for nanofabrication on non-planar surfaces. In this work, we introduce Spun-Wrapped Aligned Nanofiber (SWAN) lithography, a versatile, scalable, and cost-effective technique for fabrication of multiscale (nano to microscale) structures on 3D objects without restriction on substrate material and geometry. SWAN lithography combines precise deposition of polymeric nanofiber masks, in aligned single or multilayer configurations, with well-controlled solvent vapor treatment and etching processes to enable high throughput ($>10^{-7}$ m^2/s) and large-area fabrication of sub-50 nm to several micron features with high pattern fidelity. Using this technique, we demonstrate whole-surface nanopatterning of bulk and thin film surfaces of cubes, cylinders, and hyperbola-shaped objects that would be difficult, if not impossible to achieve with existing methods. We demonstrate that the fabricated feature size (b) scales with the fiber mask diameter (D) as $b^{1.5} \propto D$. This scaling law is in excellent agreement with theoretical predictions using the Johnson, Kendall, and Roberts (JKR) contact theory, thus providing a rational design framework for fabrication of systems and devices that require precisely designed multiscale features.

This work was published in *Nanoscale* **8**, 12780-12786, 2016.

2.2 Introduction

High-throughput, scalable, and cost-effective fabrication of micro/nano-structures on three-dimensional (3D) objects is crucial for the development of new paradigms in diverse fields including metamaterials,[24] optoelectronics,[25] nanophotonics and plasmonics,[26,27] biosensing,[28,29] lab-on-fiber technologies,[30] energy harvesting and storage.[31] There is also a great need for fabricating nanostructures on the surface of biomedical devices and implants where micro/nanoscale surface features have been shown to promote tissue regeneration[32] and inhibit microbial fouling.[10] As such, numerous attempts have been made to develop new techniques[33–36] and also adapt the conventional nanofabrication techniques such as electron beam lithography (EBL)[37,38] and soft lithography[33,34,39–44] for nanofabrication on non-planar surfaces. Despite the many positive attributes of these techniques, the high sensitivity of pattern fidelity to overall 3D object shape and limitations with respect to throughput, scalability, reliability, affordability, and substrate material compatibility present significant barriers to their use for nanopatterning of large-areas of pre-structured 3D objects. Presently, to the best of our knowledge, there is no method capable of whole surface nanopatterning of irregularly shaped or highly non-planar 3D objects. Furthermore, simultaneous fabrication of multiscale (i.e. micro- and nanoscale) structures on 3D substrates remains a formidable challenge thwarted by limited affordability and scalability of the aforementioned state-of-the-art techniques. Thus, there is a compelling need to develop new nanoscale as well as multiscale fabrication technologies.

Here, we report a versatile and scalable technique, termed Spun-Wrapped Aligned Nanofiber (SWAN) lithography, for fabrication of multiscale structures on large areas of

planar and non-planar substrates without a master and at high-throughput in standard laboratory setting. The process flow of SWAN lithography is illustrated in Fig. 2.1. In the first step, the non-electrospinning Spinneret-based Tunable Engineered Parameters (STEP) technique[22,23] was used to deposit polystyrene (PS) fibers with precisely controlled diameter, spacing and orientation onto a 3D substrate. The nanofiber mask is deposited in an array of uniform diameter fibers at a constant or a prescribed varying spacing. Multiple arrays each with different diameter and spacing may be deposited in one layer or in a 3D multi-layer configuration (Fig. 2.1a). In the second step, the fiber-masked substrate was placed under vacuum in an enclosure containing tetrahydrofuran (THF, a good PS solvent) vapor to carry out a controlled fiber deformation process and achieve the desired fiber-substrate contact area. In the third step, the substrate was etched to transfer the fiber mask pattern onto the substrate. In the final step, the PS fiber mask was dissolved. SWAN lithography is applicable to both bulk and thin film patterning; thus enabling incorporation of passive (e.g. nanostructures for controlling cell behavior on implants) or functional devices (e.g. electronic circuity for sensing) onto curved surfaces and 3D objects.

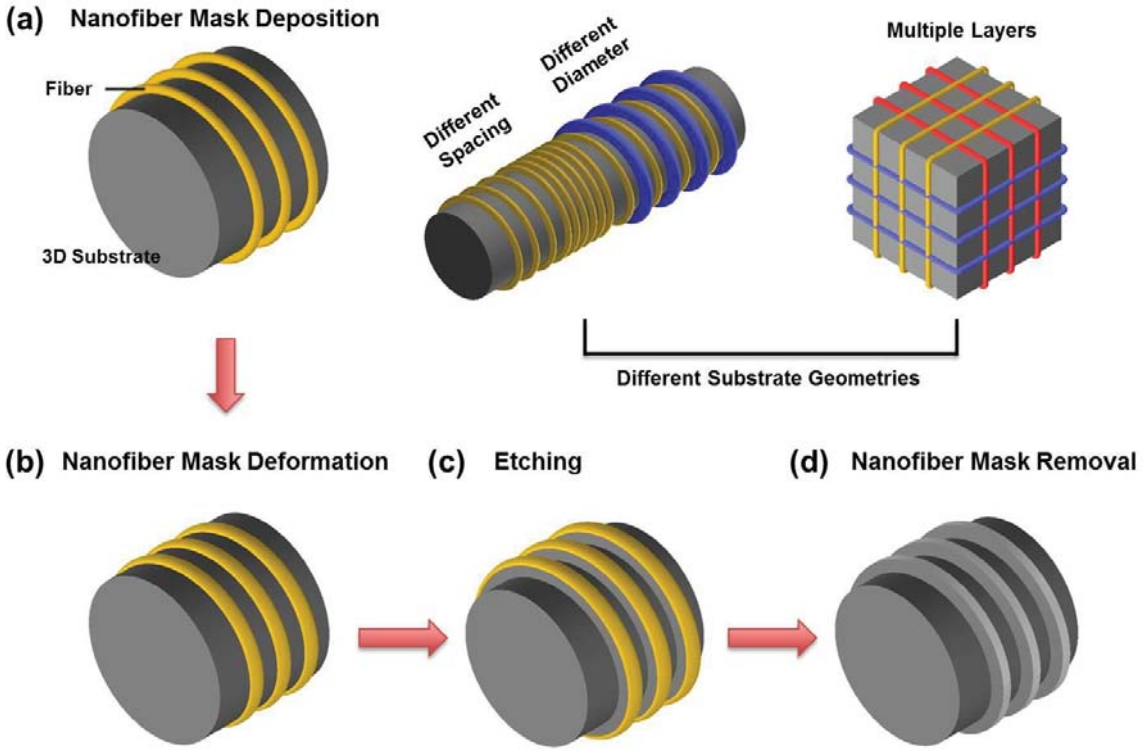

Figure 2. 1 Schematic illustration of SWAN lithography. a) High throughput continuous deposition of PS fibers on a 3D substrate using the STEP technique. Fiber mask arrays can be deposited in single or multiple layers of the same or different diameter and spacing. b) Exposure of the fiber-masked substrate to the solvent vapor for controlled deformation of the fiber mask. c) Etching of the fiber-masked substrate to create micro/nanostructures. d) Removal of the fiber mask in PS solvent.

.

2.3 Experimental section

2.3.1 Nanopatterning of glassy carbon (GC) substrates

All experiments were performed at room temperature unless otherwise stated. A total of six PS solutions were prepared by dissolving PS (Scientific Polymer Products) in xylene (Fisher Scientific) at 10 wt% for PS of 860K g mol^{-1} molecular weight, and at 5 wt%, 7 wt%, 10 wt%, 14 wt%, and 18 wt% for PS of 2,000K g mol^{-1} molecular weight. Fiber arrays were deposited on GC SIGARADUR® (Hochtemperatur-Werkstoffe GmbH, Germany) plates (10 mm × 10 mm × 1

mm), cylinders (Ø3 mm × 5 mm), and cubes (6 mm × 6 mm × 6 mm) using the STEP technique [23]. Briefly, PS solution was pumped through a glass micropipette to form an extruded droplet at the pipette tip. The droplet was brought into contact with the substrate to form a fiber, and aligned fibers were continuously wrapped around the rotating substrate. The substrate was moved using a 3D motorized stage to form the fiber mask pattern with controlled fiber spacing. The fiber-masked substrate was placed in an enclosure containing THF under a vacuum pressure of -0.68 bar. After exposure to THF vapor for the specified duration, the sample was electrochemically etched at 2.0 V (vs. Ag/AgCl) in 0.1 M NaOH solution with Platinum gauze connected to a platinum wire as the counter electrode [45]. After etching, PS fibers were dissolved in methylene chloride, and GC substrate was treated in piranha solution (3:1 H_2SO_4 and H_2O_2) for 30 min to remove the PS residue. After each use, the GC plates were serially polished by 1 µm, 0.3 µm, and 0.05 µm alumina slurry (Electron Microscopy Sciences) to remove etched features for the subsequent set of experiments. The scratches appearing in some of the SEM and AFM images (Fig. 2.5, 2.6) were from polishing. After polishing, the resulting surface roughness was 5.1±0.4 nm.

2.3.2 Nanopatterning of gold film

A borosilicate glass rod (Ø5 mm) was pulled to a hyperbola shape on an open flame. The hyperbola-shaped glass was cleaned in piranha solution for 30 min, followed by rinsing with deionized water and flushing with dry air. The glass sample was further dried at 180 °C for 30 min. A thin Ti (adhesive promoter) and Au film were sequentially deposited onto the glass sample by electron beam evaporation (Kurt J. Lesker PVD-250). To achieve uniform evaporated gold thickness, the glass substrate was continuously rotated along its axis during the deposition process.

A PS fiber array was deposited onto the gold surface and heated in an oven at 110 °C for 20 min to increase adhesion. Then, the fiber-masked sample was etched in freshly prepared gold etchant (15 mM thiourea, 10mM $Fe(NO)_3$, 1.2% HCl) [46] for 2 min while stirring at 350 rpm. PS fibers were dissolved in methylene chloride after etching, leaving behind the metallic features.

2.3.3 Surface characterizations

Lateral dimensions and heights of the nanopatterned features were measured using scanning electron microscopy (SEM) and atomic force microscopy (AFM), respectively. SEM imaging obtained at an electron beam energy of 5 keV were used to measure fiber diameter and etched feature widths. To measure the height of the etched features, AFM scanning was performed with a Si probe (NANOWORLD NCST-20) in tapping mode. All experimental data was obtained from at least two independent sets of experiments with multiple measurements (at least 10 per sample) on multiple samples to verify the repeatability.

2.4 Results and discussion

We demonstrate the versatility of SWAN lithography in patterning of 3D objects with various degrees of non-planarity, followed by detailed characterization of the SWAN lithography process itself. SWAN lithography enables simultaneous nanopatterning of the full arc length of curved geometries, such as the GC cylinder (Ø3 mm × 5 mm) shown in Fig. 2.2a. PS fiber masks of different diameters resulted in multiscale etched features with widths of 900 nm, 50 nm, or alternating width of 50 nm and 150 nm that were formed on the entire lateral surface of the cylinder with high pattern fidelity. Such nanopatterned substrates may be utilized as highly sensitive neural

electrodes.[47] A GC cube (6 mm × 6 mm × 6 mm) was modified by polishing one of its vertices to create a triangular face on the vertex (Fig. 2.2b). Separate layers of PS fibers, each with a different diameter, were deposited in three different orientations that crossed at 60° angles. Solvent vapor treatment and electrochemical etching resulted in 300 nm, 600 nm, and 900 nm wide etched features on the vertex surface (Fig. 2.2b-i). Similarly, 350 nm wide etched features in a crisscross pattern were achieved on the lateral surfaces of the GC cube (Fig. 2.2b-ii). Pattern fidelity across adjoining faces and at sharp corners can be robustly achieved, as shown in Fig. 2.2b-iii. Such 3D objects covered with nanostructures on all surfaces constitute a new class of passive devices which for example can be utilized in antireflectivity applications. [48]

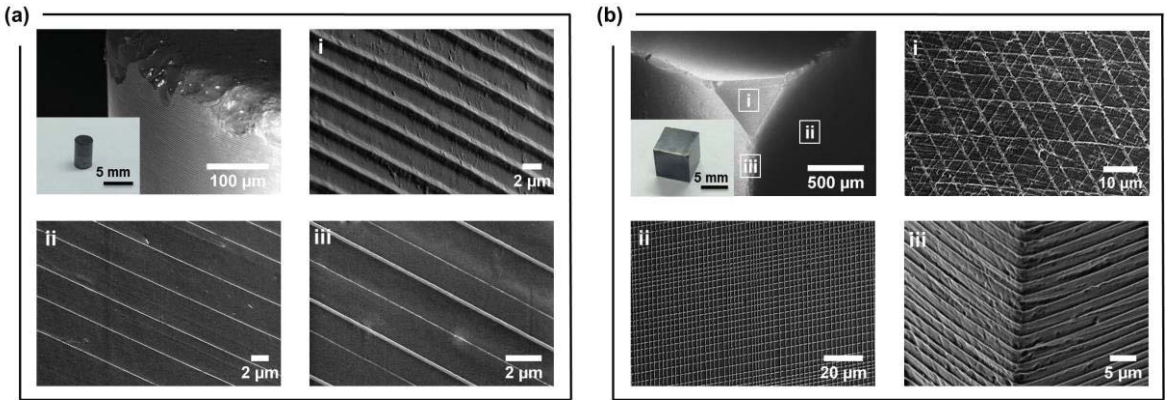

Figure 2. 2 Fabrication of micro/nano-structures on non-planar GC surfaces. a) Multiscale structures on the lateral surface of a GC cylinder. SEM images show linear features with widths of a-i) 900 nm, a-ii) 50 nm, or a-iii) alternating widths of 50 nm and 150 nm. b) Patterning of a GC cube with a polished vertex. SEM image of b-i) crisscross linear features with three different widths of 300 nm, 600 nm, and 900 nm on the polished vertex of the GC cube, b-ii) 350 nm wide etched features in an electronic circuit pattern on a face of the GC cube, b-iii) the etched features along an edge of the GC cube.

For many functional device applications, it is desirable to pattern a deposited metal film. As a proof of concept, we deposited a thin film of gold on a hyperbola-shaped glass substrate (Fig. 2.3a), followed by deposition of the PS nanofiber mask and wet etching to achieve 300 nm wide

gold features over the entire surface of the object. The variation in cross-sectional area and curvature of the substrate had no impact on uniformity of the nanopatterns (Fig. 2.3b), which in comparison is difficult to achieve by EBL or soft lithography. The gold patterns formed may be used as components of electrical or optical devices or as resists for further processing of the underlying substrate to achieve high aspect ratio features. This process may also be used to pattern optical fibers for a host of imaging and sensing applications.[49]

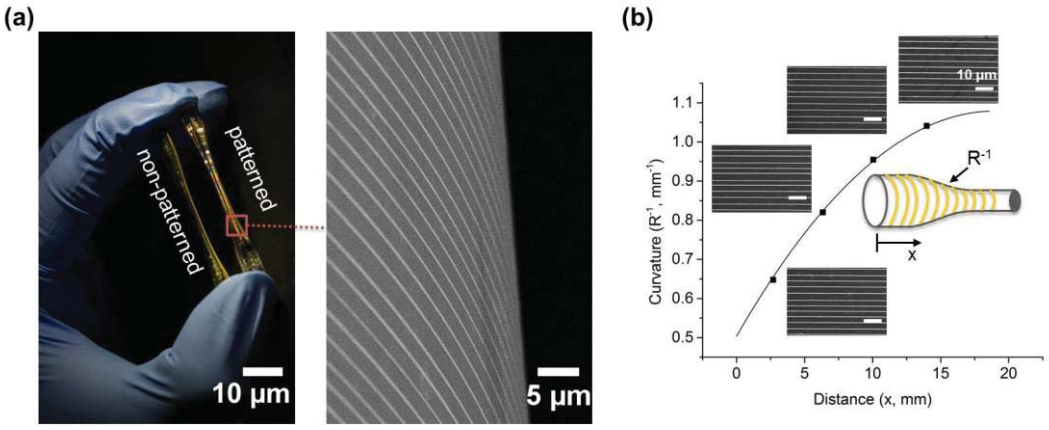

Figure 2. 3 Patterned gold film on a hyperbola-shaped glass substrate. a) Photograph of the original (left) and the nanostructured (right) substrates with structural coloration. SEM image shows 300 nm wide gold lines on the lateral surface with changing curvature. b) Curvature change along the length of the substrate. SEM images are from the marked locations with different curvatures. All scale bars are 10 µm.

Next, we characterized the SWAN lithography process on flat GC substrates (10 mm × 10 mm × 1 mm). Features of different sizes were obtained by either controlling the diameter of fibers[22,23] or by controlling the size of the fiber-substrate contact area (Fig. 2.4, 2.5). To investigate the dependency of the etched feature width upon fiber diameter, fibers of various diameters were deposited on flat GC substrates. All samples were exposed to THF vapor for 3 min to enhance interfacial adhesion without changing the fiber morphology and were then etched for a short period of time (5 s). The etched feature widths were equal to the fiber-substrate contact widths and were

measured to be (fiber diameter: etched feature size (mean±s.d.)) 85±6 nm: 46±3 nm, 134±8 nm: 82±7 nm, 173±9 nm: 111±7 nm, 219±15 nm: 141±10 nm, and 374±41 nm: 200±18 nm (Fig. 2.4a). The fiber diameter-etched feature width relation is in agreement with the Johnson, Kendall, and Roberts (JKR) contact theory,[50–52] which states that for a fixed set of materials (PS fiber and GC surface), the contact width (b) scales with the fiber diameter (D) according to $\boldsymbol{b^{1.5} \propto D}$ (see Fig. 2.4 inset). This experimentally validated relationship combined with our ability to deposit fibers of various diameters, offer novel enabling means for single-step fabrication of systems and devices with precisely designed application specific multiscale features.

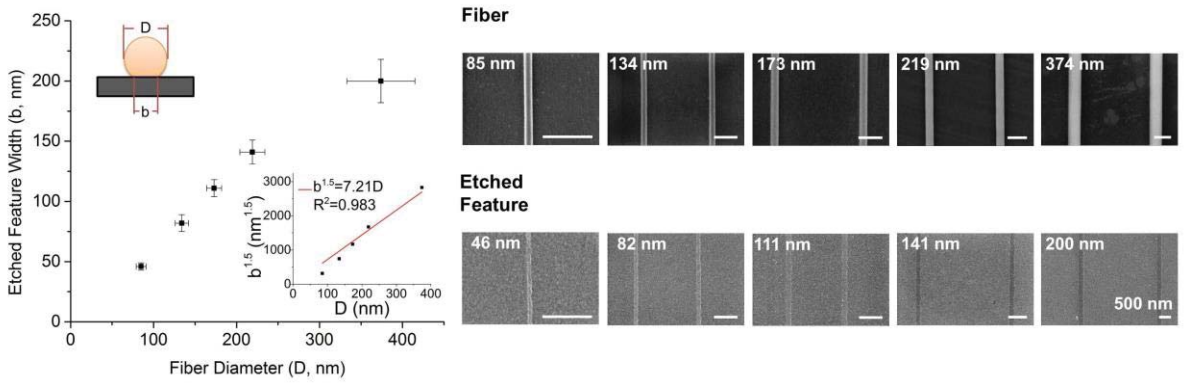

Figure 2. 4 Relationship between the deposited fiber diameter and the etched feature width (n=573 for fiber diameter measurement, n=335 for etched feature width measurement). Cartoon shows the cross-section of a fiber deposited on a substrate. SEM images depict fibers with different diameters and the corresponding etched features. The inset plot shows the fitting of experimental data according to the JKR contact theory. All error bars are standard deviations. All SEM scale bars are 500 nm.

While etched feature size can be controlled by fiber diameter, a wider range of feature sizes can be achieved by changing fiber morphology using a controlled solvent vapor treatment process. Solvent molecules penetrate the polymeric fibers, causing them to deform and spread on the substrate.[53] Therefore, increasing solvent vapor exposure time can increase the fiber-substrate contact width (Fig. 2.5). To determine the role of solvent vapor exposure time on feature width,

we fixed the PS fiber diameter (219 nm) and varied the solvent exposure duration from 0-30 min. For short 0-3 min exposure duration, fiber contact with the substrate was sporadic, resulting in inconsistencies in feature width. For increased 3-5 min exposure duration, the fiber-substrate interfacial adhesion was enhanced without changing the fiber morphology; thus, the width of the resulting feature remained constant. With further increase in exposure duration (8-20 min), both the fiber contact width and etched feature size were observed to continuously increase. For exposure duration longer than 20 min, no further increase in fiber width was achieved; consequently the etched feature size remained constant. Thus, by exposing 219 nm diameter fibers to THF vapor for 3-30 min, we were able to control etched feature width from 141±10 nm to 623±27 nm.

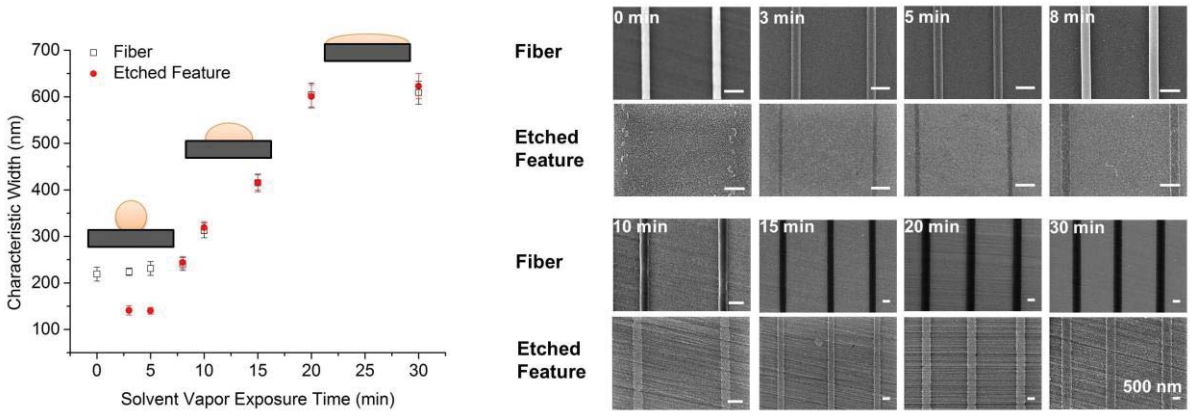

Figure 2. 5 Changing the solvent vapor exposure time to change the etched feature width (n=867 for fiber width measurement, n=602 for etched feature width measurement). Cartoons show the deformation of fiber in presence of the solvent vapor. SEM images are fibers and corresponding etched features after different solvent vapor exposure times. All error bars are standard deviations. All SEM scale bars are 500 nm.

Lastly, the height of the etched features was controlled by varying the duration of the electrochemical etching process. For the fixed process parameters of PS fiber diameter (219 nm) and THF vapor treatment time (20 min with resulting mask contact width of 600 nm), when the

etch time was varied from 5 s to 180 s, etched feature height increased from 27±3 nm to 182±18 nm. For etch times longer than 180 s, no further increase in the etched feature height was observed (Fig. 2.6). This is attributed to the reduction and eventual loss of contact between the fiber and the substrate due to undercutting during the etching process.

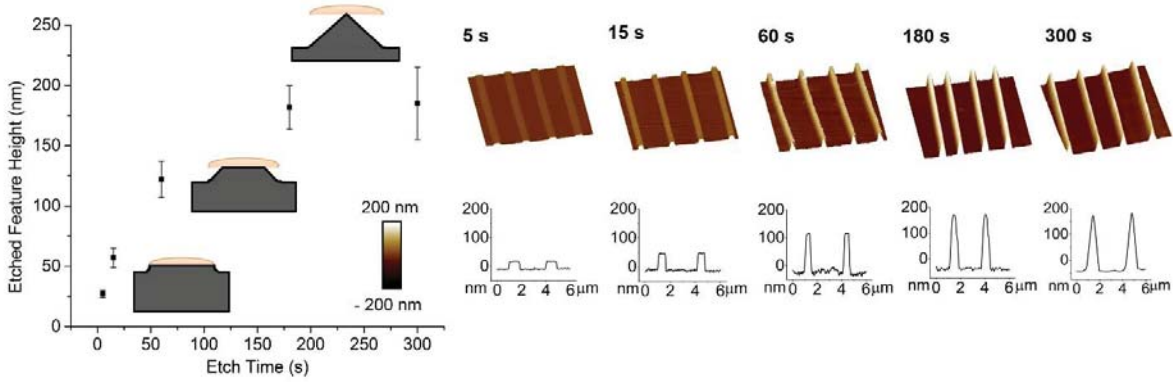

Figure 2. 6 Relationship between etch time and feature height for a fixed feature base width (n=672). Cartoons show the increasing etched feature heights for longer etch time. AFM cross-section and 3D images show the feature heights for different etch times. All error bars are standard deviations.

SWAN lithography can be applied to other soft and rigid bulk materials (e.g. Si, Fig. S2.1†) that can be etched using electrochemical, wet chemical, or dry etching processes. Similarly, this method can be applied to thin films deposited on soft or rigid substrates. This technique may be carried out in standard laboratory settings with minimal processing steps and is independent of substrate electrical, optical, or mechanical properties. Size of the fabricated feature is determined by the (1) fiber diameter, (2) fiber and substrate materials, (3) solvent vapor exposure duration, and (4) etching method and duration. Our multiscale lithography method enables high throughput ($>10^{-7}$ m^2/s) and large area fabrication of sub-50 nm to several-micron features (Fig. S2.2†) with exquisite control on feature sizes and high pattern fidelity irrespective of the substrate geometry.

Our nanofiber mask deposition method is highly scalable, cost- effective, and is capable of achieving even higher throughputs (Fig. S2.3†).

The distinguishing features of the SWAN lithography, compared to other methods that are also based on direct deposition of masking geometries,[54,55] are: (i) defect-free patterning over large-areas, (ii) multiscale patterning in a single step, (iii) wrapping of the masking geometry around the object which enables whole surface nanopatterning of macroscale objects in a single step. SWAN lithography also offers distinct advantages in comparison with the conventional nanofabrication techniques of EBL, soft lithography, and direct-write methods. In contrast to EBL, SWAN lithography produces high fidelity patterns over large-areas irrespective of degree of non-planarity of the substrate and overcomes EBL's limitations in the size of the patterned area and achievable resolution that are attributed to variation in beam incidence angle, exposure dosage, and uniformity in resist coating thickness.[37,38] In comparison with soft lithography and nanoimprint lithography based techniques,[33,34,39–41] SWAN lithography obviates the need for master templates that are typically fabricated using low throughput and costly methods. Furthermore, it overcomes soft lithography's challenge with pattern distortion on highly non-planar or irregularly shaped pre-structured 3D objects, which is shown to occur due to lack of full conformity of the 2D elastomeric stamp[39–41] and nanopatterned polymeric device layers.[42–44] Our masterless technique can robustly achieve sub-100 nm feature sizes, whereas in soft lithography, low elastic modulus of the stamps makes it highly challenging to reliably achieve sub-100 nm features over large-area 3D objects. Lastly, compared with resistless nanolithography and direct-write methods such as focused ion beam milling and ion beam proximity printing[41] that provide more versatility in substrate shape, SWAN lithography has much higher throughput, lower cost, and does not alter the material surface properties.

2.5 Conclusion

In conclusion, for the first time, we report a lithography technique for fabrication of multiscale structures, from micro to nanoscale, on the whole surface of pre-structured 3D objects. SWAN lithography enables simple, rapid and affordable production of design iterations of nanopatterned templates (Fig. S2.4†) and may be utilized to alleviate the main challenge associated with high throughput methods such as soft-lithography and roll-to-roll lithography[56] that rely on nanopatterned hard templates. Facile, scalable, cost-effective, and high throughput fabrication of micro/nanostructures on wide variety of 3D substrate geometries provides opportunities in development of new nanodevice configurations that have been difficult or impossible to obtain. Thus, it could significantly contribute to the scientific progress as well as technological advancement in different fields including photonics/plasmonics, electronics, and biotechnology in which unique properties of well-ordered nanoscale patterns enhance functionality and performance.

2.6 Electronic supplementary information

2.6.1 Nanopatterning of silicon

A silicon wafer (University Wafer; p-type, <100> orientation, 0.01-20 Ω cm, 100 mm in diameter, 500 μm thick) was cut into 5 mm × 20 mm pieces by a diamond cutter. PS fibers of 219 nm diameter were deposited on the surface of a silicon substrate and exposed to THF vapor for 10 min using the method described earlier. The fiber-masked silicon substrate was etched in KOH solution (40% w/v) at 30 °C for 20 min. Reactive ion etching (RIE) of silicon was performed with 219 nm

diameter PS fiber mask (no solvent vapor treatment) at 1800 W RF power, 80 W platen power for 2 cycles in an Alcatel AMS 100 I-SPEEDER DRIE system. Each cycle included 300 sccm SF_6 for 7 s, 150 sccm C_4F_8 for 2 s.

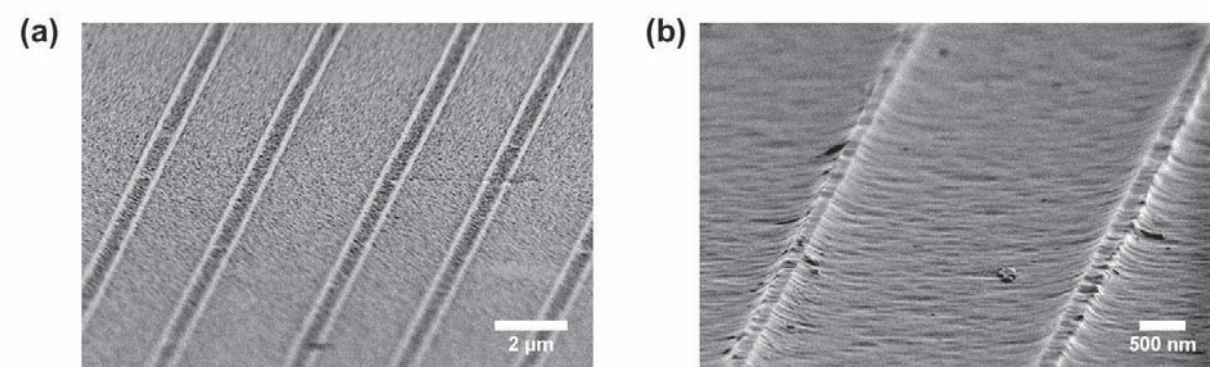

Figure S2. 1 a) SEM image of the fiber-masked silicon substrate after wet-chemical etching. Etched feature width is 600 nm. b) SEM image of silicon after RIE. Etched feature width is 200 nm.

It is well expected that the choice of etching method influences the produced feature size. In electrochemical or wet-chemical etching processes, the maximum feature width is equal to the contact width between fiber and substrate, as the fiber mask would be surrounded by a liquid (Fig. S2.1a). Compared to wet-chemical etching, electrochemical etching rate can be more precisely controlled by changing the poised potential on the electrode, but the substrate is required to be electrically conductive. If reactive ion etching (RIE) is used, the pattern width is equal to the fibermask diameter (or deformed fiber width), due to directional (vertical) nature of the ion etching process (Fig. S2.1b). Moreover, dry etching methods such as RIE are conducted in absence of a liquid; thereby eliminating the strong fiber mask-substrate adhesion requirement of electrochemical and wet-chemical etching methods.

2.6.2 Lateral feature size

The minimum lateral dimension of continuous and uniform feature in this study is 46 nm, and can be decreased with more exact control over fiber deposition, solvent vapor treatment, and the etching processes. For instance, a 10% PS solution of molecular weight of 860K g mol^{-1} was used to form 25 nm diameter fiber, as shown in Fig, S2.5. The fiber appears slightly deformed due to interaction with the electron beam during the SEM. The resulting 23.8±3.5 nm feature was formed after treating the sample in THF vapor for 3 min and etching for 5 s. Substrate grain structure size was comparable to etched feature size, resulting in a less distinct etched feature. Micron-scale features can also be achieved by SWAN lithography. As a proof of concept, an 18% PS solution of molecular weight of 2,000K g mol^{-1} was used to deposit larger diameter fiber mask, followed by treatment in THF vapor for 40 min and etching for 15 min, which resulted in 2 μm wide features.

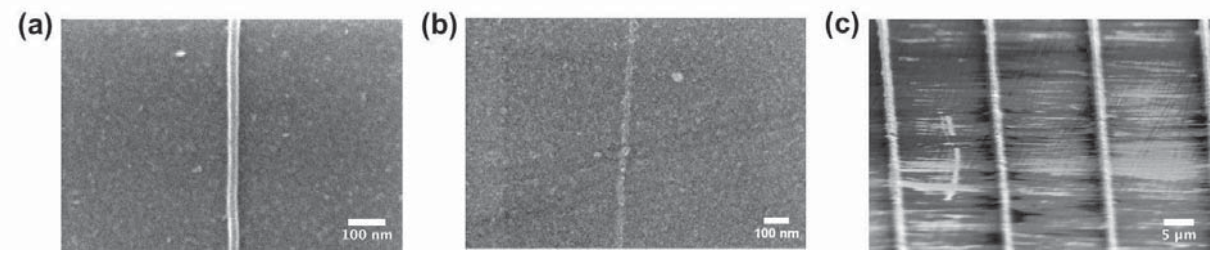

Figure S2. 2 a) SEM image of a 25 nm diameter PS fiber on a GC substrate. b) SEM image of the resulting etched feature. c) SEM image of 2 μm wide etched features.

2.6.3 SWAN lithography throughput

Depositing nanofiber mask takes the majority of the time for SWAN lithography process; thus, it is the limiting factor of the throughput rate. To calculate a representative throughput, a 10 mm diameter (D) cylindrical substrate is used as an example. To deposit nanofibers with 0.2 μm diameter (d) and 1.8 μm spacing (S), the substrate is spun at a rotational speed (ω) of 360 rpm and

the motorized stage is moved at a linear speed of $V = (d + S)\omega = 0.012\, mm/s$. The areal coverage rate ($\dot{A}$) by nanofiber mask is $\dot{A} = \pi \times D \times V = 3.8 \times 10^{-7}$ m^2/s. Increasing the substrate cross-section size or spin-wrapping multiple substrates in parallel can further improve the throughput. Compared to the commonly used nanopatterning techniques, SWAN lithography has much higher throughput than electron beam lithography (EBL) and focused ion beam (FIB) milling, and similar throughput to nanoskiving.[57–60] It has lower throughput than soft lithography and nanoimprint lithography, but it does not require a nanostructured master that is typically fabricated by the aforementioned lower throughput nanopatterning techniques.

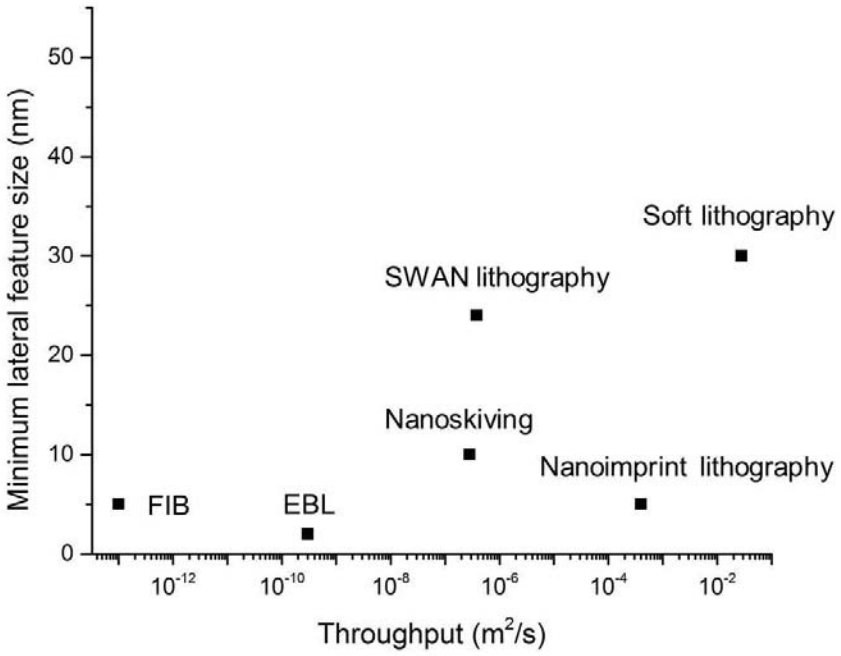

Figure S2. 3 Minimum lateral feature size vs. areal throughput for SWAN lithography and commonly used nanopatterning methods.

	SWAN lithography	EBL	FIB	Nanoskiving	Soft lithography	Nanoimprint lithography

Minimum lateral feature size (nm)	25	3	5	10	30	5
Throughput (m^2/s)	3.8×10^{-7}	3×10^{-10}	10^{-13}	2.8×10^{-7}	2.8×10^{-2}	4×10^{-4}
Capital cost ($)	50 K	2 M	0.5-2 M	60 K	Low	Low
Need master	No	No	No	No	Yes	Yes
Pattern nonplanar surface	Yes	Difficult	Difficult	No	Yes but limited to soft material and low curvature	Yes but limited to hard material

Table 2. 1 Comparison of advantages and disadvantages of SWAN lithography and commonly used nanopatterning methods.

2.6.4 Replica molding

Sylgard® 184 silicone elastomer (Dow Corning) base and curing agent were mixed at 3:1 ratio. The resulting Polydimethylsiloxane (PDMS) prepolymer was cast onto a patterned GC surface, cured at 90 °C for 1 h and then at 150 °C for additional 3 h. After PDMS was completely cured, it was peeled off the GC template. The PDMS sheet and a no. 1 glass coverslip were pressed together after being treated in air plasma for 45 s (200 mTorr, 18 W). A 200 μM F1300 fluorescein (Life Technologies) solution was flowed into the nanochannels. Fluorescence microscopy image was taken using an Axio Observer.Z1 inverted microscope (Zeiss Microscopy) with a Plan-Apochromat 63×/1.40 oil objective (Zeiss Microscopy) and an AxioCam MRm camera (Zeiss Microscopy). A post scan of the original template confirmed no damage to original features after repeated replica molding.

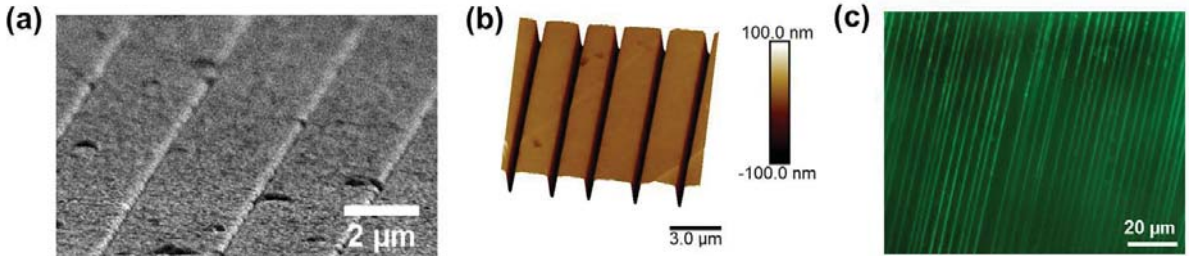

Figure S2. 4 a) SEM image of the PDMS nanochannels created by replica molding. b) AFM image of the PDMS nanochannels. c) fluorescence microscopy image of fluorescein solution flowing through a functional PDMS nanofluidic device.

2.6.5 Gold nanopattern characterization

To confirm that the gold features (as shown in Fig. 2.3 of the manuscript) are indeed continuous, experimental measurements were conducted and the results were compared with theoretical predictions.

Experimental Measurements: We measured the conductance (G) of the unpatterned gold (Au) film, the adhesion promoting titanium (Ti) film (deposited beneath the Au film), and arrays of 300 nm wide Au nanowires at 1.8 µm spacing, all on the 2 mm diameter and 5 mm long sections of the 3D hyperbola-shaped substrate (see figure below). All measurements were performed in triplicates. The conductance of the 100 nm Au film, $G(Au\ film)_{exp}$, and the 10 nm Ti film, $G(Ti\ film)_{exp}$, were measured to be 0.124±0.014 S, and 2×10^{-4} S, respectively. The conductance of the Au nanowire array, $G(Au\ nanowires)_{exp}$, was measured to be 0.016±0.004 S. Since our measurements indicated that $G(Au\ film)_{exp} \gg G(Ti\ film)_{exp}$, we neglected the contribution of the Ti adhesion layer in our theoretical analysis below.

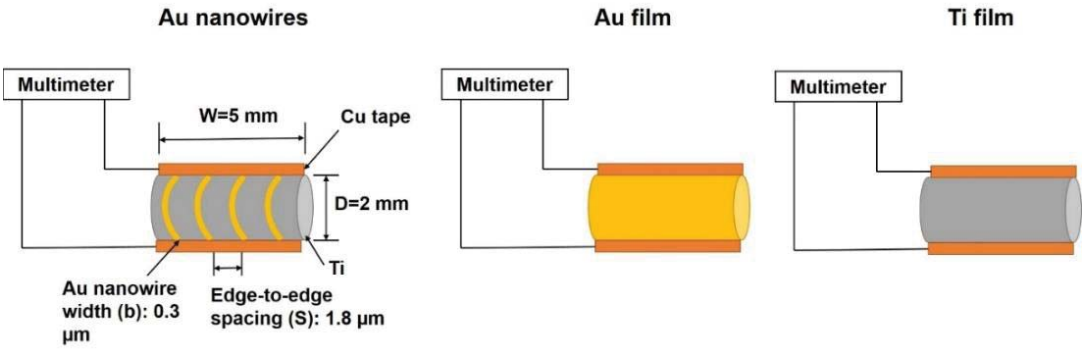

Figure S2. 5 Schematics of Au nanowires, Au film and Ti film conductance measurements.

Theoretical Predications: Conductance is defined as $G = \sigma\ (A/l)$, where σ is the conductivity, A is the cross-sectional area perpendicular to the direction of the electric current, and l is the length of the conductor. For the nanowire array, $A = Nbh$, where N is the number of nanowires in the 5 mm wide section of the cylinder, $b = 300\ nm$ is the width of each nanowire, and $h = 100\ nm$ is the thickness of each nanowire. For the Au film, $A = Wh = N(b + S)h$, where $W = 5\ mm$ is the width of the Au film, and $S = 1.8\ \mu m$ is the edge-to-edge spacing between the nanowires. In both cases, the length of the conductor, $l = \pi D/2$, where $D = 2\ mm$ is the diameter of the cylindrical section. Given that σ, l and h are the same for the Au nanowire array and the Au film, if the Au nanowires are continuous, the conductance ratio can be calculated from:

$$\frac{G(Au\ nanowires)_{theroy}}{G(Au\ film)_{theory}} = \frac{A(Au\ nanowires)}{A(Au\ film)} =$$

$$\frac{W(Au\ nanowires)}{W(Au\ film)} = \frac{Nb}{N(b+S)} = \frac{0.3\ \mu m}{0.3\ \mu m + 1.8\ \mu m} = \frac{1}{7} = 0.143$$

The theoretical conductance ratio is in agreement with the experimentally measured ratio:

$$\frac{G(Au\ nanowires)_{exp}}{G(Au\ film)_{exp}} = \frac{0.016 \pm 0.004}{0.124 \pm 0.014} = 0.129 \pm 0.035$$

The variations in the conductance measurement data is attributed to contact resistances between the probes and the film/nanowire array. The close match between the theoretical and experimental ratios suggests that the features are continuous and free of major defects.

Chapter 3: Effect of Electrode Sub-micron Surface Feature Size on Current Generation of *Shewanella oneidensis* in Microbial Fuel Cells

3.1 Abstract

Microbial fuel cells (MFCs) are envisioned to serve as compact and sustainable sources of energy; however, low current and power density have hindered their widespread use. Introduction of 3D micro/nanostructures on the MFC anode is known to improve its performance by increasing the surface area available for bacteria attachment; however, the role of the feature size remains poorly understood. To delineate the role of feature size from the ensuing surface area increase, nanostructures with feature heights of 115 nm and 300 nm, both at a height to width aspect ratio of 0.3, are fabricated in a grid pattern on glassy carbon electrodes (GCEs). Areal current densities and bacteria attachment densities of the patterned and unpatterned GCEs are compared using *Shewanella oneidensis* Δ*bfe* in a three-electrode bioreactor. The 115 nm features elicit a remarkable 40% increase in current density and a 78% increase in bacterial attachment density, whereas the GCE with 300 nm pattern does not exhibit significant change in current or bacterial attachment density. The current density dependency on feature size is maintained over the entire 160 h experiment. Thus, optimally sized surface features have a substantial effect on current production that is independent of their effect on surface area.

This work was published in *J. Power Sources* **347**, 270-276, 2017.

3.2 Introduction

Microbial fuel cells (MFCs) use exoelectrogenic bacteria (e.g. *Shewanella oneidensis* and *Geobacter sulfurreducens*) as catalysts to generate electricity from organic and inorganic substrates. MFCs are envisioned to have applications in wastewater treatment, environmental sensing, bioremediation, hydrogen production, and miniature vehicle powering [61–65]. While power density of MFCs has increased by several orders of magnitude over the past decade, an improvement of another one to two orders of magnitude is needed to enable commercial consideration [66]. In this regard, one of the major areas of focus has been the anode, since the extracellular electron transport occurs between the anode biofilm and the anode surface. Anodes of 3D structured materials (e.g. fiber felt [67], non-woven carbon fiber [68], stainless steel foam [69]) have been shown to significantly enhance the performance of MFCs. Modification of the electrode surface by addition of nanomaterials, including nanoparticles [70–72], carbon nanotubes [73–76], carbon nanostructures [77], and graphene [78–80], has also been shown to improve the power generation. These modifications typically changed the surface chemistry (e.g. surface energy, functional groups, and charge) and the surface topography (e.g. feature shape and feature size) making it challenging to identify the specific factors that contribute most to the improved performance. Most studies have attributed the positive effect of the surface micro/nanostructures solely to the increased available surface area for bacterial attachment. However, it is now known that certain topographical feature sizes reduce bacterial attachment density despite the increase in actual surface area [10,11,13,15,81]. Furthermore, it is shown that single cell morphology [18–20], and expression of certain genes [21] are regulated by the size of the surface features. In this work, to investigate the effect of feature size on current production of *S. oneidensis* in MFCs, we utilized our previously developed Spun-wrapped aligned nanofiber (SWAN) lithography technique [82] to texturize electrodes with well-

defined and precisely controlled topographical features and disambiguated the effect of topographical feature size from the ensuing effect of surface area increase on bacterial attachment and current production.

3.3 Experimental Methods

3.3.1 Electrode assembly and surface nanostructure fabrication

Glassy carbon (GC) was chosen as the electrode material due to its high electrochemical activity, biocompatibility, and surface smoothness after polishing. Electrodes were assembled as shown in Figure 3.1(a). Before assembly, the back face and edges of the GC chip (10 mm × 10 mm, and 1 mm thick, Hochtemperatur-Werkstoffe GmbH, Germany) were roughened using a 320 grit sandpaper, followed by sonication in deionized water, flushing with dry air and then further drying on a hot plate at 180 °C. A wire was soldered to a copper plate (6 mm × 6 mm), which was then adhered to the back face of the GC piece by conductive epoxy. The back of this assembly was covered by a biocompatible and autoclavable epoxy (Master Bond, Hackensack, NJ), leaving only the front face of the GC chip exposed to the bacteria solution in the experiment. After curing at room temperature overnight, the assembled glassy carbon electrode (GCE) was further cured at 70 °C for another 3 h. The exposed surface of the GCE was polished successively by 1 μm, 0.3 μm, and 0.05 μm alumina slurry to produce a smooth surface finish. Smooth electrodes serve as the control (unpatterned) electrodes and also as the base for fabricating the nanopatterned electrodes. Nanostructures in a grid pattern were fabricated on the unpatterned GCEs using SWAN lithography [82]. First, 7 wt% and 14 wt% polystyrene (PS, molecular weight of 2000 kg mol^{-1}) in xylene solutions were used to deposit 170 nm (for fabrication of the small features) and 370 nm (for fabrication of the large features) fiber masks on the GCE surfaces, using the non-

electrospinning spinneret based engineered tunable parameter (STEP) technique [22]. To fuse fibers to the substrate, the fiber-masks were then exposed to tetrahydrofuran vapor under atmosphere conditions for 40 min (170 nm fiber) or 60 min (370 nm fiber). The mask covered electrodes were etched at 2.0 V (vs. Ag/AgCl) in 0.1 M NaOH solution for 5 min (small feature) and 10 min (large feature), respectively. After etching, the masking fibers were gently wiped off and the electrodes were further treated in piranha solution (3:1 H_2SO_4 and H_2O_2) for 40 min to remove the PS fiber residue. The patterned surface nanostructures were characterized by scanning electron microscopy (SEM) and atomic force microscopy (AFM). In order to check the surface activity of the electrodes after mechanical polishing and electrochemical etching, cyclic voltammetry (CV) at a scan rate of 100 mV s^{-1} in a solution of 1 M KNO_3 and 1 mM ferricyanide was conducted.

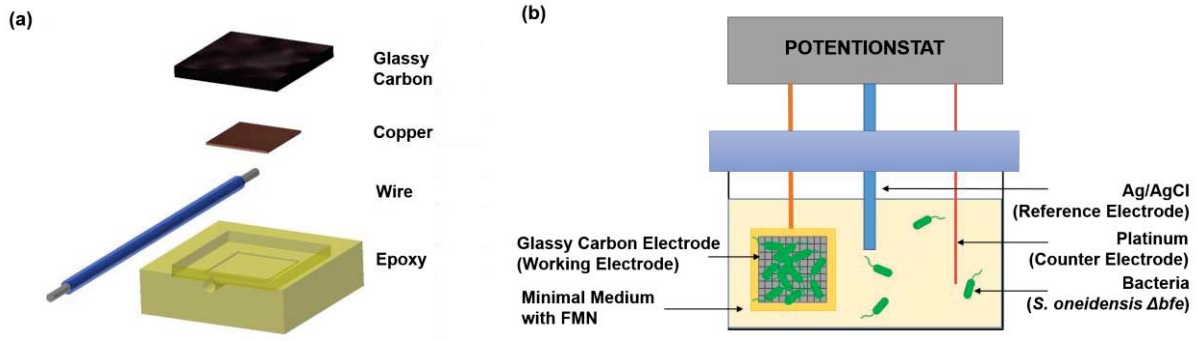

Figure 3. 1(a) Exploded view of the glassy carbon electrode (GCE) assembly. (b) Schematic of the bioreactor setup used for electrochemical performance characterization.

3.3.2 Bacteria culture and bioreactor setup

S. oneidensis Δ*bfe* [83] was streaked from -80 °C frozen stock on a 1.5% Luria-Bertani (LB) agar plate (10 g l^{-1} tryptone, 5 g l^{-1} yeast extract, 10 g l^{-1} NaCl, and 15 g l^{-1} agar) and cultured at 30 °C

for 24 h. A single colony was isolated from the plate and inoculated into a 125 ml flask containing 10 ml LB media and cultured at 30 °C and 150 rpm. Bacteria were harvested after 5 hours, centrifuged at 1,700 g for 10 min and resuspended in minimal medium (MM) twice, then transferred to a 1000 ml flask containing 100 ml MM with 10 μM flavin mononucleotide (FMN, Sigma-Aldrich, St. Louis, MO), and cultured at 30 °C and 150 rpm. Bacteria were harvested at OD_{600}=1 (Fig. S3.1), centrifuged, and resuspended in fresh MM supplemented with 10 μM FMN and then introduced into the bioreactor. The MM contains 0.46 g l^{-1} of NH_4Cl, 0.225 g l^{-1} of K_2HPO_4, 0.225 g l^{-1} of KH_2PO_4, 0.117 g l^{-1} of $MgSO_4 \cdot 7H_2O$, 0.225 g $l^{-1}$of $(NH_4)_2SO_4$, 10 ml of a mineral mix (containing 1.5 g l^{-1} of nitrilotriacetic acid, 0.2 g l^{-1} of $FeCl_2 \cdot 4H_2O$, 0.1 g l^{-1} of $MgCl_2 \cdot 6H_2O$, 0.02 g l^{-1} of sodium tungstate, 0.1 g l^{-1} of $MnCl_2 \cdot 4H_2O$, 0.1 g l^{-1} of $CoCl_2 \cdot 6H_2O$, 1 g l^{-1} of $CaCl_2 \cdot 2H_2O$, 0.05 g l^{-1} of $ZnCl_2$, 0.002 g l^{-1} of $CuCl_2 \cdot 2H_2O$, 0.005 g l^{-1} of H_3BO_3, 0.01 g l^{-1} of sodium molybdate, 1 g l^{-1} of NaCl, 0.017 g l^{-1} of Na_2SeO_3, and 0.024 g l^{-1} of $NiCl_2 \cdot 6H_2O$), and 100 mM HEPES as buffer [84,85]. MM was adjusted to pH 7.2 and autoclaved. After autoclaving, filter sterilized 0.05% (w/v) casamino acids, 100 mM lactate, 5 ml of a flavin-free vitamin solution (containing 0.002 g l^{-1} of biotin, 0.002 g l^{-1} of folic acid, 0.02 g l^{-1} of pyridoxine HCl, 0.005 g l^{-1} of thiamine, 0.005 g l^{-1} of nicotinic acid, 0.005 g l^{-1} of pantothenic acid, 0.0001 g l^{-1} of B-12, 0.005 g l^{-1} of *p*-aminobenzoic acid, and 0.005 g l^{-1} of thioctic acid) were added [84].

3.3.3 Electrochemical experiments in a bioreactor

The bioreactor included a three-electrode system, with the GCE as the working electrode, a platinum wire as the counter electrode, and an Ag/AgCl electrode as the reference electrode (Fig.

3.1(b)). The three electrodes were kept at fixed distances in all experiments. After addition of the bacterial suspension, the GCE was poised at 0.24 V vs. standard hydrogen electrode (SHE) and the current production was recorded by a multichannel potentiostat (Solartron Analytical 1480 MultiStat). The areal current density is defined as the measured current divided by the real surface area of the electrode. Each GCE was placed in a separate bioreactor with a small hole on the top to maintain atmospheric pressure during the experiment. The bioreactors were kept in a water bath at 30 ºC to maintain constant temperature during the experiment. At 72 h, additional lactate to a final concentration of 20 mM was added to make sure that the electrode biofilm had enough electron donors. After that, additional 20 mM lactate was added every 24 h for the entire duration of the experiment (around 160 h). After 160 h, to remove the planktonic bacteria, the bacteria solution was centrifuged at 3,000 g for 10 min twice and then filtered through a 0.2 μm filter. During the process of centrifugation and filtration, the biofilm covered electrodes were maintained in fresh MM and were subsequently put back into the original medium without planktonic bacteria and poised at 0.24 V vs. SHE. The current production was compared to the current production in the original bacteria suspension. The current recovery ratio is defined as the ratio of current after removal of planktonic bacteria to the respective current in presence of planktonic bacteria. In preliminary experiments, reduced CV peaks of the electrodes after one bioreactor experiment indicated that the electrodes cannot be directly used in the next experiment, however, the electrochemical activity recovered after piranha solution treatment (Fig. S3.2). Thus, after each set of experiments, the electrodes were treated in piranha solution for 30 min to oxidize and remove organic biofilm residues. The activity of the electrode after piranha solution treatment was checked by CV measurement in a solution of 1 M KNO_3 and 1 mM ferricyanide.

3.3.4 Evaluation of biofilm coverage and bacterial attachment density

Upon completion of the electrochemical measurements, the electrodes were gently rinsed in fresh MM to remove loosely attached bacteria and were stained with the LIVE/DEAD™ BacLight® bacterial viability kit according to the manufacturer's instructions. Fluorescent microscopy images of the entire GCE surface were taken using 2.5× objective and the mosaic images were stitched together. Cells with a compromised membrane that are dead or dying will stain red (DsRed), while cells with an intact membrane stain green (GFP). All images were taken at the same intensity and exposure time.

In order to quantitate the number of viable bacteria on the electrode surface, we used the method of serial dilution and plating to count the number of colony-forming units (CFU). First, bacteria on the epoxy frame of the GCE were scraped away using a razor blade. Then, the biofilm on the glassy carbon surface was collected and suspended in 10 ml MM by vortex shaking at 1,500 rpm and sonication for 30 s, three separate times. After serial dilution, 100 μL of the diluted bacteria solution was plated on an LB agar plate and incubated at 30 °C for 24 h. For each electrode, we plated three agar plates and averaged the CFU count from the three plates. All bioreactor experiments were repeated at least four times. The areal bacterial attachment density is defined as the CFU divided by the real surface area of the electrode.

Electrodes were prepared for SEM imaging following fluorescent microscopy imaging [86]. Electrodes were first placed in 2.5% glutaraldehyde in phosphate buffered saline (PBS) for 2 hours at 4 ºC. The electrodes were then soaked in 0.1 M PBS for 20 min twice, followed by soaking in distilled water for 20 min twice. The electrodes were then serially dehydrated by soaking in 35%, 50%, 75%, 95% ethanol for 30 min each and in 100% ethanol for 3×30 min. The 100% ethanol was finally replaced with hexamethyldisilazane (HMDS) for 30 min twice. HMDS was pipetted out and the electrodes were air dried overnight.

3.3.5 Statistical analysis

Statistical analysis of the data was conducted using Origin 9.0 (OriginLab, Northampton, MA). In particular, a one-way analysis of variance (ANOVA) followed by Fisher's LCD test was used to determine statistical significance. A p-value of 0.05 was used as the threshold for significance. Standard errors were calculated and represented as error bars in the respective figures.

3.4 Results and discussion

3.4.1 Electrode surface feature characterization

Nanostructures with uniform feature size and spacing in a grid pattern were fabricated on the electrode surface, as shown in Fig. 3.2(a). Using the procedure described in section 2.1, one electrode was patterned with small features and one with large features. The base width of the small feature was measured to be 0.41±0.01 μm (N=20) and the base width of the large feature was measured to be 0.93±0.08 μm (N=21). All widths were measured from SEM images (Fig. 3.2(b)). The cross-section of the features was triangular in shape and the height to width aspect ratio (H/W) was close to 0.3 for both pattern sizes. The peak-to-peak spacing (S) between two adjacent linear structures was approximately 3.1 μm for both patterns (3.1±2.4 μm for 0.4 μm pattern, N=226; 3.1±1.9 μm for 1.0 μm pattern, N=210), which provided the same pattern areal density for both designs. The height of the small feature was measured to be 115±6 nm (N=17) and the height of the large feature was measured to be 300±12 nm (N=14). Given the higher importance of feature height, compared with its base width, in interaction with bacteria, we refer to the feature sizes studied in this work by their height (i.e. "115 nm pattern" and "300 nm pattern"). The roughness of the unpatterned GCE was measured to be 5.1±0.4 nm (N=6), which

was much lower than the heights of the patterns on nanostructured electrodes. All heights were measured from AFM scanning data (Fig. 3.2(c)). *S. oneidensis Δbfe* bacteria were measured to have a length of 1.87±0.53 μm and a diameter of 0.53±0.09 μm (N=100). The aforementioned surface pattern designs provided many opportunities for the bacteria to contact the surface nanostructures due to the high pattern density. Furthermore, low aspect ratio of the nanostructures makes all of the surface area (i.e. both the nanostructures and the flat areas in between) available

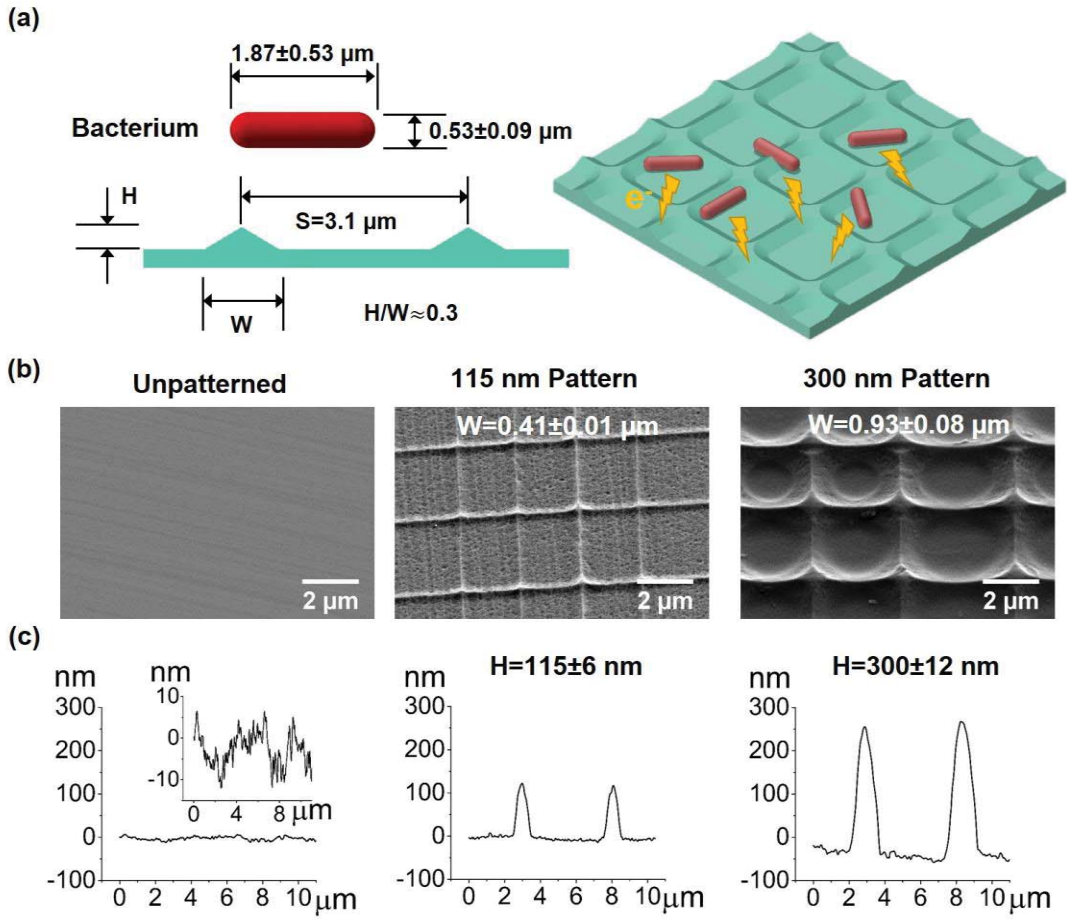

Figure 3. 2 (a) Schematic on the left shows the cross-sectional view of the surface nanopattern and the bacterium. Schematic on the right shows select modes of bacteria-nanostructured surface interactions. (b) SEM images show the unpatterned and patterned GCE surface topography. (c) AFM data show the unpatterned GCE roughness and the patterned GCE feature heights.

for bacterial attachment. Compared to the unpatterned surface, the 115 nm pattern increased the surface area by 4.3%, and the 300 nm pattern increased the surface area by 10.7%. There is no significant difference in the CV peaks of the electrodes after mechanical polishing and electrochemical etching (Fig. S3.1), which demonstrates that the nanopatterning did not change the electrochemical activity of the electrodes.

3.4.2 Current production

It is known that wild-type *S. oneidensis* MR-1 can secrete and accumulate flavins (riboflavin and FMN), which can increase the reduction rate at the electrode [83]. Thus, the differences in current production associated with surface features might be masked by different concentrations of flavins

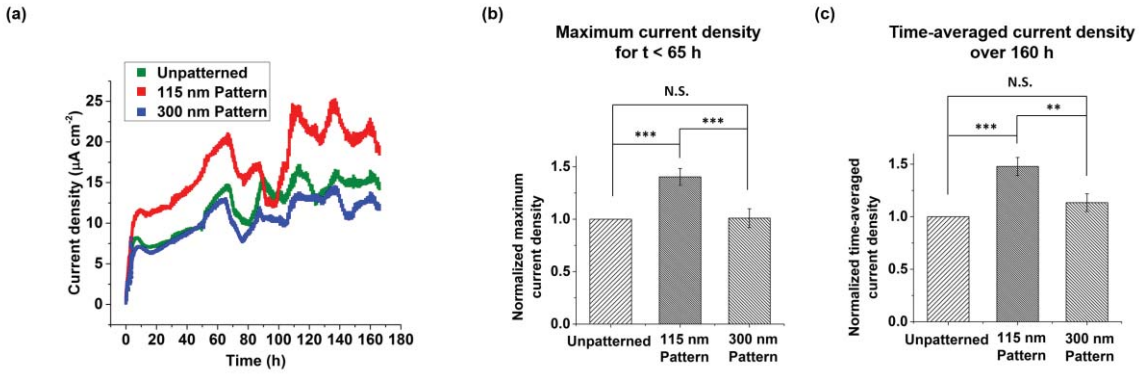

Figure 3. 3 (a) A representative plot of the current densities vs. time for GCEs with smooth surface, 115 nm pattern, and 300 nm pattern. (b) Comparison of maximum normalized current densities for t<65 h (N=10 per category). (c) Comparison of the normalized time-averaged current densities over the 160 h experiment (N=7 per category). ** p-value<0.01, *** p-value<0.001, N.S. not significant.

produced by the planktonic and surface-associated bacteria. In order to minimize the influence of endogenous flavins, *S. oneidensis* Δ*bfe* mutant, which secretes flavins at a significantly lower rate was used [87]. To further minimize the bacteria influence on flavins concentration, a relatively high concentration of FMN (10 μM) is exogenously added at the beginning of the experiment, which would be much higher than the endogenous flavin secreted during the experiments [87]. This enabled us to compare bacterial current generation as a function of surface feature size at similar concentrations of FMN.

In order to exclude the effect of the surface area increase resulting from introduction of the nanostructures, the measured current was normalized by the actual surface area (1 cm^2 for the unpatterned GCE, 1.043 cm^2 for the GCE with 115 nm pattern, 1.107 cm^2 for the GCE with 300 nm pattern), and was reported as *areal current density*. As shown in Fig. 3.3a, the areal current density for all three GCEs continuously increased for 60-65 h and then fluctuated during the rest of the experiment duration (~65–160 h). The increase of the current density is attributed to the biofilm development on the electrode and the planktonic bacteria growth. Since a biofilm is a dynamic system with both growth and dispersal occurring at the same time, fluctuations in current were observed throughout the 160 h period of experiments, even after a steady average current was reached at 60-65 h.

To quantitatively compare the current production of the GCEs, we normalized the current densities of the patterned GCEs to the unpatterned GCE. We first compared the maximum normalized current densities over the first 65 h (Fig. 3.3(b)). The unpatterned electrode produced an average current density of 16.1±5.3 μA cm^{-2} (N=10). The electrode with 115 nm pattern produced a 40% higher average current density which was significantly higher than the unpatterned electrode (N=10, $p<0.001$). On the other hand, the electrode with 300 nm pattern produced a similar current

density as the unpatterned electrode and no statistically significant difference between the two was observed (N=10). To investigate the role of surface features on long-term performance of the electrode, we also compared the time-averaged current densities over the total 160 h duration of the experiments (Fig. 3.3(c)). The average (N=7) time-averaged current density of the unpatterned GCE was 10.0±3.1 μA cm^{-2}. The GCE with 115 nm pattern produced a 48% higher time-averaged current density than the unpatterned electrode (N=7), which also showed statistical difference ($p<0.001$). The GCE with 300 nm patterns produced a 14% higher time-averaged current density than the unpatterned electrode, but the difference was not statistically significant (N=7). This demonstrates that introducing surface features in certain sizes (e.g. 115 nm high with an aspect ratio of 0.3) can significantly increase the current production, however, not all feature sizes (e.g. 300 nm high at a similar aspect ratio) can affect the MFC performance. Both the maximum current density at 60-65 h and the time-averaged current density over the total 160 h experiment of the GCE with 115 nm pattern were significantly higher, which indicates that the optimally sized submicron features affect current density over short (<65 h) and long (160 h) timescales.

In order to compare the current contribution from the electrode biofilm and the planktonic bacteria, we removed the planktonic bacteria in the solution at the end of the 160 h experiment. The current of the GCEs with smooth surface, 115 nm and 300 nm patterns all recovered to almost the same level as the currents measured before removing the planktonic bacteria (Fig. 3.4). Recovery occurred within 30 minutes which is too brief of a time period for significant dissociation and regrowth of planktonic population. This indicates that, for all cases, the current production was primarily attributable to the biofilm.

3.4.3 Bacterial attachment

To explore the correlation between the current production and the surface-associated biofilm, we compared the biofilms on the surface of the unpatterned GCE, the GCE with 115 nm and the GCE with 300 nm patterns when the current reached the maximum within the first 65 h and also at the end of the 160 h experiment. When the current reached its maximum at 60-65 h, the biofilm development on the electrodes also reached a quasi-steady state in the experimental setting. The unpatterned GCE had an average of 1.2×10^{8} CFU cm^{-2} attached (N=4). When normalized to the

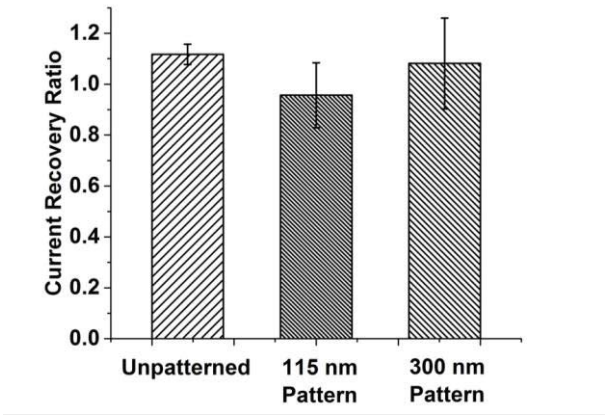

Figure 3. 4 Current recovery ratio describing the ratio of current after removal of planktonic bacteria to the respective current in presence of planktonic bacteria (N=3 for each category).

unpatterned GCE, the GCE with 115 nm pattern had a 78% higher cell attachment density (Fig. 3.5(a-i)). However, the GCE with 300 nm pattern did not show any increase in cell attachment density. The difference between the GCE with 115 nm pattern and the unpatterned GCE was verified by the ANOVA statistical analysis ($P<0.05$). For the GCE with 115 nm pattern, the cell density increase (78% higher than the unpatterned GCE) was much higher than the current increase (40% higher than the unpatterned GCE). This can be contributed to a reduced electron transfer rate from the outer layer of the thicker biofilm (i.e. mass transfer resistance) [88]. The fluorescent microscopy images (Fig. 3.5(a-ii)) shows that the GCE with 115 nm pattern had more uniform biofilm coverage than the unpatterned GCE and the GCE with 300 nm pattern, which was consistent with the CFU counting (and the current measurements). The SEM images (Fig. 3.5(a-iii)) also confirm that the bacterial attachment density on the GCE with 115 nm pattern was higher than the other two electrodes.

To investigate the biofilm development over the period of 65-160 h, bacteria on the electrode surface were also counted at the end of the 160 h experiment. The average cell density of the unpatterned GCE was 4.5×10^7 CFU cm^{-2} (N=4), which was smaller than the bacterial attachment density at 60-65 h. Average cell density on the patterned GCEs were somewhat reduced to 1.35×10^8 CFU cm^{-2} for the GCE with 115 nm pattern and to 9.45×10^7 CFU cm^{-2} for the GCE with 300 nm pattern. The lower reduction rate of the surface associated bacteria on the patterned electrodes can be attributed to the positive role of sub-micron surface features in the retention of bacteria cells on patterned surfaces [89] . The bacterial attachment density of the GCE with 115 nm

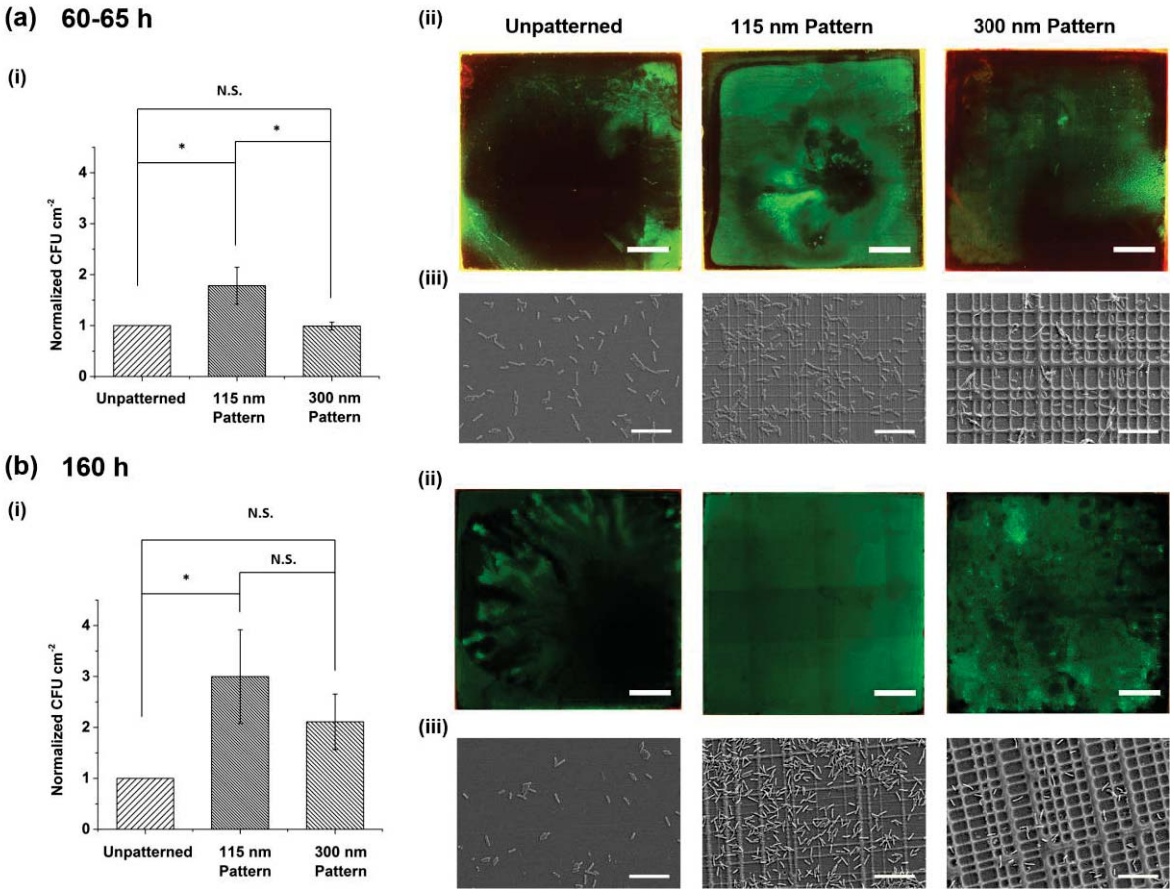

Figure. 5 Normalized bacterial attachment density on GCEs with smooth surface, 115 nm pattern, and 300 nm pattern at (a-i) 60-65 h and (b-i) 160 h. Fluorescent microscopy images of biofilms at (a-ii) 60-65 h and (b-ii) 160 h. Scale bars are all 2 mm. SEM images of the biofilms at (a-iii) 60-65 h and (b-iii) 160 h. Scale bars are all 10 µm. * p-value<0.05, N.S. not significant.

pattern was 3.0 times of that on the unpatterned GCE, and the bacterial attachment density of the GCE with 300 nm pattern was 2.1 times of that on the unpatterned GCE (Fig. 3.5(b-i)). However, AVONA analysis showed that only the GCE with 115 nm pattern had a significant increase in the bacterial attachment density relative to the unpatterned GCE. This was further demonstrated by the fluorescent microscopy images (Fig. 3.5(b-ii)) and the SEM images (Fig. 3.5(b-iii)). The high magnification fluorescent microscopy images show that almost all of the bacteria exhibited green fluorescence, which indicates that the majority of the attached bacteria were alive (Fig. S3.3). The results suggest that while the 300 nm patterns did not significantly increase the bacterial attachment density, the surface features do help maintain uniform biofilm coverage over long periods [89,90].

3.5 Conclusion

Bacterial adhesion to the MFC electrode is the first crucial step in biofilm formation and current production. Understanding the effect of surface feature size on bacterial activity at the anode is a critical step toward designing MFCs with higher power density. In this study, we investigated the effect of the electrode surface feature size on current production in MFCs. Nanostructures in a grid pattern with feature heights of 115 nm and 300 nm, both at a height to width aspect ratio of 0.3 were fabricated on GCEs, and their areal current densities were compared to the unpatterned GCE using *S. oneidensis* Δ*bfe* mutant. Only the GCE with 115 nm structures exhibited significantly increased areal current density (i.e. 40% higher than the unpatterned GCE at 60-65 h). On the other hand, the GCE with 300 nm nanostructures had a current density similar to the unpatterned GCE. The increased current density of the GCE with 115 nm nanostructures was due to the more mature and uniform coverage of the biofilm on the electrode surface, as evident by the 78% increase in bacterial attachment density. However, the GCE with 300 nm structures had similar bacterial

attachment density as the unpatterned GCE. The thermodynamic principles governing the vesicle-rigid surface interactions can be used to qualitatively interpret these results [10,91]. Bacteria can conform to small (115 nm) surface features to increase their adhesion energy (due to increase in available binding sites) with minimal energy expenditure on membrane deformation, making the surface more favorable for attachment. Whereas presence of larger (300 nm) surface feature necessitates larger membrane deformation which will not be offset by the increased adhesion area, therefore no enhancement is observed in the case of 300 nm features. Bacteria size, shape, and cell membrane physicochemical properties as well as substrate surface energy, surface feature shape and size will dictate the outcome of cell-surface interaction. Thus, the current production and the attachment density of the bacteria on the electrode surface was shown to be a function not only of the available surface area of the electrode, but also the size of the surface feature of the electrode. Our findings strongly suggests that to increase the current and power production of MFCs, the electrode surface must be modified with features that are optimally sized to enhance bacterial attachment and biofilm development. Introducing these optimally sized nanostructures with small changes in actual surface area will not have a notable effect on of the electrode material cost, but highly improves the performance of MFCs.

3.6 Supplementary data

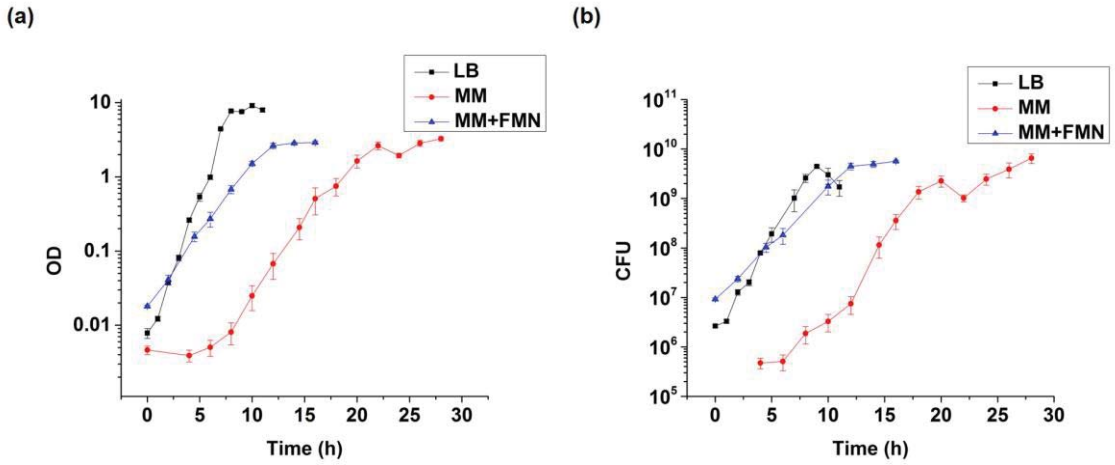

Figure S3. 2 (a) Optical density (OD_{600})-based and (b) CFU based-growth curve of *S. oneidensis* Δ*bfe* grown in LB, MM and MM with FMN media.

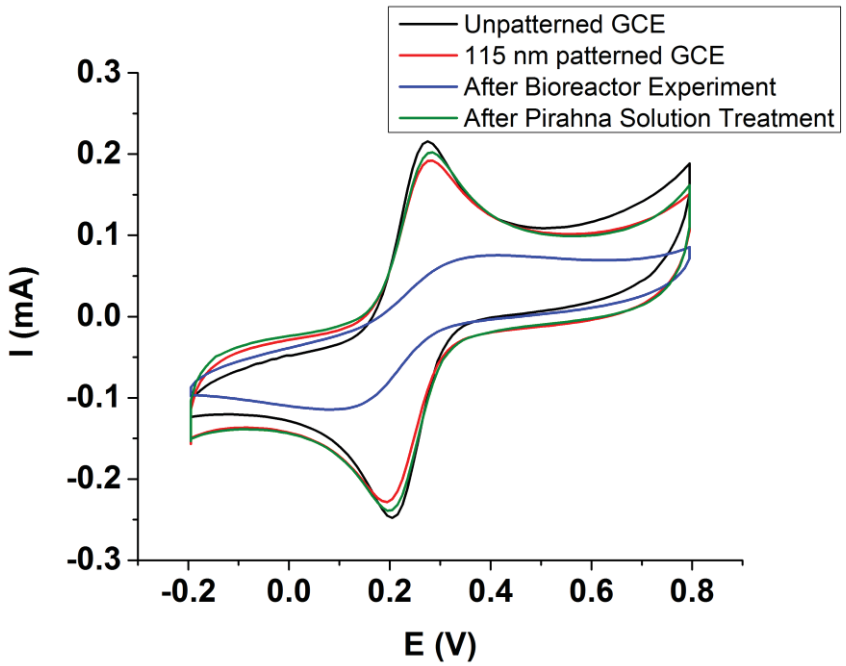

Figure S3. 1 Cyclic Voltammetry (CV) of a GCE in 1 M KNO_3 solution with 1 mM ferricyanide (1) after mechanical polishing, (2) after electrochemical etching, (3) after the bioreactor experiment, and (4) after pirahna solution treatment. The scan rate is 100 mV s^{-1}.

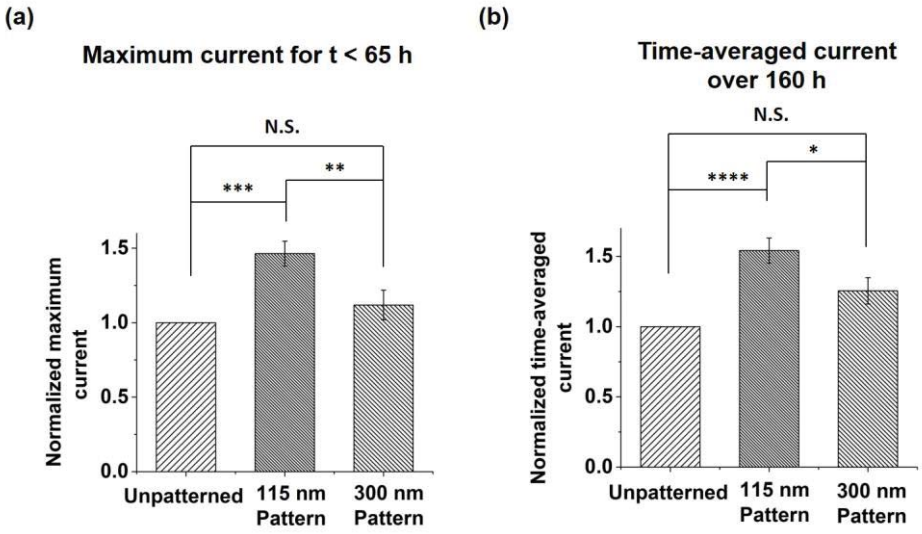

Figure S3. 3 (a) Comparison of normalized maximum current for t<65 h (N=10 per category). (b) Comparison of normalized time-averaged current over the 160 h experiment (N=7 per category). * p-value<0.05, ** p-value<0.01, *** p-value<0.001, **** p-value<0.0001, N.S. not significant.

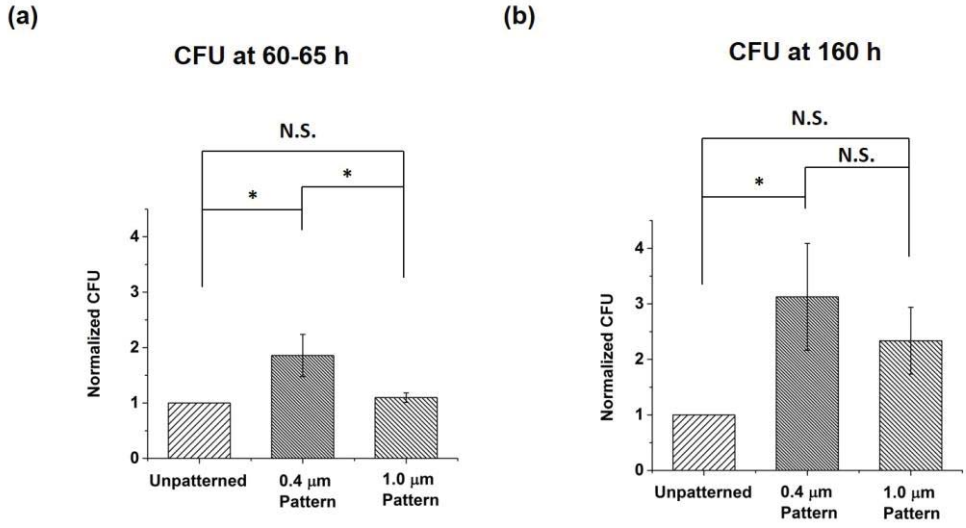

Figure S3. 4 Comparison of normalized bacterial number for t=60-65 h (N=4 per category). (b) Comparison of normalized bacterial number for t=160 h (N=4 per category). * p-value<0.05, N.S. not significant.

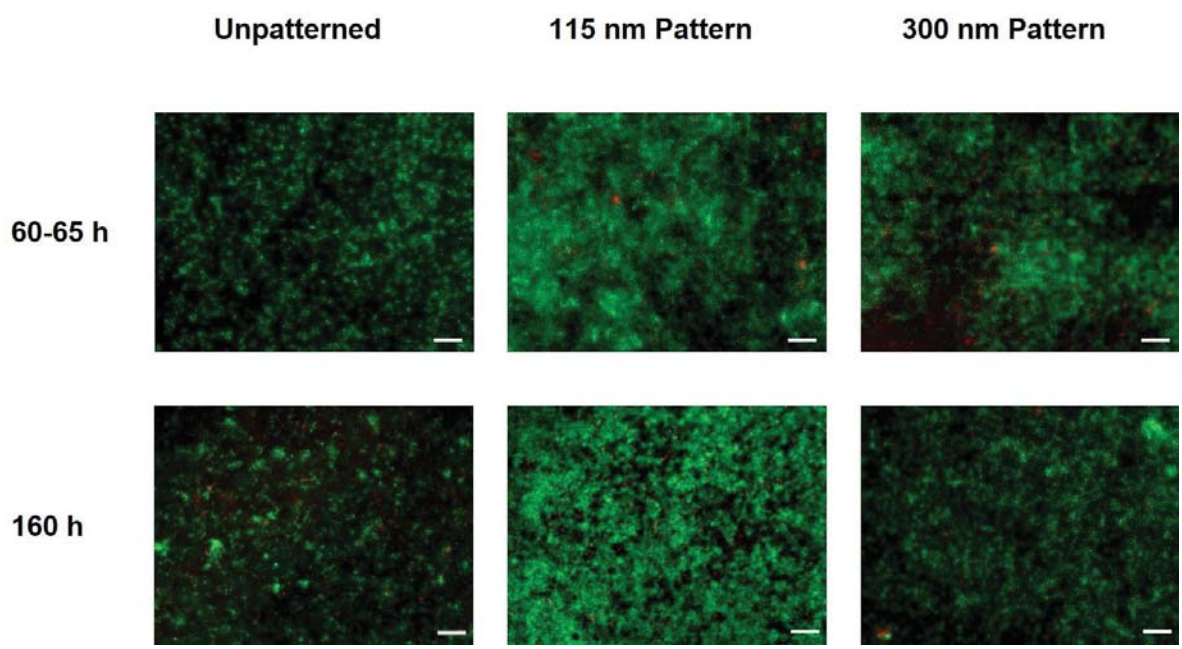

Figure S3. 5 Fluorescent microscopy images of biofilms on GCEs with smooth surface, 115 nm pattern, and 300 nm pattern at 60-65 h and 160 h. Green fluorescence (GFP) represents live bacteria, and red fluorescence (DsRed) represents dead bacteria. Scale bars are all 20 μm.

Chapter 4: A Biophysical Model for *ab initio* Design of Nanofiber-Coated Surfaces for Mitigation of *Candida albicans* Fouling on Medical Catheters

4.1 Abstract

Many taxa of microorganisms live in surface associated multicellular communities, known as biofilms. Pathogenic biofilms are responsible for a substantial portion of healthcare associated infections. Recent works have shown that nanoscale structural features have wide-ranging and long-lasting effects on microorganism adhesion and biofilm development. However, a biophysical model describing the effect of the geometry and size of nanostructures on microbial adhesion is lacking. In this work, we report a biophysical model of the adhesion of the model fungal pathogen, *Candida albicans*, on nanofiber-coated surfaces. Our theoretical model enables quantification of the total energy (adhesion energy and stretching energy) of adherent cells as a function of the geometry (i.e. nanofiber diameter) and configuration (i.e. spacing) of the nanofibers. We utilized the non-electrospinning Spinneret-based Tunable Engineering Parameters (STEP) technique to construct nanofiber-coated polystyrene surfaces and experimentally verified the model predictions for the effect of highly ordered surface nanostructures (0.5 μm – 2.0 μm diameter nanofibers) on the population-level cell attachment density. The biophysical model can be utilized for *ab initio* design of surfaces that resist biofilm growth for medical applications and beyond. We demonstrate successful prototypical examples of the reduction in biofilm formation by optimally designed nanofiber coating of urinary and central venous catheters.

AhRam Kim (M.S. 2015) contributed to the dynamic retention assay experiments in section 4.4.2. Carolyn Y. Mottley contributed to part of the simulation in section 4.4.1 and 4.4.3 and the dynamic retention assay experiments in section 4.4.3.

This chapter in its entirety will be submitted as a manuscript to a peer-reviewed journal. The co-authors are Zhou Ye, AhRam Kim, Carolyn Y. Mottley, Michael W. Ellis, Amrinder S. Nain, Candace Wall, Alan R. Esker and Bahareh Behkam.

4.2 Introduction

Microorganisms attach and form biofilms on living and nonliving surfaces. A biofilm is a multilayer community of adherent cells and their self-produced matrix of extracellular polymeric substances (EPS). Biofilm formation is a costly problem in the marine [92], food processing [93], and healthcare industries [94]. In particular, healthcare associated infections cause approximately 100,000 deaths and an estimated $28-45 billion in added healthcare costs per annum, of which infections on medical devices are responsible for a substantial portion [95]. Compared to planktonic cells, biofilms are more resistant to antimicrobial agents (e.g. antibiotics, surfactants, and silver nanoparticles) due to both transport limitations and phenotypic changes in the adherent cells [96]. In recent years, studies have found that the early-stage biofilm formation is highly regulated by surface micro/nano topography [97]. Previous work by our group and others has demonstrated the efficacy of micropatterned [98,99] and nanopatterned [10,90,100,101] surfaces in respectively controlling biofilm formation and reducing microbial adhesion. However, a quantitative framework that enables *ab initio* design of surface patterns that optimally reduce biofilm formation is currently lacking. Development of such framework can significantly enhance the current iterative process of anti-fouling biomaterial design by defining a narrower design space.

In the past, several approaches have been used to model early-stage reversible microbial adhesion. Perhaps the most well-known is the Derjaguin-Landau-Verwey-Overbeek (DLVO) theory of colloid stability, which has been extended to microbial adhesion. The DLVO theory expresses the cell-substrate interactions as a balance of long-range Lifshitz-van der Waals interactions and electrostatic double layer interactions [102]. The DLVO theory can qualitatively explain the influence of the ionic strength of the culture medium [103,104] and the substrate charge density [105,106], but cannot

explain the experimentally measured forces in media with a high ionic concentration or high pH (e.g. 10^{-2} M and pH=9.5 NaCl solution) due to the increased hydration force [107,108]. Thermodynamic-based approaches have also been developed to model microbial adhesion by describing the interactions in terms of the adhesion free energy (ΔG_{ad}) [109,110]. Adhesion is energetically favorable for $\Delta G_{ad} < 0$, and unfavorable for $\Delta G_{ad} > 0$. Developed from the DLVO theory, the extended DLVO (XDLVO) theory also includes a short-range Lewis acid-base interaction from hydrogen bonding at the microbial-surface interface. Compared to the DLVO theory, the XDLVO theory has been shown to more accurately predict microbial adhesion behaviors [111–113]. However, all of the aforementioned models treat microorganisms as rigid particles without considering the stretching and deformation of the cell and the associated energy expenditure. The cell wall stretching could be significant for microorganisms with relatively low stiffness (e.g. yeast) or in presence of closely spaced and high aspect ratio micro/nanoscale surface patterns. For instance, stretching of the cell wall has been used to explain the bactericidal activity of nanopatterns on the cicada wing surface [114]. Thus, both the energy gain from adhesion and energy expenditure from the cell wall stretching must be included in modeling microbial adhesion on micro/nano-patterned surfaces, however, the role of the stretching energy on cell adhesion has not yet been explored.

Although none of the classical theories are capable of describing the adhesion outcome for all conditions and the search for a comprehensive model is ongoing [115], our goal here is more focused. We hypothesize that biofilm formation (i.e. population-scale microbial attachment density) trends can be predicted based on total energy trends for early stage adhesion. To this end, we develop a biophysical model that describes changes in the total energy of the cells associated with the adhesion as well as the cell wall stretching. We hypothesize that the surface patterns that cause

higher single cell total energy will have less cell attachment density and population-scale biofilm formation. This model calculates the energy of *C. albicans* yeast, a model fungal pathogen, adherent to nanofiber-coated surfaces with uniform fiber diameter and spacing. *C. albicans* is a human commensal and opportunistic fungal pathogen that can cause infection of the skin, oral cavity, esophagus, vagina, and vascular system. Although most traditional antifungals and the host immune response are capable of preventing large-scale infection, *C. albicans* biofilms associated with removable prosthetic devices and implants are often less susceptible to antimicrobial compounds and more pathogenic than their planktonic counterparts [116]. In this work, we theoretically and experimentally investigate the effect of nanofiber diameter and spacing on the energy of adherent cells. To validate our model, we conducted experiments using polystyrene (PS) substrates coated with PS nanofibers of varying diameters. Furthermore, we demonstrate the application of this experimentally-validated model in *ab initio* material design by showing the correlation between the total energy calculated from the biophysical model and the cell attachment density on fiber-coated catheters of different materials.

4.3 Materials and methods

4.3.1 Biophysical model of cell adhesion

C. albicans grows either as unicellular yeast or in filamentous pseudohyphal and hyphal forms (Figure S4.1). *C. albicans* biofilm formation often starts with the adherence of yeast cells on the substrate, followed by the growth and differentiation to pseudohyphal and hyphal forms [117,118]. We hypothesize that the total energy of a yeast cell at the early-stage of adherence, which can be highly regulated by the substrate surface topography, strongly influences the biofilm development

outcome. Thus, herein we focus on developing a biophysical model of the adhesion of *C. albicans* yeast to nanofiber-coated surfaces. The total energy (E_{tot}) of an adherent cell *relative to a planktonic cell* is comprised of the adhesion energy (E_{ad}, energy change from the formation of adhesion interfaces), the stretching energy (E_{str}, energy change on stretching the cell wall), and the bending energy (E_{c}, energy change on changing the cell wall curvatures) [119,120]:

$$E_{\mathrm{tot}} = E_{\mathrm{ad}} + E_{\mathrm{str}} + E_{\mathrm{c}} \quad (1)$$

Bending energy (E_{c}) was not considered in this study, since the E_{c} value was found to be negligible compared to E_{ad} (as shown in supplementary information section 2). Upon contact with a substrate, if $E_{\mathrm{tot}} > 0$, it is energetically unfavorable for the cell to adhere on the surface; whereas if $E_{\mathrm{tot}} < 0$, it is energetically favorable for the cell to attach. The lower the total energy, the higher the probability of a cell remaining adherent on the surface.

Non-specific interactions (e.g. van der Waals, electrostatic, and acid-base interactions) between the cell wall and the substrate govern the early-stage cell adhesion on abiotic surfaces [121], thus specific adhesion (e.g. by adhesins [122]) is ignored in this model. E_{ad} is defined as the surface integral of the work of adhesion (w_{ad}) over the cell-substrate contact area (A_{ad}):

$$E_{\mathrm{ad}} = -\oint w_{\mathrm{ad}} dA_{\mathrm{ad}} \quad (2)$$

Assuming a homogenous cell surface property, Eq. (2) is simplified to:

$$E_{\mathrm{ad}} = -w_{\mathrm{ad}} A_{\mathrm{ad}} \quad (3)$$

The value of w_{ad} is determined through experimental measurement of the dispersive (γ_c^d, γ_s^d) and polar (γ_c^p, γ_s^p) components of the surface energies of the *C. albicans* yeast (denoted with subscript c) and the solid substrate (denoted with subscript s) in conjunction with the equation below [123]:

$$w_{\mathrm{ad}} = 2\sqrt{\gamma_c^d \gamma_s^d} + 2\sqrt{\gamma_c^p \gamma_s^p} \quad (4)$$

The adhesion energy will decrease as the adhesion area increases, however, the cell must simultaneously experience an increase in energy as the cell wall stretches, which is denoted as E_{str}. The value of E_{str} can be calculated from the following equation [124]:

$$E_{\mathrm{str}} = \frac{1}{2} k_{\mathrm{str}} \frac{(A-A_0)^2}{A_0} \quad (5)$$

where k_{str} is the stretching modulus, A is the total surface area of the stretched cell after adhesion, and A_0 is the original cell surface area in a non-adherent state which can be approximated as a sphere with a diameter of D_{cell}.

The stretching modulus was calculated from the following equation [125,126]:

$$k_{str} = Y\, h \quad (6)$$

where Y is the average Young's modulus of the cell wall, and h is the average cell wall thickness. When the cell wall stiffness increases (higher Y), the stretching modulus will increase.

The total energy can be simplified as:

$$E_{\mathrm{tot}} = E_{\mathrm{ad}} + E_{\mathrm{str}} = -w_{\mathrm{ad}} A_{\mathrm{ad}} + \frac{1}{2} k_{\mathrm{str}} \frac{(A-A_0)^2}{A_0} = -\left(2\sqrt{\gamma_c^d \gamma_s^d} + 2\sqrt{\gamma_c^p \gamma_s^p}\right) A_{\mathrm{ad}} + \frac{1}{2} Y\, h \frac{(A-A_0)^2}{A_0} \quad (7)$$

The unknown parameters in Eq. (7) are A_{ad} and A. Based on the experimental observations, we assume that the overall cell shape remains spherical and any deformation is localized to the regions of interactions with the underlying substrate. We also assume that the cell volume remains

constant. For each cell-fiber distance (Δx, shown in Figure 4.1), with the aforementioned shape and volume constraints, we calculate E_{tot} for every combination of the geometric parameters (Figure 4.1, and supplementary information) in a physically meaningful range (e.g. $0 < \alpha < \pi$, $0 < \beta < \pi$, $\rho > 0$). The geometry of the cell that yields the minimum total energy for a specific cell-fiber distance is computed using an optimization routine. We then average the total energy of an adherent cell over all possible cell-fiber distance values for the patterned surface and normalize by dividing it by the total energy of an adherent cell on a flat surface. We hypothesize that surfaces with a lower value of the spatially-averaged normalized total energy will be less favorable for cell adhesion (see supplementary information for computational details).

4.3.2 Cell culture

Wild-type *C. albicans* strain SC5314 (ATCC MYA2876) was streaked on Sabouraud dextrose agar (SDA) plates and incubated at 37 °C for 24 h. Several (3-5) colonies were inoculated into 10 ml of yeast nitrogen base with 50 mM dextrose (YNBD) medium and the suspension was shaken at 37 °C and 150 rpm for 24 h.

4.3.3 Nanofiber deposition

PS fibers with uniform diameters (D_{fiber} =0.5-2.0 μm, Figure S4.2) at the edge to edge spacing of 2.0 μm (Figure S4.3) were deposited on flat PS substrates (3×15 mm, 0.125 mm thick) and catheters (10 mm long) using the non-electrospinning Spinneret-based Tunable Engineered Parameters (STEP) technique [23]. The nanofiber-coated substrates were sterilized under ultraviolet light inside a biological safety cabinet for 45 minutes and were conditioned by soaking in fetal bovine serum (FBS) overnight at 37 °C before the experiment.

4.3.4 Dynamic retention assay

All retention assays were performed in a Center for Disease Control (CDC) biofilm reactor (Figure S4.4), according to the methods previously established by Chandra *et al.* [127]. Yeast culture, grown in YNBD at 37 °C and 150 rpm for 24 h, was diluted to an OD_{520}=0.385 (~1×10^7 CFU/ml) in YNBD medium. Subsequently, 8 ml of the diluted yeast culture and 392 ml of YNBD medium were mixed and added to the CDC biofilm reactor. The bioreactor was placed on a magnetic stir plate inside an incubator at 80 rpm and 37 °C for 24 hours. The viable cell number on samples was counted from serial dilution and plate count method.

4.3.5 Scanning electron microscopy

After the 24h experiment in the bioreactor, select samples were gently washed in phosphate buffered saline (PBS) and then placed in 2.5% glutaraldehyde in PBS for 2 hours at 4 ºC. Subsequently, the samples were soaked in PBS for 20 min twice, and then in deionized (DI) water for 20 min twice. The samples were then serially dehydrated by soaking in 35%, 50%, 75%, 95% ethanol for 30 min each and in 100% ethanol for 3×30 min. The 100% ethanol was pipetted out and the samples were air dried overnight. The air dried samples were gold coated prior to scanning electron microscopy (SEM) imaging.

4.3.6 Contact angle measurement and surface energy calculation

After 24 h of growth, a yeast culture was harvested, washed twice by centrifugation, and suspended in DI water. The yeast cells were then collected on a nitrocellulose membrane filter (0.22 μm pores, Millipore) to a density of 10^8 cells/mm^2 to form a dense yeast film. The filters were placed on a microscope glass slide with double-side tape and dehydrated in a desiccator for 24 h. Contact

angles of DI water, formamide and diiodomethane were measured by depositing only one liquid droplet in the center of each yeast film. Time-lapse images at one frame per second were recorded upon the deposition of the liquid droplet. The contact angles were measured using the images that depicted the initial placement of each drop on the yeast film.

PS substrate was cut to 10 mm×10 mm pieces and the PS fiber material was solution cast on a microscope glass slide to a final thickness of 100 μm. The PS substrate and the cast PS fiber material were cleaned with ethanol and DI water and dried overnight prior to contact angle measurements. Contact angles of DI water, formamide and diiodomethane on the PS substrate and PS fiber material were measured by depositing one liquid drop on at the center of each substrate. A minimum of three independent measurements for each substrate were conducted.

A glass cuvette was treated by hexamethyldisilazane (HMDS) vapor to ensure a hydrophobic surface. The glass cuvette was filled with DI water, formamide or diiodomethane. The treated latex (Bard Medical) and silicone (Rochester Medical) urinary catheters and the treated polyurethane (PU) dog femoral central vein catheter (SAI Infusion Technologies) were cut to 10 mm long pieces and rinsed with ethanol and DI water. The catheter pieces were vertically inserted into the liquid and the contact angles between the liquid and the catheter walls were measured. A minimum of three independent measurements for each catheter type were conducted.

The solid-liquid (γ_{SL}) surface energy, the solid-vapor (γ_{SV}) surface energy, and the dispersive and polar components of the solid surface energy (γ_S^d and γ_S^p respectively) can be determined from the contact angle (θ) and the known values of the dispersive (γ_L^d) and polar (γ_L^p) components of the liquid surface energy (γ_{LV}) by equations (8) through (11):

$$\gamma_{SL} = \gamma_{SV} + \gamma_{LV} - 2\left(\gamma_S^d \gamma_L^d\right)^{1/2} - 2\left(\gamma_S^p \gamma_L^p\right)^{1/2} \quad (8)$$

$$\gamma_{SV} = \gamma_{SL} + \gamma_{LV}\cos\theta \tag{9}$$

$$\gamma_{SV} = \gamma_S^d + \gamma_S^p \tag{10}$$

$$\gamma_{LV} = \gamma_L^d + \gamma_L^p \tag{11}$$

In practice, this is accomplished by rearranging the preceding equations to fit the slope-intercept form of the equation of a line [123]:

$$\gamma_{LV}(1+\cos\theta)/2\left(\gamma_L^d\right)^{1/2} = \left(\gamma_S^p\right)^{1/2}\left(\gamma_L^p\ /\gamma_L^d\right)^{1/2} + \left(\gamma_S^d\right)^{1/2} \tag{12}$$

With the left side of Eq. (12) plotted against $\left(\gamma_L^p\ /\gamma_L^d\right)^{1/2}$, the slope is $\left(\gamma_S^p\right)^{1/2}$ and the intercept is $\left(\gamma_S^d\right)^{1/2}$. For each solid surface, we analyzed the results for each of the three liquids and plotted a best-fit line through the data to determine the slope and intercept and hence the dispersive $\left(\gamma_S^d\right)$ and polar components $\left(\gamma_S^p\right)$ of the solid surface energy.

4.3.7 Statistical analysis

The one-way analysis of variance (ANOVA) and Fisher's LCD test were conducted for statistical analysis. All analyses were conducted using Origin 9.0 (OriginLab, Northampton, MA). To determine the statistical significance, the threshold for p-value was set at 0.05. The error bars for all experimental data (Figure 4.3b and 4.4b) represent the standard deviations.

4.4 Results

4.4.1 Biophysical modeling results

We first analyzed the simplest case, wherein a cell only interacts with one fiber. As shown in Figure 4.1, the total energy of the cell, E_{tot}, varies with fiber diameter, D_{fiber}, as well as location

of the cell centroid with respect to the fiber centerline, denoted as Δx. From microscopy images of planktonic *C. albicans* yeast, the average diameter of the cell, D_{cell}, was measured to be 4.2 ± 1.2 μm (N=235). For Δx=0, when the cell is adhered to a fiber with diameter smaller than the critical fiber diameter, D_{crit}, the cell can wrap around the fiber and contact the underlying substrate. However, when adhered to a fiber with diameter larger than D_{crit}, the cell cannot contact the underlying substrate. For *C. albicans* yeast with k_{str}=416 mN/m and w_{ad}=77 mJ m^{-2} for adhesion to PS substrates, D_{crit} was determined to be 1.2 μm. For the case $D_{\text{fiber}} \leq D_{\text{crit}}$, E_{tot} has only one minimum which is a function of fiber diameter and occurs in the range of $\Delta x = 2.2 - 2.4$ (Figure 4.1a). For $D_{\text{fiber}} > D_{\text{crit}}$, E_{tot} has two local minima, one at $\Delta x = 0$ and the other is a function of fiber diameter and occurs at $\Delta x = 1.6 - 2.1$ (Figure 4.1b).

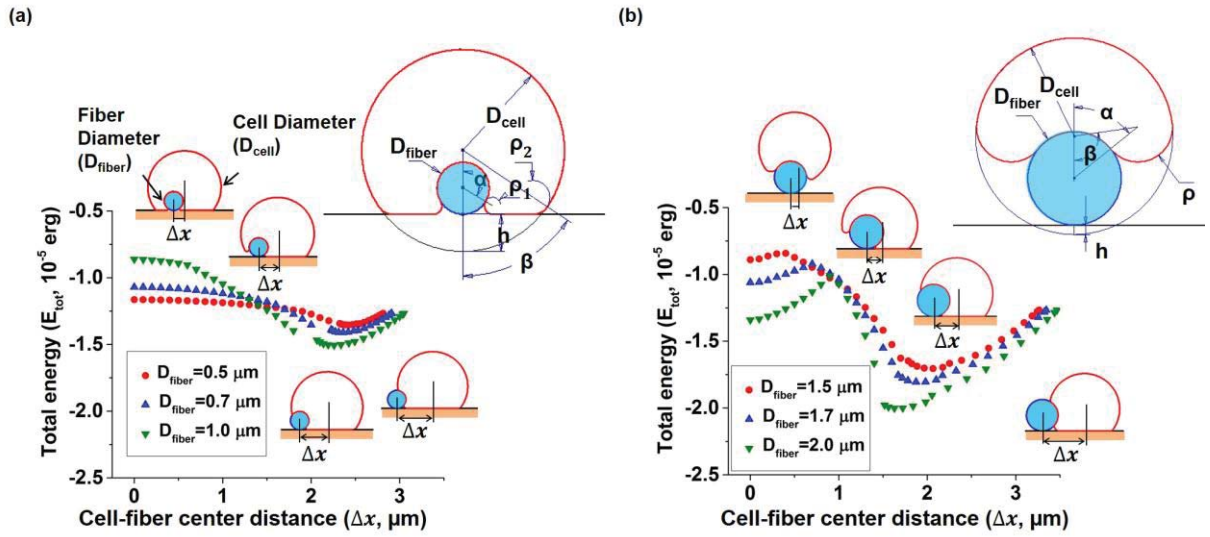

Figure 4. 1 Total energy ($\boldsymbol{E_{\text{tot}}}$) of *C. albicans* yeast cell interacting with a single fiber of diameters of (a) 0.5-1.0 μm and (b) 1.5-2.0 μm vs. cell-fiber center distance ($\boldsymbol{\Delta x}$) with $\boldsymbol{w_{\text{ad}}}$=77 mJ m^{-2} and $\boldsymbol{k_{str}}$=416 mN/m. In this case, D_{crit}=1.2 μm. The inset cartoons show cell shape (and relevant geometrical parameters) for various fiber diameter and cell-fiber distances.

After analyzing the case of a cell interacting with a single fiber, the model was extended to a cell interacting with two fibers when the fiber edge-to-edge spacing (S) is smaller than the cell diameter (D_{cell}). E_{tot} of one cell interacting with two fibers was calculated from E_{tot} of a cell interacting with each of the two fibers separately, with the assumption that cell deformation caused by a fiber is confined to the vicinity of the fiber and is much smaller than overall cell surface area change (see supplementary information section 3.4). If two fibers (a and b) are placed under the cell, the difference in total energy between the two fiber case, $E_{\text{tot}}(ab)$, and the case where the cell rests on a flat surface ($E_{\text{tot}}(flat)$) is given by Eq. (13).

$$E_{\text{tot}}(ab) - E_{\text{tot}}(flat) = [E_{\text{tot}}(a) - E_{\text{tot}}(flat)] + [E_{\text{tot}}(b) - E_{\text{tot}}(flat)] \quad (13)$$

which simplifies to:

$$E_{\text{tot}}(ab) = E_{\text{tot}}(a) + E_{\text{tot}}(b) - E_{\text{tot}}(flat) \quad (14)$$

If the fiber spacing is equal to or smaller than S_{min}, where $S_{\text{min}} = D_{\text{cell}}/2 - D_{\text{fiber}}$, then the cell can rest on more than two fibers and Eq (14) does not apply. Here we consider contact with not more than two fibers such that $S > S_{\text{min}}$.

Since E_{tot} of the cell varies with its location relative to the fibers, we define the spatially-averaged E_{tot} (denoted as $\overline{E_{\text{tot}}}$) to represent each surface pattern (i.e. nanofiber coating of different diameters and separation distances). We assume that the possibility of a cell initially contacting the patterned substrate is equal in every location, so $\overline{E_{\text{tot}}}$ is calculated as (see supplementary information section 3.5):

$$\overline{E_{\text{tot}}} = \frac{1}{A_s} \oint E_{\text{tot}} dA_s = \frac{1}{N} \sum_i^N E_{\text{tot}}(i) \quad (15)$$

for a sufficiently large number, N, of equal area increments, where $E_{\mathrm{tot}}(i)$ is the total energy of the cell adherent to the patterned surface at a position with the distance of the cell centroid and one fiber centerline of $\Delta x(i)$, for $0 \leq \Delta x(i) \leq S + D_{\mathrm{fiber}}$.

In order to generalize the analysis to different cell sizes, we normalized the fiber diameter and spacing to the cell diameter (i.e. $D_{\mathrm{fiber}}/D_{\mathrm{cell}}$, S/D_{cell}). Furthermore, a new non-dimensional parameter Π was introduced to represent ratio of the stretching modulus (a measure of the cell wall stiffness) to the work of adhesion (a measure of interaction between the cell wall and the substrate).

$$\Pi = k_{\mathrm{str}}/w_{\mathrm{ad}} \tag{16}$$

In order to quantify the influence of nanofiber addition on the total energy of the adherent cell, the spatially- averaged total energy of the cell attached on nanofiber-coated surfaces was normalized by the total energy of the cell adhered on the flat surface ($\overline{E_{\mathrm{tot}}}/E_{\mathrm{tot}}(flat)$). A value of $\overline{E_{\mathrm{tot}}}/E_{\mathrm{tot}}(flat) < 1$ indicates that, on average, the patterned surface exhibits a less negative value for E_{tot} than does an unpatterned (flat) surface and thus is less favorable for adhesion. As shown in Figure 4.2, the spatially-averaged normalized total energy has a minimum value. For instance, when Π = 5.0 and S/D_{cell} =0.48, the spatially-averaged normalized total energy reaches the minimum value at $D_{\mathrm{fiber}}/D_{\mathrm{cell}}$ = 0.29. For a given range of $D_{\mathrm{fiber}}/D_{\mathrm{cell}}$, the slope around the minimum is a strong function of the Π value but it also depends on S/D_{cell}. For a fixed S/D_{cell}, the normalized total energy is more sensitive to changes of $D_{\mathrm{fiber}}/D_{\mathrm{cell}}$ at higher Π values. A higher Π value implies either a stiffer cell wall (higher k_{str}) or a lower cell-substrate adhesion strength (lower w_{ad}). This indicates stiffer cells or cells with weaker adhesion are more sensitive to the surface pattern size change. For a fixed Π, the change of the normalized total energy is more significant with a smaller

S/D_{cell} since the nanofiber density (number of nanofibers per surface area) is higher with smaller S/D_{cell}.

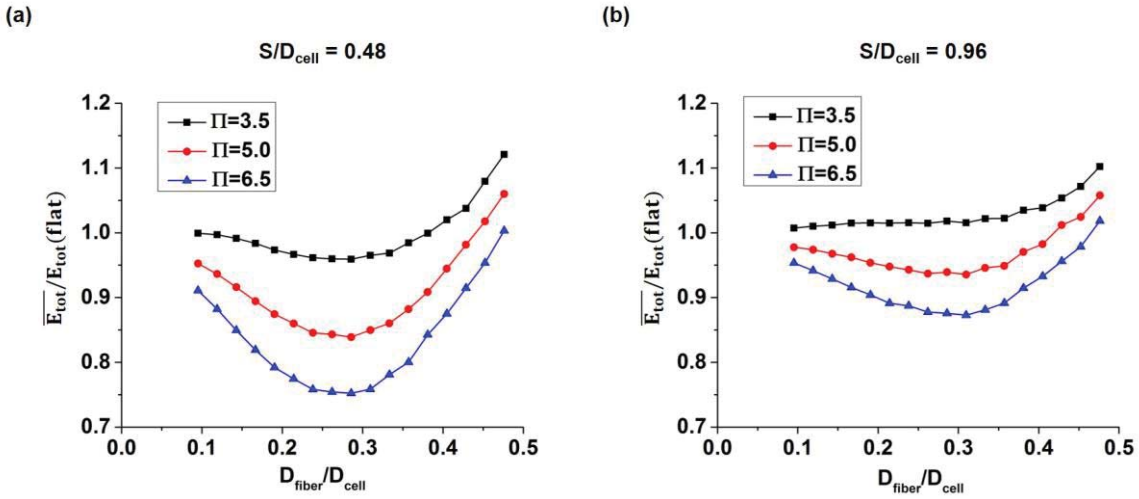

Figure 4. 2 Normalized total energy ($\overline{E_{\mathrm{tot}}}/E_{\mathrm{tot}}(flat)$) of a *C. albicans* yeast cell on nanofiber-textured substrate vs. normalized fiber diameter ($D_{\mathrm{fiber}}/D_{\mathrm{cell}}$) for Π=3.5, 5.0, and 6.5 and **(a)** S/D_{cell}=0.48 or **(b)** S/D_{cell}=0.96.

4.4.2 Experimental validation with PS nanofiber-coated PS substrate

As shown in Table 1, contact angles of the yeast film, PS substrate, and PS fiber material with water, formamide and diiodomethane were measured. From the contact angle measurements and Eq. (12), surface energy (γ) values and their corresponding dispersive (γ^{d}) and polar (γ^{p}) components were calculated. Work of adhesion (w_{ad}) between the yeast cell and the relevant material were calculated from Eq. (4).

The Young's modulus of *C. albicans* yeast was taken to be 1.6 MPa, and the average cell wall thickness was taken to be 260 nm as previously reported in the literature [128,129]. Using these values, the stretching modulus, k_{str}, was determined from Eq. (6) to be 416 mN/m.

	Contact angle (degree)			γ^D (mJ m^{-2})	γ^P (mJ m^{-2})	γ (mJ m^{-2})	w_{ad} with yeast (mJ m^{-2})
	Water	**Formamide**	**Diiodomethane**				
Yeast	56.4±7.9	59.5±8.4	37.4±6.8	28.3±6.9	17.8±5.4	46.1±8.8	-----
PS substrate	88.8±1.0	60.9±1.4	22.9±1.9	44.0±2.0	0.6±0.2	44.6±2.0	77.3
PS fiber material	82.7±0.6	66.7±2.3	26.0±1.5	37.5±4.4	2.4±1.1	39.9±4.5	78.3
PU catheter	82.3±0.2	64.0±3.7	80.3±1.8	15.1±1.3	11.3±1.1	26.4±1.7	69.7
Latex catheter	110.1±2.7	89.2±0.5	90.0±0.6	13.2±1.0	1.1±0.3	14.3±1.0	47.5
Silicone catheter	112.8±1.9	104.0±1.0	90.4±0.8	10.3±0.8	0.9±0.2	11.2±0.8	42.1

Table 4. 1 Contact angles, surface energies (γ^D, γ^P, γ) and work of adhesion (w_{ad}) of yeast, PS sheet, PS fiber material, PU catheter, latex catheter, and silicone catheter.

Using the calculated w_{ad} for PS substrate and k_{str} values, Π is calculated to be 5.4, the normalized total energy has a minimum value at D_{fiber}/D_{cell} = 0.29 for S/D_{cell} =0.48 (S=2 μm, Figure 4.3a). From the dynamic retention assay experiment, the cell attachment density on fiber-coated surfaces was normalized to the cell attachment density on the flat surface and plotted against D_{fiber}/D_{cell} for S/D_{cell} =0.48 (Figure 4.3b). The fiber diameters were separated to three different groups (D_{fiber}/D_{cell} = 0.12-0.24, 0.24-0.36 and 0.36-0.48), and the normalized cell attachment densities were averaged in each group. A one-way ANOVA test demonstrated significant differences between the groups of D_{fiber}/D_{cell} = 0.12-0.24, D_{fiber}/D_{cell} = 0.24-0.36 and D_{fiber}/D_{cell} = 0.36-0.48 (Figure 4.3b). The SEM images of the substrates (shown in Figure 4.3c) after the experiment displayed the difference

in cell attachment density between the flat surface, 1.2 µm fiber coated surface (D_{fiber}/D_{cell}=0.29), and 2.0 µm fiber coated surface (D_{fiber}/D_{cell}=0.48). The experimental results confirmed the model's predicted behavior that only a specific range of fiber diameters could reduce the cell attachment density while other fiber diameters increase it. This is because when the fiber diameters are either too small or too large, the cell's total energy decreases as it utilizes the fiber to increase the adhesion area (reduce E_{ad}) with minimal stretching (no significant increase in E_{str}).

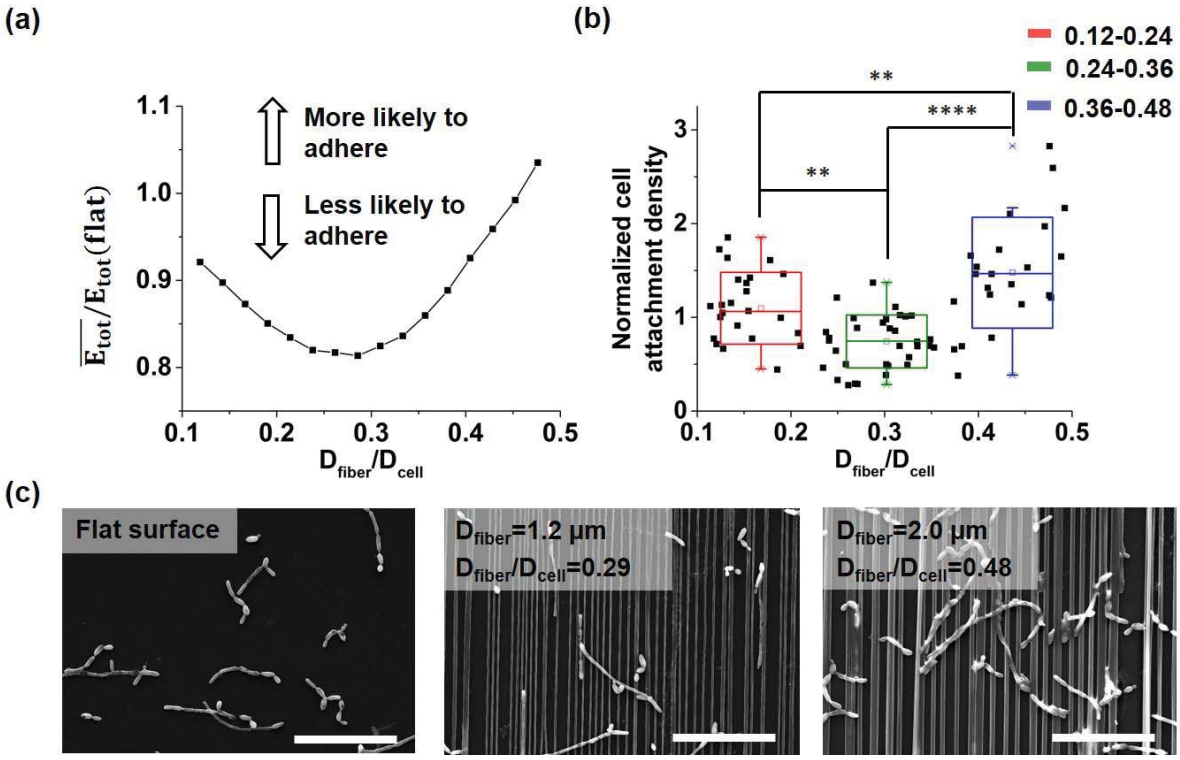

Figure 4. 3 (a) $\overline{E_{tot}}/E_{tot}(flat)$ vs. D_{fiber}/D_{cell} for fiber edge-to-edge spacing of 2.0 µm (S/D_{cell}=0.48), (b) Normalized cell attachment density vs. D_{fiber}/D_{cell}, N=80. Comparison of normalized cell attachment density of fiber groups of D_{fiber}/D_{cell} =0.12-0.24, 0.24-0.36, and 0.36-0.48, ****p-value<0.0001, **p-value<0.01, (c) SEM images of *C. albicans* on flat, D_{fiber}=1.0 µm and D_{fiber}=2.0 µm fiber textured surfaces. All scale bars are 50 µm.

4.4.3 Experimental validation with PS nanofiber-coated catheters

To further investigate the applicability of our biophysical model, the effect of the PS nanofiber coating on the density of cell attachment to the catheters was explored. Commercially available latex and silicone urinary catheters and PU femoral central vein catheter were used in this study. Contact angles of these catheter materials with water, formamide, and diiodomethane were measured, as shown in Table 1. From these contact angle measurements, γ^d, γ^p and γ were calculated using Eq. (12). The work of adhesion, w_{ad}, between the yeast cell and the PU, latex, and silicone catheters were calculated to be 69.7 mJ m^{-2}, 47.5 mJ m^{-2} and 42.1 mJ m^{-2}, respectively. As described in the previous section, w_{ad} between the yeast cell and the PS fiber material is 78.3 mJ m^{-2} and k_{str} of the cell wall is 416 mN/m. The simulation results for the spatially-averaged normalized total energy ($\overline{E_{\mathrm{tot}}}/E_{\mathrm{tot}}(flat)$) against the non-dimensional fiber diameter ($D_{\mathrm{fiber}}/D_{\mathrm{cell}}$) for the PU, latex and silicone catheters coated with PS fibers are shown in Figure 4.4a. Only the PU catheter has a region of $D_{\mathrm{fiber}}/D_{\mathrm{cell}}$ values that results in a total energy that is less favorable for adhesion ($\overline{E_{\mathrm{tot}}}/E_{\mathrm{tot}}(flat)$<1), compared with the unpatterned PU catheter. On the other hand, both the latex and silicone catheters have total energy values that are more favorable for adhesion with the deposited PS nanofibers for all $D_{\mathrm{fiber}}/D_{\mathrm{cell}}$. This is because w_{ad} for the PS fiber (78.3 mJ m^{-2}) is closer to w_{ad} for the PU (69.7 mJ m^{-2}) catheter but much higher than the latex (47.5 mJ m^{-2}) and silicone (42.1 mJ m^{-2}) catheters. As a result, for the PU catheter, the effects of surface patterning are able to overcome the higher w_{ad} and yield a minimum for the spatially-averaged normalized total energy in the $D_{\mathrm{fiber}}/D_{\mathrm{cell}}$ region of 0.24-0.29, which corresponds to fiber diameters of 1.0-1.2 μm.

The model predictions were validated by applying PS fibers with diameters of 1.0-1.2 μm on the PU, latex and silicone catheter surfaces using the STEP technique. As shown in Figure 4.4b, the cell attachment density normalized by the respective unpatterned surface attachment density is

0.77 ± 0.20 for the PU catheter, 1.22 ± 0.22 for the latex catheter, and 1.25 ± 0.19 for the silicone catheter. The experimental results are in agreement with the prediction from the model. The deposition of the PS fibers is only effective in mitigating cell attachment on the PU catheter; however, introducing PS nanofibers onto the latex and silicone catheters increases the cell attachment density since the introduction of fibers increases the work of adhesion between the cell and the substrate. The SEM images in Figure 4.4c show the cell attachment density in the presence and absence of the fibers on the different catheters.

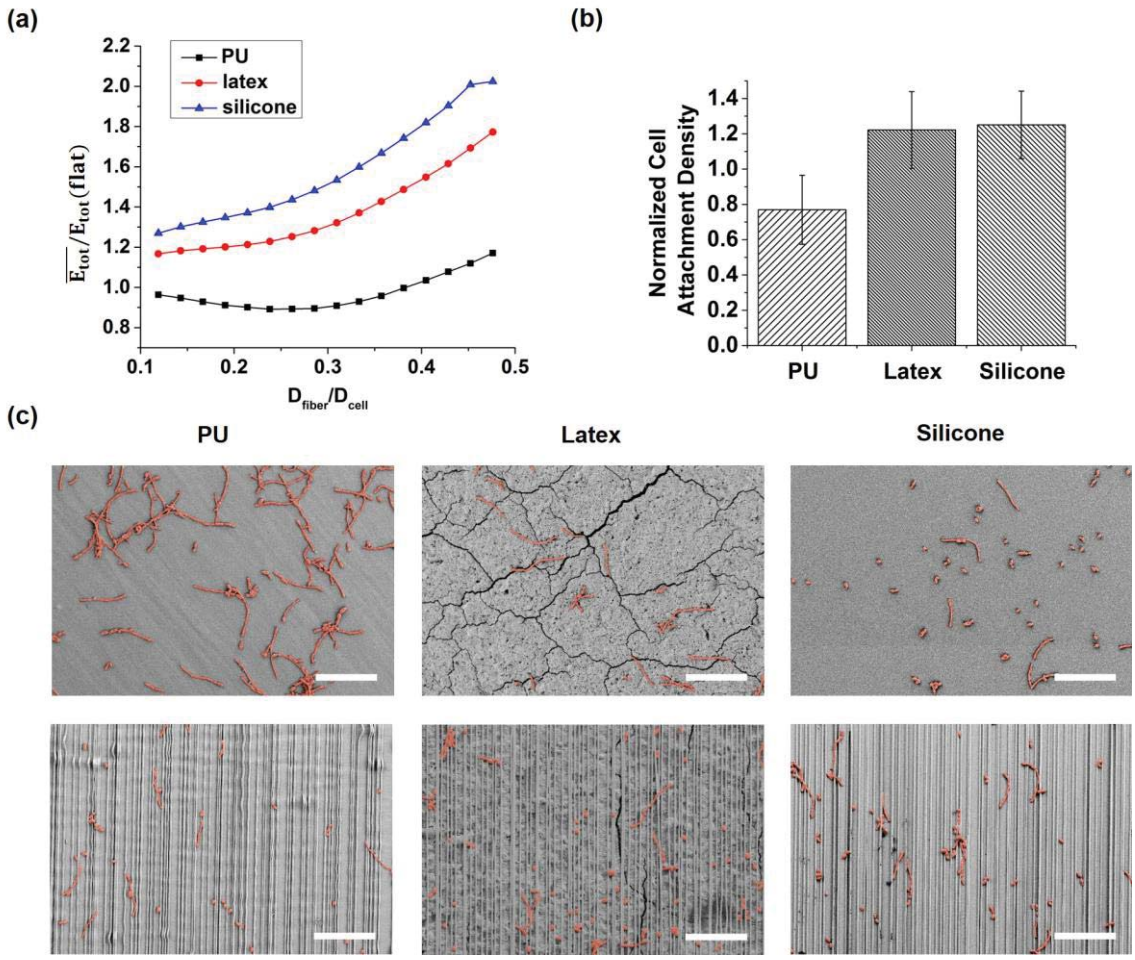

Figure 4. 4 (a) Simulation result of $\overline{\boldsymbol{E_{tot}}}/\boldsymbol{E_{tot}}(\boldsymbol{flat})$ vs. D_{fiber}/D_{cell} for PU, latex and silicone catheters coated with PS nanofibers, (b) Normalized cell attachment density for PU, latex and silicone catheters, N=12, 10, 11, respectively, (c) SEM images of *C. albicans* on non-textured and nanofiber-textured catheter surfaces.

4.5 Discussion

The biophysical model developed through this work utilizes a description of the total energy (adhesion energy and stretching energy) of a single adherent yeast cell to predict the effect of depositing nanofibers on the cell attachment density. Results from the model show that patterning the surface with nanofibers can increase or decrease the cell attachment density, depending on the substrate and fiber materials as well as the fiber diameter and spacing. For example, depositing fibers made of a material that causes significant increase in w_{ad} will lead to a reduced total energy of the adherent cell and increased cell attachment density (e.g. depositing PS fibers on latex or silicone catheters). Even when depositing fibers of the same material as the substrate (e.g. depositing PS fibers on PS substrate), not all fiber diameters will increase the total energy and mitigate cell attachment (Figure 4.3). In the application of depositing nanofibers on catheter surfaces, if the fiber material is the same as the catheter material (e.g. depositing PU fibers on the PU catheter), the effect of the pattern geometry will be more pronounced (Figure 4.5). As shown in Figure 4.2, the normalized total energy is more sensitive to changes of $D_{\text{fiber}}/D_{\text{cell}}$ at higher Π values and silicone has the highest Π value ($\Pi = k_{\text{str}}/w_{\text{ad}}$), so the minimum normalized total energy for silicone is the lowest (i.e. $\overline{E_{\text{tot}}}/E_{\text{tot}}(flat)$ =0.61 at $D_{\text{fiber}}/D_{\text{cell}}$=0.24-0.26 for S/$D_{\text{cell}}$=0.48). When designing nanostructure modified surfaces, the surface energy of the nanostructures' material should be as low as possible. For a particular coating material, the biophysical model can predict the optimal feature size (e.g. nanofiber diameter) and configuration (fiber spacing) that would maximize the E_{tot} to ensure the best antifouling effect. This biophysical model can be extended to other nanostructures with appropriate geometrical calculations. Further, since this model is generalized through the use of non-dimensional parameters, it can be applied

to other microorganisms and substrates with experimentally measured k_{str}, w_{ad} , and surface energy values.

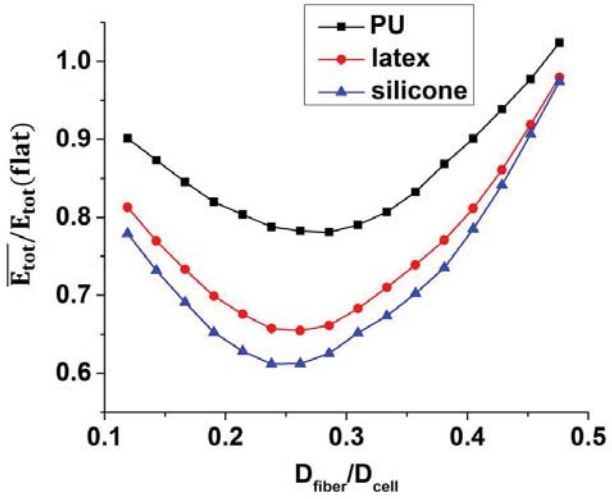

Figure 4. 5 Simulation result of $\overline{\boldsymbol{E_{tot}}}/\boldsymbol{E_{tot}}(\boldsymbol{flat})$ vs. D_{fiber}/D_{cell} for PU, latex and silicone catheters coated with PU, latex and silicone nanofibers respectively. S/D_{cell}=0.48.

4.6 Conclusion

We have developed and experimentally validated a biophysical model that incorporated cell wall stretching in *C. albicans* yeast adhesion on nanofiber-coated surfaces. Our model determines the cell total energy (adhesion energy and stretching energy) as a function of the fiber diameter and spacing. Dynamic retention assay of *C. albicans* on PS fiber coated PS substrates was carried out to test our hypothesis that the total energy of the adherent cell is predictive of the population-level cell attachment density. We show that the surface design that yielded the highest total energy yields the lowest cell attachment density. Guided by our biophysical model, we patterned PU, latex and silicone catheters with PS fibers, and demonstrated good agreement between the model and the experiment. This biophysical model in conjunction with the introduced non-dimensional parameters can to be applied for other microorganisms and substrate materials to control biofilm

formation on abiotic surface (e.g. mitigation of biofilms on biomedical devices). This biophysical model can be extended to other nanostructures for efficient *ab initio* biomaterial design, either to decrease pathogenic microbial adhesion or increase beneficial microbial adhesion.

4.7 Supplementary Information

4.7.1 Supplementary figures

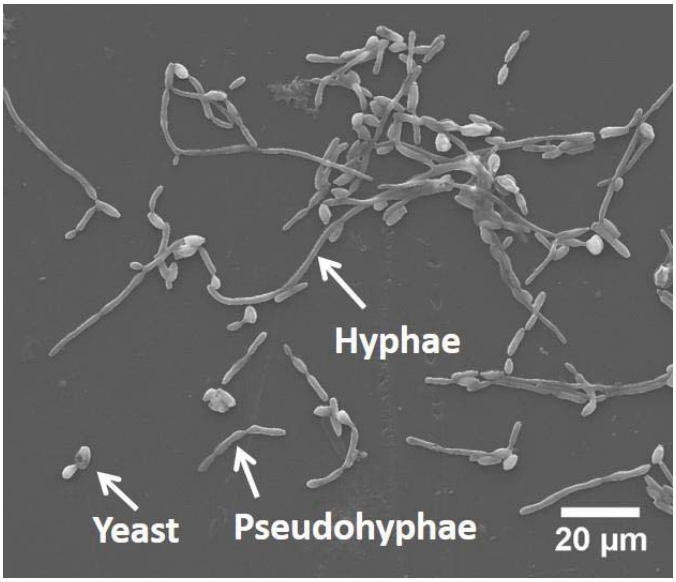

Figure S4. 1 SEM images of *C. albicans* in yeast, pseudohyphal, and hyphal forms.

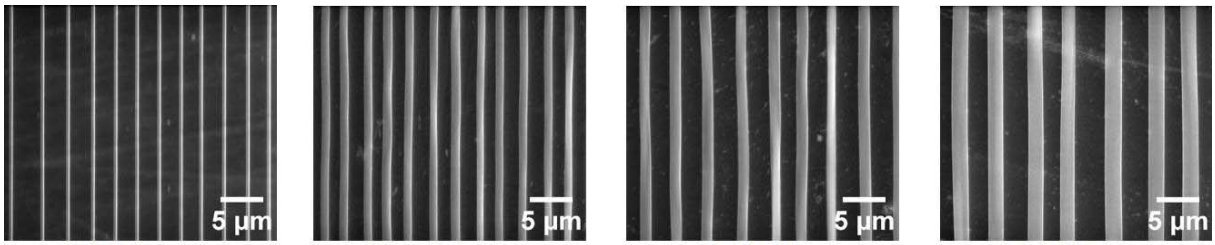

Figure S4. 2 SEM images of nanofibers with diameters of (a) 0.5 μm, (b) 0.9 μm, (c) 1.4 μm, and (d) 2.0 μm and spacing of 2.0 μm. All scale bars are 5 μm.

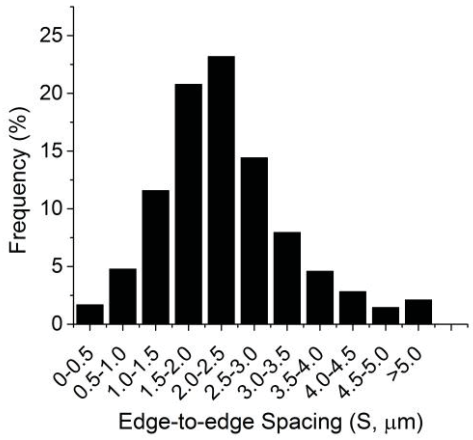

Figure S4. 3 Distribution of fiber edge-to-edge spacing. N=11,716.

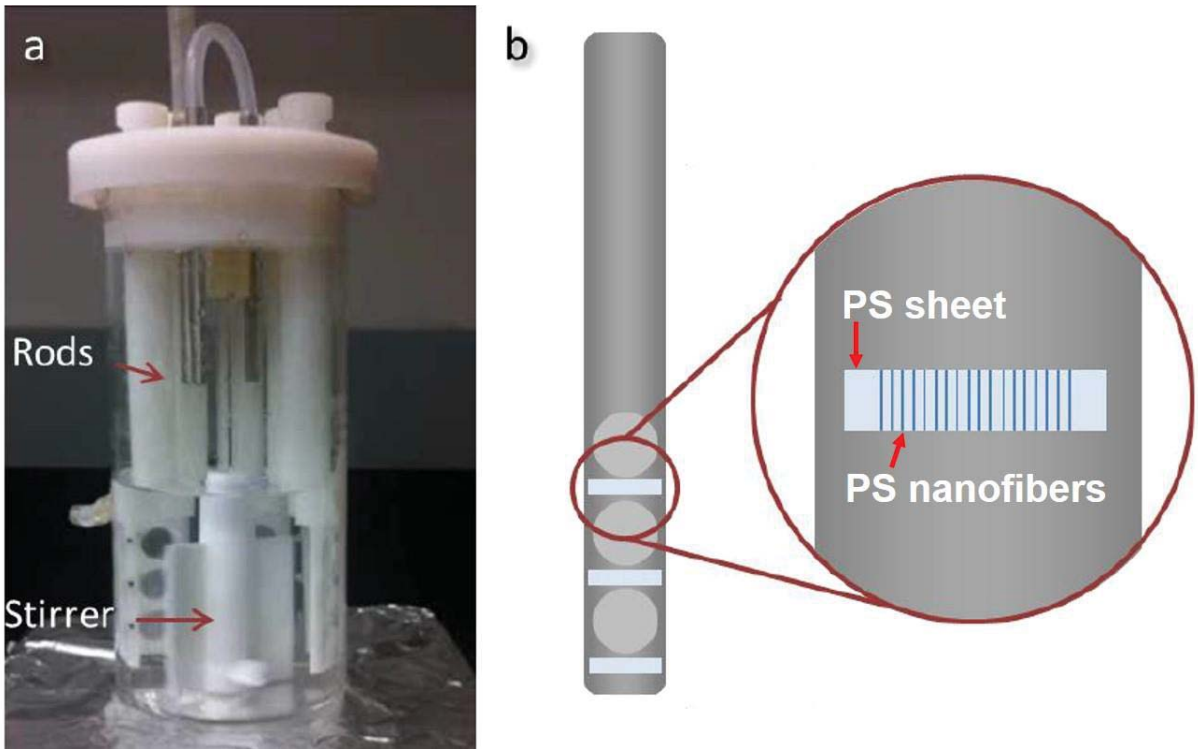

Figure S4. 4 a, CDC biofilm reactor. b, illustration of close-up of a rod mounted with nanofiber textured samples.

4.7.2 Bending energy (E_c)

E_c can be calculated by integrating the bending energy per unit area (e_c) over the cell surface:

$$E_c = \oint e_c dA \quad \text{(S1)}$$

An approximation of e_c is given by Helfrich[130]:

$$e_c = \frac{1}{2}k_c(\kappa_1 + \kappa_2 - 2c_0)^2 + \overline{k_c}\kappa_1\kappa_2 \quad \text{(S2)}$$

Where κ_1 and κ_2 are the principal curvatures, c_0 is the spontaneous curvature, k_c is the bending modulus, which is estimated to be $k_c = 20k_BT = 8.6 \times 10^{-20}$ J (37 ºC), $\overline{k_c}$ is the saddle-splay modulus, and the product $\kappa_1\kappa_2$ gives the Gaussian curvature. Based on Gauss-Bonnet theorem, the integral of Gaussian curvature over a closed surface is equal to $2\pi\chi$, in which χ, the Euler characteristic, is topologically invariant. Topological change in cell deformation during adhesion to a surface is not significant [131], therefore the second term $\overline{k_c}\kappa_1\kappa_2$ is ignored. Thus, k_c is the only modulus in the Eq. (S2) and a new length scale λ can be introduced to compare the relative value of E_c to E_{ad}:

$$\lambda = \sqrt{k_c/w_{ad}} \quad \text{(S3)}$$

When λ is much smaller than the scale of the cell, E_c is negligible compared to E_{ad}. Here, this length (λ) is calculated to be 1 nm, which is three magnitudes smaller than the radius of the cell (2.1 μm), allowing E_c to be ignored in our study.

4.7.3 Total energy calculation for a single cell adhered to a flat surface

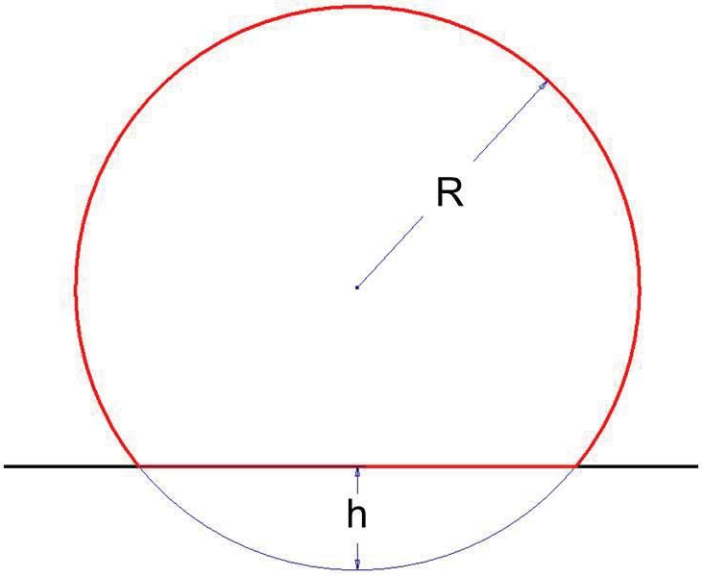

Figure S4. 2 Section view of an individual cell on flat surface.

To calculate E_{tot}:

$A_{ad} = \pi(R^2 - (R - h)^2)$

$A = 2\pi R(2R - h) + \pi(R^2 - (R - h)^2)$

With the constraint that the cell volume remains constant:

$V = \frac{4\pi}{3}R^3 - \pi h^2\left(R - \frac{h}{3}\right) = \frac{4\pi}{3}{R_0}^3$

4.7.4 Total energy calculation for a single cell adhered to a single fiber with small diameter ($D_{fiber} \leq D_{crit}$)

Geometry I:

The following geometric and cell volume constraints are present:

$(a + \rho_1)cos\alpha_1 + a - \rho_1 = 0$

$(a + \rho_2)cos\alpha_2 + a - \rho_2 = 0$

$$V \approx \frac{4\pi}{3}R^3 - \pi h^2\left(R - \frac{h}{3}\right) - \left(\frac{1}{2}\alpha_1 a^2 + \frac{1}{2}(a+\rho_1)^2 \sin\alpha_1 - \frac{1}{2}\alpha_1{\rho_1}^2 + \frac{1}{2}\alpha_2 a^2 + \right.$$

$$\left.\frac{1}{2}(a+\rho_2)^2 \sin\alpha_2 - \frac{1}{2}\alpha_2{\rho_2}^2\right)\left(\sqrt{R^2 - \left(\sqrt{b^2 + (R-h-a)^2} - a\right)^2} + \right.$$

$$\left.\sqrt{R^2 - (R-h)^2 - (b + (a+\rho_1)\sin\alpha_1)^2}\right) = \frac{4\pi}{3}{R_0}^3$$

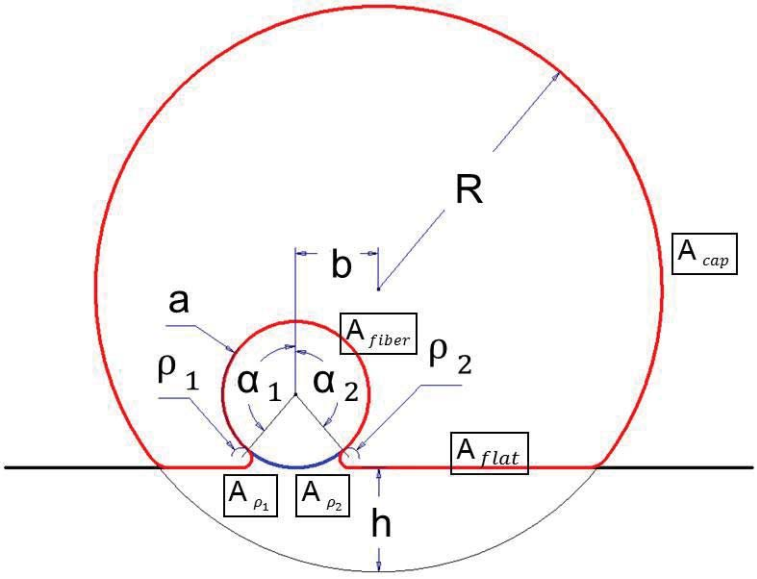

Figure S4. 3 Section view of an individual cell adherent to a single fiber with smaller diameter (Geometry I).

To calculate E_{tot}, the following surface areas need to calculated as:

$$A_{ad} = A_{flat} + A_{fiber}$$

$$A = A_{cap} + A_{flat} + A_{fiber} + A_{rho1} + A_{rho2}$$

where

$$A_{flat} = (R^2 - (R-h)^2)\cos^{-1}\frac{b+(a+\rho_1)\sin\alpha_1}{\sqrt{R^2-(R-h)^2}} - (b + (a +$$

$$\rho_1)\sin\alpha_1)\sqrt{R^2 - (R-h)^2 - (b + (a+\rho_1)\sin\alpha_1)^2} + \left(\pi - \cos^{-1}\frac{b-(a+\rho_2)\sin\alpha_2}{\sqrt{R^2-(R-h)^2}}\right)(R^2 -$$

$$(R-h)^2) + (b - (a+\rho_2)sin\alpha_2)\sqrt{R^2 - (R-h)^2 - (b + (a-\rho_2)sin\alpha_2)^2}$$

$$A_{fiber} = 2a\int_{-\alpha_1}^{\alpha_2}\sqrt{R^2-(R-h-a)^2-a^2-b^2+2a(R-h-a)\cos\theta+2ab\sin\theta}$$

$$A_{cap} \approx 2\pi R(2R-h)-2\left(\frac{1}{2}\alpha_1 a^2+\frac{1}{2}(a+\rho_1)^2\sin\alpha_1-\frac{1}{2}\alpha_1{\rho_1}^2+\frac{1}{2}\alpha_2 a^2+\frac{1}{2}(a+\rho_2)^2\sin\alpha_2-\frac{1}{2}\alpha_2{\rho_2}^2\right)\frac{\left(\sin^{-1}\frac{b+a}{\sqrt{R^2-(R-h)^2}}-\sin^{-1}\frac{b-a}{\sqrt{R^2-(R-h)^2}}\right)\sqrt{R^2-(R-h-a)^2}}{2a}$$

$$A_{rho1} = 2\rho_1\int_0^{\alpha_1}\sqrt{\begin{matrix}R^2-(R-h-\rho_1)^2-{\rho_1}^2-(b+(a+\rho_1)\sin\alpha_1)^2\\-2\rho_1(R-h-\rho_1)\cos\theta+2\rho_1(b+(a+\rho_1)\sin\alpha_1)\sin\theta\end{matrix}}$$

$$A_{rho2} = 2\rho_2\int_0^{\alpha_2}\sqrt{\begin{matrix}R^2-(R-h-\rho_2)^2-{\rho_2}^2-(b+(a+\rho_2)\sin\alpha_2)^2\\-2\rho_2(R-h-\rho_2)\cos\theta+2\rho_2(b+(a+\rho_2)\sin\alpha_2)\sin\theta\end{matrix}}$$

Geometry II:

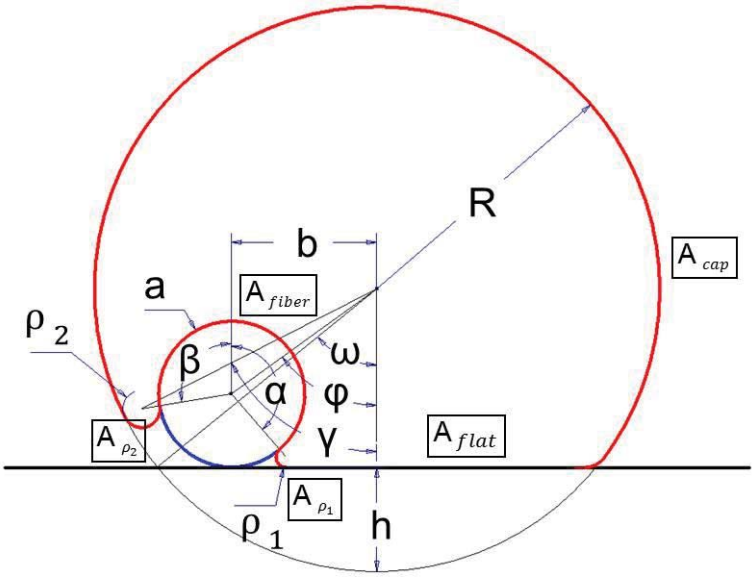

Figure S4. 4 Section view of an individual cell adherent to a single fiber with smaller diameter (Geometry II).

The following geometric and cell volume constraints are present

$$(a+\rho_1)cos\alpha+a-\rho_1=0$$

$$(R-\rho_2)\sin\gamma-(a+\rho_2)\sin\beta-b=0$$

$$(R-\rho_2)\cos\gamma+(a+\rho_2)\cos\beta+a+h-R=0$$

$$\varphi=cos^{-1}\frac{R-h-a}{\sqrt{b^2+(R-h-a)^2}}$$

$$\omega=cos^{-1}\frac{R-h}{R}$$

$$V\approx\frac{4\pi}{3}R^3-\pi h^2\left(R-\frac{h}{3}\right)-\Bigg(\pi a^2+\frac{1}{2}(a+\rho_1)^2\sin\alpha-\frac{\pi-\alpha}{2}a^2-\frac{\alpha}{2}{\rho_1}^2+\Bigg(\frac{\gamma-cos^{-1}\frac{R-h}{R}}{2}R^2-$$

$$\frac{1}{2}\sqrt{b^2+(R-h-a)^2}(a+\rho_2)\sin\left(\pi-\beta-\tan^{-1}\frac{b}{R-h-a}\right)-\frac{1}{2}\left(a-\frac{\sqrt{R^2-(R-h)^2}-b}{\tan\left(cos^{-1}\frac{R-h}{R}\right)}\right)b+$$

$$\frac{1}{2}\frac{\left(\sqrt{R^2-(R-h)^2}-b\right)^2}{\tan\left(cos^{-1}\frac{R-h}{R}\right)}-\frac{\pi-\beta}{2}a^2-\frac{\beta+\gamma}{2}{\rho_2}^2\Bigg)\Bigg)\sqrt{R^2-\left(\sqrt{b^2+(R-h-a)^2}-a\right)^2}=\frac{4\pi}{3}{R_0}^3$$

To calculate E_{tot}, the following surface areas need to calculated as:

$$A_{ad}=A_{flat}+A_{fiber}$$

$$A=A_{cap}+A_{flat}+A_{fiber}+A_{rho1}+A_{rho2}$$

where

$$A_{flat}=\left(\pi-\cos^{-1}\frac{b-(a+\rho_1)\sin\alpha}{\sqrt{R^2-(R-h)^2}}\right)(R^2-(R-h)^2)+(b-(a+$$

$$\rho_1)\sin\alpha)\sqrt{R^2-(R-h)^2-(b-(a+\rho_1)\sin\alpha)^2}$$

$$A_{fiber}=2a\int_{-\beta}^{\alpha}\sqrt{R^2-(R-h-a)^2-a^2-b^2+2a(R-h-a)\cos\theta+2ab\sin\theta}$$

$$A_{cap}\approx 2\pi R(2R-h)-2\left(\pi a^2+\frac{1}{2}(a+\rho_1)^2\sin\alpha-\frac{\pi-\alpha}{2}a^2-\right.$$

$$\left.\frac{\alpha}{2}{\rho_1}^2\right)\frac{\left(\sin^{-1}\frac{b+a}{\sqrt{R^2-(R-h-a)^2}}-\sin^{-1}\frac{b-a}{\sqrt{R^2-(R-h-a)^2}}\right)\sqrt{R^2-(R-h-a)^2}}{2a}-2\left(\frac{\gamma-\omega}{2}R^2-\right.$$

$$\frac{1}{2}\sqrt{b^2+(R-h-a)^2}(a+\rho_2)\sin(\pi-\beta-\varphi)-\frac{1}{2}\left(a-\frac{\sqrt{R^2-(R-h)^2}-b}{\tan\omega}\right)b+\frac{1}{2}\frac{\left(\sqrt{R^2-(R-h)^2}-b\right)^2}{\tan\omega}-$$

$$\frac{\pi-\beta}{2}a^2-\frac{\beta+\gamma}{2}{\rho_2}^2\Bigg)\Bigg(\left(R\sin\gamma+\sqrt{R^2-(R-h)^2}\right)\frac{\cos^{-1}\frac{R\sin\gamma-\rho_2\sin\gamma-\rho_2\sin\beta+b}{R\sin\gamma+\sqrt{R^2-(R-h)^2}}}{\rho_2\sin\gamma+\rho_2\sin\beta+\sqrt{R^2-(R-h)^2}-b}\Bigg)$$

$$A_{rho1}=2\rho_1\int_0^{\alpha}\sqrt{\begin{matrix}R^2-(R-h-\rho_1)^2-{\rho_1}^2-(b-(a+\rho_1)\sin\alpha)^2\\-2\rho_1(R-h-\rho_1)\cos\theta-2\rho_1(b-(a+\rho_1)\sin\alpha)\sin\theta\end{matrix}}$$

$$A_{rho2}=2\rho_2\int_0^{\rho_2}\sqrt{R^2-(R-\rho_2)^2-{\rho_2}^2-2\rho_2(R-\rho_2)\cos\gamma\cos\theta+2\rho_2(R-\rho_2)\sin\gamma\sin\theta}$$

Geometry III:

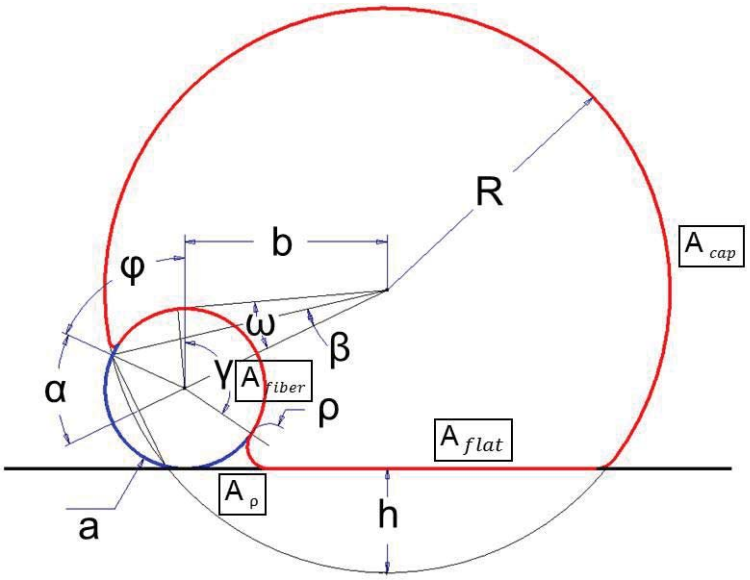

Figure S4. 5 Section view of an individual cell adherent to a single fiber with smaller diameter (Geometry III).

The following geometric and cell volume constraints are present

$$a\sin\alpha-R\sin\beta=0$$

$$(a+\rho)\cos\gamma+a-\rho=0$$

$$b = \sqrt{(R\cos\beta - a\cos\alpha)^2 - (R-h-a)^2}$$

$$\varphi + \alpha + cos^{-1}\frac{R-h-a}{\sqrt{(R-h-a)^2+b^2}} - \pi = 0$$

$$\omega = \sin^{-1}\frac{a}{R\cos\beta - a\cos\alpha}$$

$$V \approx \frac{4\pi}{3}R^3 - \pi h^2\left(R - \frac{h}{3}\right) - \pi\big(R(1-\cos\beta)\big)^2\left(R - \frac{R(1-\cos\beta)}{3}\right) - \Big((\pi-\alpha)a^2 +$$

$$a\sin\alpha\, a\cos\alpha + \frac{1}{2}(a+\rho)^2\sin\gamma - \frac{\pi-\gamma}{2}a^2 - \frac{\gamma}{2}\rho^2\Big)\sqrt{R^2 - \left(\sqrt{b^2+(R-h-a)^2} - a\right)^2} =$$

$$\frac{4\pi}{3}{R_0}^3$$

To calculate E_{tot}, the following surface areas need to calculated as:

$$A_{ad} = A_{flat} + A_{fiber}$$

$$A = A_{cap} + A_{flat} + A_{fiber} + A_\rho$$

where

$$A_{flat} = \left(\pi - \cos^{-1}\frac{b-(a+\rho)\sin\gamma}{\sqrt{R^2-(R-h)^2}}\right)(R^2-(R-h)^2) + (b - (a +$$

$$\rho)\sin\gamma)\sqrt{R^2-(R-h)^2-(b-(a+\rho)\sin\gamma)^2}$$

$$A_{fiber} = 2a\int_{-\varphi}^{\gamma}\sqrt{R^2-(R-h-a)^2-a^2-b^2+2a(R-h-a)\cos\theta+2ab\sin\theta}$$

$$A_{cap} = 2\pi R(2R-h) - 4R^2\int_0^{\omega}\cos^{-1}\frac{\cos\theta(R\cos\beta-a\cos\alpha)-\sqrt{a^2-(R\cos\beta-a\cos\alpha)^2(\sin\theta)^2}}{R} +$$

$$4R^2\int_{\beta}^{\omega}\cos^{-1}\frac{\cos\theta(R\cos\beta-a\cos\alpha)+\sqrt{a^2-(R\cos\beta-a\cos\alpha)^2(\sin\theta)^2}}{R}$$

$$A_\rho = 2\rho\int_0^{\gamma}\sqrt{\begin{matrix}R^2-(R-h-\rho)^2-(b-(a+\rho)\sin\gamma)^2-\rho^2-\\2\rho(R-h-\rho)\cos\theta-2\rho(b-(a+\rho)\sin\gamma)\sin\theta\end{matrix}}$$

Geometry IV:

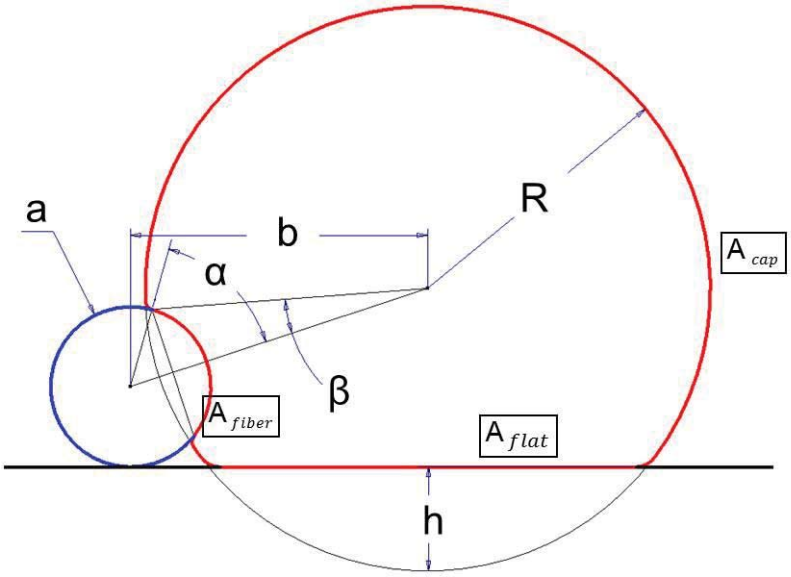

Figure S4. 6 Section view of an individual cell adherent to a single fiber with smaller diameter (Geometry IV).

The following geometric and cell volume constraints are present:

$$a \sin\alpha - R \sin\beta = 0$$

$$b = \sqrt{(a\cos\alpha + R\cos\beta)^2 - (R - h - a)^2}$$

$$V \approx \frac{4\pi}{3}R^3 - \pi h^2\left(R - \frac{h}{3}\right) - \pi\big(R(1-\cos\beta)\big)^2\left(R - \frac{R(1-\cos\beta)}{3}\right) - (\alpha a^2 -$$

$$a \sin\alpha\, a\cos\alpha)\sqrt{R^2 - (a\cos\alpha + R\cos\beta - a)^2} = \frac{4\pi}{3}{R_0}^3$$

To calculate E_{tot}, the following surface areas need to calculated as:

$$A_{ad} = A_{flat} + A_{fiber}$$

$$A = A_{cap} + A_{flat} + A_{fiber}$$

where

$$A_{flat} = \pi(R^2 - (R-h)^2)$$

$$A_{fiber} = 4a\int_0^{\alpha}\sqrt{R^2 - (a\cos\alpha + R\cos\cos\beta)^2 - a^2 + 2a(a\cos\alpha + R\cos\beta)\cos\theta}$$

$$A_{cap}$$

$$= 2\pi R(2R - h)$$

$$- 4R^2 \int_0^{\beta} \cos^{-1} \frac{cos\,\theta\,(a\cos\alpha + R\cos\beta) - \sqrt{a^2 - (a\cos\alpha + R\cos\beta)^2(\sin\theta)^2}}{R}$$

4.7.5 Total energy calculation for a single cell adhered to a single fiber with large diameter ($D_{fiber} > D_{crit}$)

Geometry I:

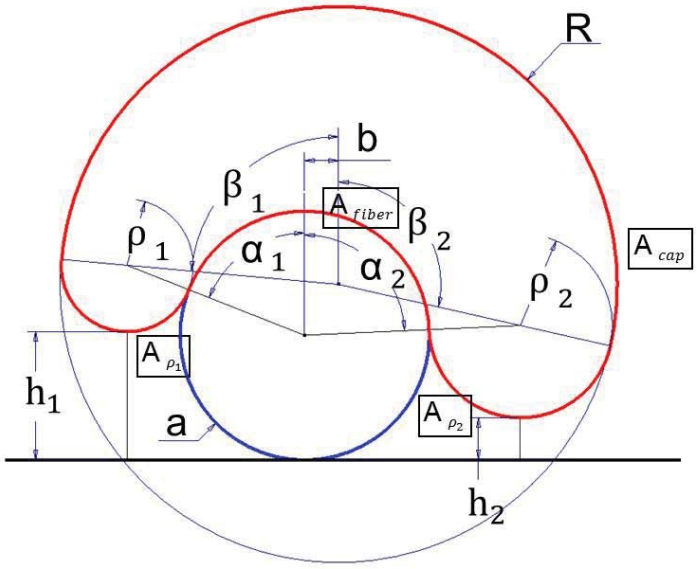

Figure S4. 7 Section view of an individual cell adherent to a single fiber with larger diameter (Geometry I).

The following geometric and cell volume constraints are present:

$$(a + \rho_1)\sin\alpha_1 + b - (R - \rho_1)\sin\beta_1 = 0$$

$$(a + \rho_2)\,sin\,\alpha_2 - b - (R - \rho_2)\,sin\,\beta_2 = 0$$

$$(R - \rho_1)\cos\beta_1 + (a + \rho_1)\cos\alpha_1 - (R - \rho_2)\cos\beta_2 - (a + \rho_2)\cos\alpha_2 = 0$$

$$(a + \rho_1)\cos\alpha_1 + a - \rho_1 - h1 = 0$$

$$(a+\rho_2)\cos\alpha_2 + a - \rho_2 - h2 = 0$$

$$V \approx \frac{4\pi}{3}R^3 - \left(\frac{\beta_1+\beta_2}{2}R^2 - \frac{1}{2}(a+\rho_1)(R-\rho_1)\sin(\pi-\alpha_1-\beta_1) - \frac{1}{2}(a+\rho_2)(R-\rho_2)\sin(\pi-\alpha_2-\beta_2) - \frac{\alpha_1+\beta_1}{2}{\rho_1}^2 - \frac{\alpha_2+\beta_2}{2}{\rho_2}^2 + \frac{\alpha_1+\alpha_2}{2}a^2\right)\frac{4}{3}R = \frac{4\pi}{3}{R_0}^3$$

To calculate E_{tot}, the following surface areas need to calculated as::

$$A_{ad} = A_{fiber}$$

$$A = A_{cap} + A_{fiber} + A_{rho1} + A_{rho2}$$

where

$$A_{fiber} = 2a\int_{-\alpha_1}^{\alpha_2}\sqrt{\begin{matrix}R^2 - a^2 - b^2 - \left((R-\rho_1)\cos\beta_1 + (a+\rho_1)\cos\alpha_1\right)^2 \\ +2ab\,sin\,\theta + 2a\left((R-\rho_1)\cos\beta_1 + (a+\rho_1)\cos\alpha_1\right)cos\,\theta\end{matrix}}$$

$$A_{cap} \approx 4\pi R^2 - 2\left(\frac{\beta_1+\beta_2}{2}R^2 - \frac{1}{2}(a+\rho_1)(R-\rho_1)\sin(\pi-\alpha_1-\beta_1) - \frac{1}{2}(a+\rho_2)(R-\rho_2)\sin(-\alpha_2-\beta_2) - \frac{\alpha_1+\beta_1}{2}{\rho_1}^2 - \frac{\alpha_2+\beta_2}{2}{\rho_2}^2 + \frac{\alpha_1+\alpha_2}{2}a^2\right)4$$

$$A_{rho1} =$$

$$2\rho_1\int_{-\alpha_1}^{\beta_1}\sqrt{R^2 - (R-\rho_1)^2 - {\rho_1}^2 - 2\rho_1(R-\rho_1)\sin\beta_1\,sin\,\theta - 2\rho_1(R-\rho_1)\cos\beta_1\cos\theta}$$

$$A_{rho2} =$$

$$2\rho_2\int_{-\alpha_2}^{\beta_2}\sqrt{R^2 - (R-\rho_2)^2 - {\rho_2}^2 - 2\rho_2(R-\rho_2)\sin\beta_2\,sin\,\theta - 2\rho_2(R-\rho_2)\cos\beta_2\cos\theta}$$

Geometry II, III, IV of cells interacting with large fibers are the same as the cell interacting with small fibers.

4.7.6 Total energy calculation for a single cell adhered to two fibers

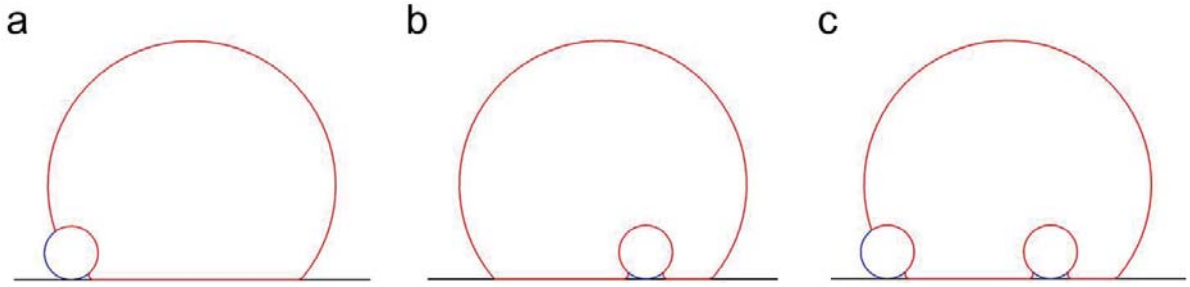

Figure S4. 8 Section views of an individual cell adherent to two single fibers at two positions (a, b) and to the combination of these two fibers (c).

Below, we prove that E_{tot} of the cell adherent to two fibers ($E_{tot}(ab)$) is related to E_{tot} of the cell adherent to each of the two fibers separately according to $E_{tot}(ab) = E_{tot}(a) + E_{tot}(b) - E_{tot}(flat)$:

$$E_{tot}(ab) = E_{ad}(ab) + E_{str}(ab)$$

$$A_{ad}(ab) = A_{ad}(ab) - A_{ad}(flat) + A_{ad}(flat)$$

$$= [A_{ad}(a) - A_{ad}(flat)] + [A_{ad}(b) - A_{ad}(flat)] + A_{ad}(flat)$$

$$= A_{ad}(a) + A_{ad}(b) - A_{ad}(flat)$$

$$E_{ad}(ab) = -w_{ad}A_{ad}(ab) = -w_{ad}[A_{ad}(a) + A_{ad}(a) - A_{ad}(flat)]$$

$$= E_{ad}(a) + E_{ad}(b) - E_{ad}(flat)$$

$$
\begin{aligned}
(\mathrm{A}(ab)-\mathrm{A}_0)^2 &= (\mathrm{A}(ab)-\mathrm{A}(flat)+\mathrm{A}(flat)-\mathrm{A}_0)^2 \\
&= [\big(\mathrm{A}(a)-\mathrm{A}(flat)\big)+\big(\mathrm{A}(b)-\mathrm{A}(flat)\big)+\mathrm{A}(flat)-\mathrm{A}_0]^2 \\
&= [(\mathrm{A}(a)-\mathrm{A}_0)+(\mathrm{A}(b)-\mathrm{A}_0)-(\mathrm{A}(flat)-\mathrm{A}_0)]^2 \\
&= [(\mathrm{A}(a)-\mathrm{A}_0)+(\mathrm{A}(b)-\mathrm{A}_0)-(\mathrm{A}(flat)-\mathrm{A}_0)][(\mathrm{A}(a)-\mathrm{A}_0)+(\mathrm{A}(b)-\mathrm{A}_0) \\
&\quad +(\mathrm{A}(flat)-\mathrm{A}_0)-2(\mathrm{A}(flat)-\mathrm{A}_0)] \\
&= [(\mathrm{A}(a)-\mathrm{A}_0)+(\mathrm{A}(b)-\mathrm{A}_0)-(\mathrm{A}(flat)-\mathrm{A}_0)][(\mathrm{A}(a)-\mathrm{A}_0)+(\mathrm{A}(b)-\mathrm{A}_0) \\
&\quad +(\mathrm{A}(flat)-\mathrm{A}_0)] \\
&\quad -2[(\mathrm{A}(a)-\mathrm{A}_0)+(\mathrm{A}(b)-\mathrm{A}_0)-(\mathrm{A}(flat)-\mathrm{A}_0)](\mathrm{A}(flat)-\mathrm{A}_0) \\
&= ((\mathrm{A}(a)-\mathrm{A}_0)+(\mathrm{A}(b)-\mathrm{A}_0))^2-(\mathrm{A}(flat)-\mathrm{A}_0)^2 \\
&\quad -2[(\mathrm{A}(a)-\mathrm{A}_0)+(\mathrm{A}(b)-\mathrm{A}_0)-(\mathrm{A}(flat)-\mathrm{A}_0)](\mathrm{A}(flat)-\mathrm{A}_0) \\
&= (\mathrm{A}(a)-\mathrm{A}_0)^2+(\mathrm{A}(b)-\mathrm{A}_0)^2-(\mathrm{A}(flat)-\mathrm{A}_0)^2 \\
&\quad +2(\mathrm{A}(a)-\mathrm{A}_0)(\mathrm{A}(b)-\mathrm{A}_0) \\
&\quad -2[(\mathrm{A}(a)-\mathrm{A}_0)+(\mathrm{A}(b)-\mathrm{A}_0)-(\mathrm{A}(flat)-\mathrm{A}_0)](\mathrm{A}(flat)-\mathrm{A}_0) \\
&= (\mathrm{A}(a)-\mathrm{A}_0)^2+(\mathrm{A}(b)-\mathrm{A}_0)^2-(\mathrm{A}(flat)-\mathrm{A}_0)^2 \\
&\quad +2(\mathrm{A}(a)-\mathrm{A}_0)(\mathrm{A}(b)-\mathrm{A}_0)-2[\mathrm{A}(a)+\mathrm{A}(b)-\mathrm{A}_0-\mathrm{A}(flat)](\mathrm{A}(flat)-\mathrm{A}_0) \\
&= (\mathrm{A}(a)-\mathrm{A}_0)^2+(\mathrm{A}(b)-\mathrm{A}_0)^2-(\mathrm{A}(flat)-\mathrm{A}_0)^2 \\
&\quad +2(\mathrm{A}(a)-\mathrm{A}_0)(\mathrm{A}(b)-\mathrm{A}_0) \\
&\quad -2\big[(\mathrm{A}(a)-\mathrm{A}_0)+\big(\mathrm{A}(b)-\mathrm{A}(flat)\big)\big](\mathrm{A}(flat)-\mathrm{A}_0) \\
&= (\mathrm{A}(a)-\mathrm{A}_0)^2+(\mathrm{A}(b)-\mathrm{A}_0)^2-(\mathrm{A}(flat)-\mathrm{A}_0)^2 \\
&\quad +2(\mathrm{A}(a)-\mathrm{A}_0)(\mathrm{A}(b)-\mathrm{A}_0)-2(\mathrm{A}(a)-\mathrm{A}_0)(\mathrm{A}(flat)-\mathrm{A}_0) \\
&\quad -2\big(\mathrm{A}(b)-\mathrm{A}(flat)\big)(\mathrm{A}(flat)-\mathrm{A}_0) \\
&= (\mathrm{A}(a)-\mathrm{A}_0)^2+(\mathrm{A}(b)-\mathrm{A}_0)^2-(\mathrm{A}(flat)-\mathrm{A}_0)^2 \\
&\quad +2(\mathrm{A}(a)-\mathrm{A}_0)\big(\mathrm{A}(b)-\mathrm{A}(flat)\big)-2\big(\mathrm{A}(b)-\mathrm{A}(flat)\big)(\mathrm{A}(flat)-\mathrm{A}_0)
\end{aligned}
$$

$$= (\mathrm{A}(a) - \mathrm{A}_0)^2 + (\mathrm{A}(b) - \mathrm{A}_0)^2 - (\mathrm{A}(flat) - \mathrm{A}_0)^2$$

$$+ 2\big(\mathrm{A}(a) - \mathrm{A}(flat)\big)\big(\mathrm{A}(b) - \mathrm{A}(flat)\big)$$

Since $\mathrm{A}(a) - \mathrm{A}(flat)$ and $\mathrm{A}(b) - \mathrm{A}(flat)$ are much smaller than $\mathrm{A}(a) - \mathrm{A}_0$, $\mathrm{A}(b) - \mathrm{A}_0$, and $\mathrm{A}(flat) - \mathrm{A}_0$, then

$$(\mathrm{A}(ab) - \mathrm{A}_0)^2 \approx (\mathrm{A}(a) - \mathrm{A}_0)^2 + (\mathrm{A}(b) - \mathrm{A}_0)^2 - (\mathrm{A}(flat) - \mathrm{A}_0)^2$$

$$\mathrm{E}_{\mathrm{str}}(ab) = \frac{1}{2}\mathrm{k}_{\mathrm{cell}}\frac{(\mathrm{A}(ab) - \mathrm{A}_0)^2}{\mathrm{A}_0} \approx \frac{1}{2}\mathrm{k}_{\mathrm{cell}}\frac{(\mathrm{A}(a) - \mathrm{A}_0)^2 + (\mathrm{A}(b) - \mathrm{A}_0)^2 - (\mathrm{A}(flat) - \mathrm{A}_0)^2}{\mathrm{A}_0}$$

$$= \mathrm{E}_{\mathrm{str}}(a) + \mathrm{E}_{\mathrm{str}}(b) - \mathrm{E}_{\mathrm{str}}(flat)$$

$$\mathrm{E}_{\mathrm{tot}}(ab) = \mathrm{E}_{\mathrm{tot}}(a) + \mathrm{E}_{\mathrm{tot}}(b) - \mathrm{E}_{\mathrm{tot}}(flat)$$

4.7.7 Population scale total energy calculation for cells adhered to nanofiber textured surfaces with uniform fiber diameter and spacing

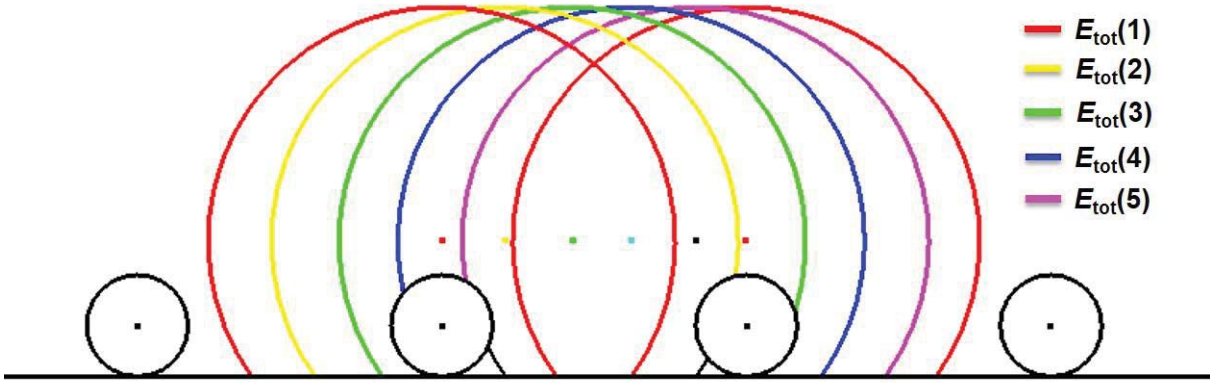

Figure S4. 9 Cell at different positions with $E_{tot}(1)$, $E_{tot}(2)$, $E_{tot}(3)$, $E_{tot}(4)$, and $E_{tot}(5)$.

The probability of a cell remaining adhered to a substrate is dependent upon $\mathrm{E}_{\mathrm{tot}}$ where the cell initially contacts the surface. For cells adhering to a nanofiber-coated surface with fiber diameter of $\mathrm{D}_{\mathrm{fiber}}$ and fiber edge-to-edge spacing of S, the spatially-averaged $\mathrm{E}_{\mathrm{tot}}$ of the cell initially

deposited on the surface is represented by $\overline{\mathrm{E_{tot}}}$. Since the probability of the cell deposition at all positions is equal, $\overline{\mathrm{E_{tot}}}$ can be calculated as:

$$\overline{\mathrm{E_{tot}}} = \frac{1}{N}\sum_{i}^{N} \mathrm{E_{tot}}(i)$$

Where $\mathrm{E_{tot}}(i)$ is $\mathrm{E_{tot}}$ of a cell adherent to two fibers at a position with the distance of the cell center and one fiber centerline of $\Delta \mathrm{x}(i)$, where $0 \leq \Delta \mathrm{x}(i) \leq S + D_{\mathrm{fiber}}$.

Chapter 5: *Candida albicans* Yeast Seek to Adhere in Energetically Optimal Locations

5.1 Abstract

The interaction of microbes with surface topographical features at the nanoscale is critical to the biofilm formation and other biological activities. Bacteria near-surface motility has been found to significantly affect the cell attachment on surfaces. The eukaryotic microorganism, yeast, is commonly known to be non-motile. Therefore, the role of near-surface yeast cell motion on its initial attachment remains largely unexplored. Herein, we report that *Candida albicans* yeast displays directional motion around nanofiber topographies with fiber diameters larger than 1 μm. Through development of a biophysical model, we show that the cells eventually adhere in the energetically optimal locations. The total energy is comprised of the adhesion energy (due to the interface formation between the cell and the surface) and the stretching energy (energy cost by the stretching of the cell membrane). The energy gradient as a function of location with respect to the surface feature must be large enough to drive the motion, so we did not observe the adjustment of the adhesion location on flat surfaces or around small diameter fibers (0.5 μm). This phenomenon is unique to live cells, indicating that it is a biologically driven behavior.

5.2 Introduction

Microbial biofilm formation is a costly problem in the marine industry[92], the food processing industry[93], and for medical devices[94]. The formation of biofilms starts with the adhesion of

This chapter in its entirety will be submitted as a manuscript to a peer-reviewed journal. The co-authors are Zhou Ye, Amrinder S. Nain and Bahareh Behkam.

microorganisms on substrates. Understanding the interaction of single microbes with substrate topographical features is critical to a better understanding of the biofilm formation and other biological activities of adherent cells. Previous work by us and others has demonstrated that bacteria can recognize nanostructures and modulate their behaviors accordingly. The micro/nano topography has an effect on the cell attachment density and organization[10,90]. The reported selectivity in attachment location which leads to distinct spatial distribution patterns on nanostructures is suggested to be related to the near-surface motility in bacteria that are driven by flagella and type IV pili, including near-surface swimming, crawling, walking, and gliding motilities (i.e. adventurous gliding or A-motility, and social gliding or S-motility)[132,133]. Bacterial flagella are also found to be instrumental in adhesion to microscale crevices where the bacterial body can hardly reach[134]. In contrast, the eukaryotic microorganisms, yeasts, are presently thought to lack motility appendages and are well-accepted to be non-motile both in planktonic form and on the surface[135]. The interaction between a yeast cell and the surface nanotopography at high spatiotemporal resolution can provide insights into the mechanisms involved in the cell interactions with the surface topographical features.

In this study, we investigated the near-surface behavior and the early-stage adhesion of the fungal pathogen *Candida albicans* to nanofiber-textured surfaces. We report that upon adhering to a surface, *C. albicans* continually adjust their position and stably attach in a location of minimum total energy (Figure 5.1). We developed a biophysical model of cell adhesion to nanofiber textured surfaces to explain the selective adhesion position of *C. albicans* yeast. Notably, we find this behavior to be unique to living yeast cells.

5.3 Materials and methods

5.3.1 Yeast culture

Wild-type *C. albicans* strain SC5314 (ATCC MYA2876, American Type Culture Center, Manassas, VA) was streaked on a sabouraud dextrose agar (SDA) plate and incubated at 25 °C for 48 h. Several (3-5) colonies were inoculated into 10 ml of yeast peptone dextrose (YPD) medium and grown at 25 °C and 150 rpm for 24 h. All cells grew as yeast in this culturing condition. In order to limit the proliferation of the cells during the experiment, 100 µl of yeast culture was diluted into 5 ml of 1× phosphate-buffered saline (PBS) and was sonicated and vortexed at 1000 rpm for 30 s each three times before experiments to separate clumped planktonic cells.

5.3.2 Substrate preparation

The non-electrospinning Spinneret-based Tunable Engineered Parameters (STEP) technique[23] was used to deposit PS nanofibers of 0.5 µm, 1 µm, and 2 µm diameters from 14 wt%, 18 wt% and 25 wt% of 2,000K g mol^{-1} molecular weight PS solutions (in xylene solvent) on a PS sheet (5×10 mm, 125 µm thick). Each nanofiber-textured sample was placed in one well of a 12-well plate containing 4 ml of YPD to condition the substrate surface overnight. The substrate was then rinsed in 4 ml of 1× PBS three times before experiments. Finally, each well was inoculated with 100 µl of the diluted *C. albicans* culture at OD_{600}=0.3 and 4 ml of 1× PBS.

5.3.3 UV treatment of yeast

A 400 µl of the diluted *C. albicans* culture (OD_{600}=0.3) was deposited into one well of a 12-well plate and exposed to UV light for 10 min (650 µW/cm^2 at 254 nm wavelength). The killing efficiency of the UV treatment was tested by streaking an SDA agar plate with UV-treated cells and incubating it at 25 °C for 48 h which did not yield any growth. To explore the cell membrane

integrity, 1 μL of propidium iodide (20 mM in DMSO) was added to 1 ml of UV-treated *C. albicans* solution. The sample was incubated at 37 °C and in the dark for 30 min before fluorescent microscopy. In order to compare the cell wall property, zeta potentials of the live and UV-treated cells were measured according to previously described methods[136]. Briefly, the live and UV-treated cells were separately centrifuged at 1,700 g and resuspended in 0.1× PBS. Zeta potential of the cells was measured by dynamic light scattering with a Zetasizer NanoZS equipped with a He-Ne laser (Malvern Instruments, Software version 7.11) at 25 °C and 15V.

5.3.4 Measurement of cell position

After introducing the yeast solution into the well plates, the sample was observed by a phase-contrast microscope (Zeiss Observer.Z1) with a 40×/0.6 objective (LD Plan-NEOFL). The lower frame rate videos (0.1 fps) were taken by a AxioCam MRmCCD camera (Zeiss), and the higher frame rate videos (60 fps) were taken by a AxioCam HSm CCD camera (Zeiss). The images were processed by Zen, ImageJ, and Matlab. The position of the cell center was constructed from the outlines of the cell. Considering the possible vibrations from the microscope and the building, the position of the cell center was subtracted by the fiber center, since the fiber was deposited on the substrate and cannot move by the environment. The Fourier transform was analyzed by MATLAB.

5.3.5 Biophysical modeling for cell adhesion

The theoretical model for changes in the total energy of the cell adhered to nanofiber-textured surfaces was described in detail in our earlier work (Chapter 4). Briefly, E_{ad} was defined as the integral of work of adhesion (w_{ad}) over the cell-substrate contact surface area (A_{ad}):

$$E_{\mathrm{ad}} = -\oint w_{\mathrm{ad}} dA_{\mathrm{ad}} \quad (1)$$

Assuming a homogenous cell wall, Eq. (1) is simplified to:

$$E_{\mathrm{ad}} = -w_{\mathrm{ad}} A_{\mathrm{ad}} \quad (2)$$

The cell will expend energy to deform the cell wall in order to increase the adhesion surface area, which is denoted as E_{str}. E_{str} can be calculated from the following equation[124]:

$$E_{\mathrm{str}} = \frac{1}{2} k_{\mathrm{strl}} \frac{(A-A_0)^2}{A_0} \quad (3)$$

Where k_{cell} is the stretching modulus, A is the total surface area of the stretched cell after adhesion, and A_0 is the original cell surface area in a non-adherent state which can be approximated as a sphere with a diameter of D_0.

The total energy can be simplified as:

$$E_{\mathrm{tot}} = E_{\mathrm{ad}} + E_{\mathrm{str}} = -w_{\mathrm{ad}} A_{\mathrm{ad}} + \frac{1}{2} k_{\mathrm{str}} \frac{(A-A_0)^2}{A_0} \quad (4)$$

The unknown parameters in Eq. (4) are A_{ad} and A. We hypothesize that the overall shape of the cell maintains as spherical and that the volume of the cell maintains constant. With these shape and volume constraints, we calculate E_{tot} from every combination of these geometric parameters (Figure S5.6) in a physically meaningful range (e.g. $0<\alpha<\pi$, $0<\beta<\pi$, $\rho>0$). The geometry of the cell that results the minimum E_{tot} when adhered to the substrate at a specific position was computed using an optimization routine.

5.4 Results and discussion

5.4.1 *C. albicans* yeast interacting with a single nanofiber

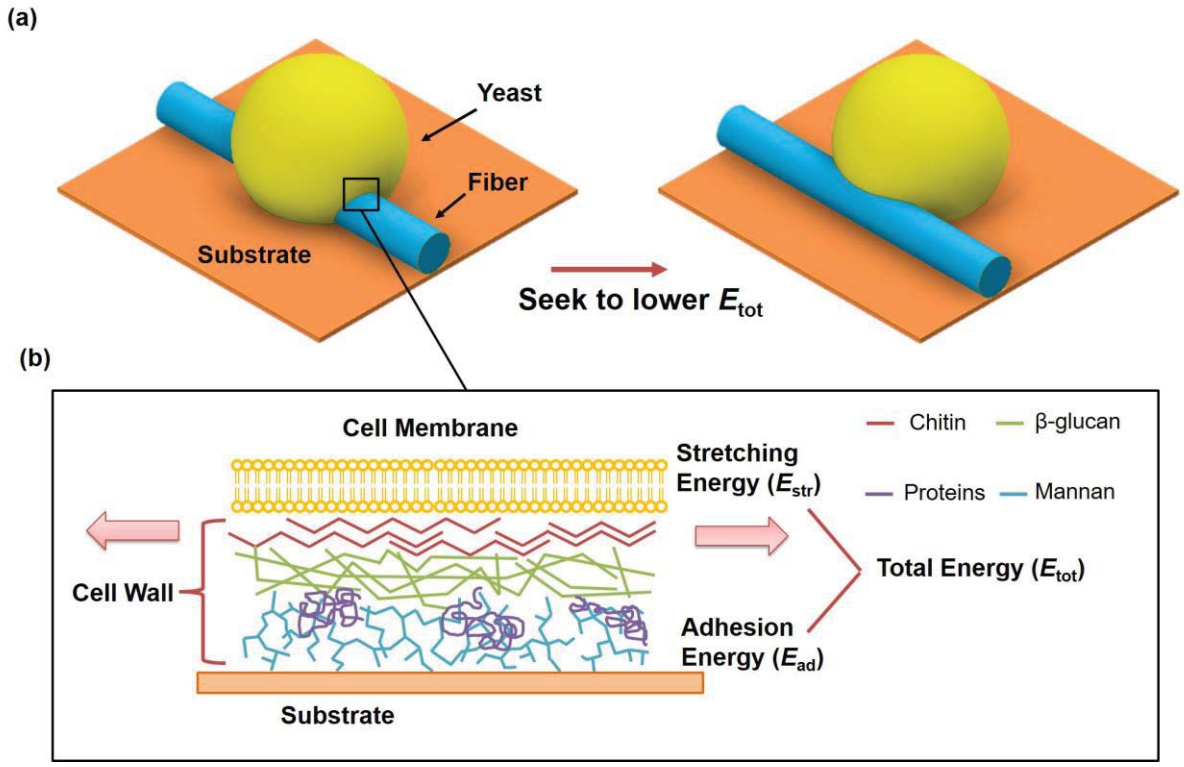

Figure 5. 1 Schematic of *C. albicans* yeast adjusting its attachment location to lower its total energy and (b) Adhesion energy, associated with the formation of an interface between the cell and the substrate, and stretching energy due to deformation in cell membrane dictate the changes experienced in the cell total energy.

We first investigated the effect of fiber diameter (i.e. topographical feature size) on the interaction of *C. albicans* yeasts with polystyrene (PS) surfaces coated with highly aligned PS nanofibers (Figure S5.1). Nanofibers of precisely defined diameter with edge-to-edge spacing of 15 μm were deposited on PS substrates using the Spinneret-based Tunable Engineered Parameters (STEP) technique[23]. The average cell diameter was measured to be 4.2±0.5 μm (N=105). The distance between the cell center and the fiber center (Δx) was used to describe the location of the cell relative to the fiber (Figure 5.2a). We normalized Δx by D_{cell} to exclude the effect of the varying cell diameter. For the same fiber diameter, $\Delta x/D_{cell}$ associated with the minimum E_{tot} is not

sensitive to the cell diameter (Figure S5.2). When the cell initially attached on the substrate, the percentage of adhesion occurrence at different locations was equal for all fiber diameters (i.e. D_{cell} =0.5, 1.0, and 2.0 μm) (Figure 5.2b). We define the equilibrium adhesion location as the adhesion location maintained for at least 30 min. The adhesion location maintained for 30 min was almost always permanently maintained for the entire duration of experiment. We found that for D_{fiber}=1.0 μm, more than 60% of the cells achieved equilibrium adhesion in the region of $\Delta x/D_{cell}$ = 0.3-0.5; for D_{fiber}=2.0 μm, more than 70% of the cells equilibrated in the region of $\Delta x/D_{cell}$ = 0-0.1 or $\Delta x/D_{cell}$ = 0.3-0.4 (Figure 5.2b). However, for D_{fiber} = 0.5 μm, the position adjustment from initial adhesion to equilibrium was not obvious.

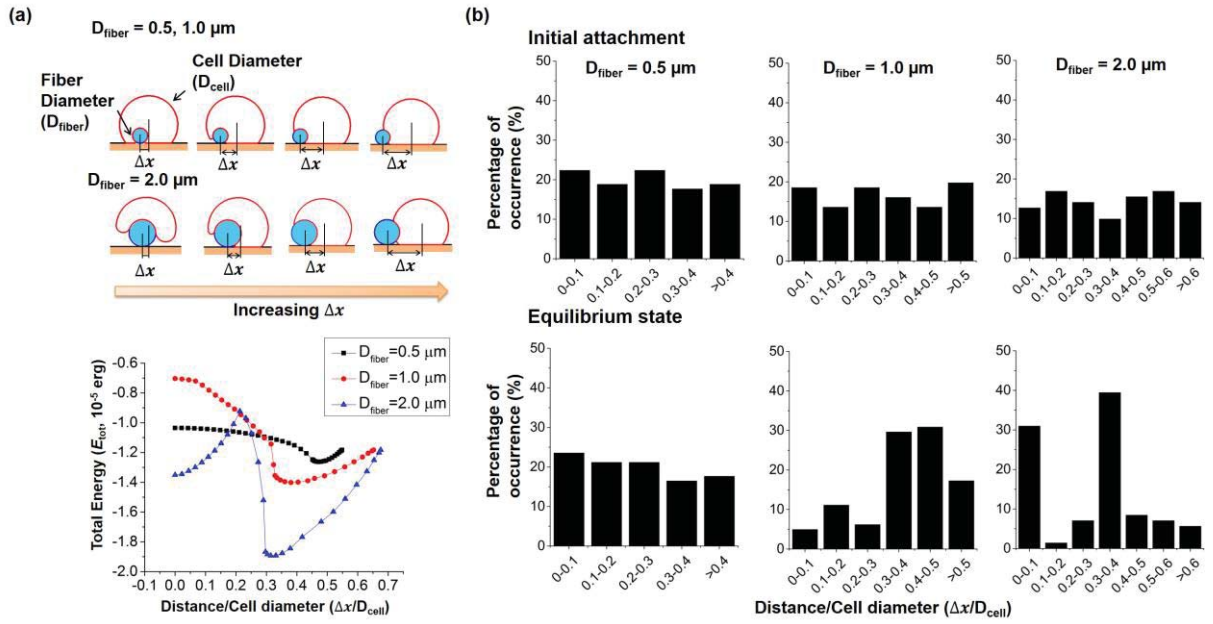

Figure 5. 2 (a) Cross-section views of a *C. albicans* yeast cell interacting with a single fiber of diameter of 0.5 μm, 1.0 μm and 2.0 μm at different cell-fiber center distances (Δx) and corresponding total energy vs. distance/cell diameter ($\Delta x/D_{cell}$) (b) Percentage of occurrence of *C. albicans* adhesion to a single fiber of diameter of 0.5 μm, 1.0 μm and 2.0 μm at different distance/cell diameter ($\Delta x/D_{cell}$), N=85, 81 and 71, respectively.

We hypothesize that the adherent cell's equilibrium position is the location of total energy minima which is energetically most favorable and that if the total energy is not significantly different in

different positions, then there is no preferred (or optimum) attachment location. We next developed a biophysical model for yeast cell-nanofiber-textured substrate interaction to test our hypothesis. Upon adhesion to a substrate surface, the total energy of a cell (E_{tot}) will change as a result of the formation of a cell-substrate interface (described by the adhesion energy (E_{ad})) and the ensuing stretching (described by the stretching energy (E_{str})), and bending or change in curvature (described by the bending energy (E_{c})) of the cell membrane (Figure 5.1)[119,120]. Bending energy (E_{c}) is not considered in this study, since E_{c} is negligible compared to E_{ad}. As shown in Figure 5.2a, when the cell adheres to 0.5 μm or 1 μm diameter fiber, for all relevant values of $\Delta x/D_{cell}$, the cell is in contact with both the fiber and the underlying flat substrate. As a result, there is only one total energy minimum point. However, in the case of 2 μm diameter fiber, at small normalized separation distance values (i.e. $\Delta x/D_{cell} \leq 0.1$, when the cell center is close to the fiber center), the cell is only in contact with the fiber and at higher $\Delta x/D_{cell}$ cell is in contact with both the fiber and the substrate. As a result, when the cell adheres to 2 μm diameter fiber, there are two total energy minima. Correspondingly, for D_{fiber}=1.0 μm, E_{tot} is smaller than 95% of the minimum E_{tot} in the region of $\Delta x/D_{cell}$ = 0.32-0.51; for D_{fiber}=2.0 μm, E_{tot} is smaller than 95% of the minimum E_{tot} in the region of $\Delta x/D_{cell}$ = 0-0.09 and 0.30-0.42 (Figure 5.2a). A comparison between the modeled total energy trends and experimentally obtained equilibrium adhesion locations, indicates that cells predominantly adhered stably in locations where the total energy was the lowest. For D_{fiber}=0.5 μm, the difference between maximum E_{tot} and minimum E_{tot} is smaller than 18%, which is not significant enough to affect the adhesion location.

In order to investigate the process of adhesion location adjustment over time, we conducted time-lapse microscopy of the initial to equilibrium cell-surface interactions at high spatiotemporal resolutions (Figure 5.3). We first tracked the position of cells exclusively interacting with the flat

substrate with a minimum 5 µm separation distance between the cell starting position and the nearest fiber to avoid contact/interactions between the cell and the fiber. Changes in position were measured relative to the nearest fiber, as shown in the Figure 5.3a-i.. Most cells demonstrated very small displacement ($(\Delta x- \Delta x(t=0))/D_{cell} < 0.1$) over more than one hour. The cells attached to the 0.5 µm diameter fibers also mostly vibrated around the initial attachment location. A few cells showed larger displacement ($0.1<\Delta x/D_{cell} < 0.2$) after the initial attachment, but did not display any directional motion. When interacting with larger fibers (D_{fiber}=1.0 µm or 2.0 µm), most cells moved to the optimal adhesion locations with minimum total energy ($\Delta x/D_{cell}$ = 0.3-0.5 for D_{fiber}=1.0 µm, $\Delta x/D_{cell}$ = 0-0.1 and 0.3-0.4 for D_{fiber}=2.0 µm), even when the initial attachment position was far from the optimal locations. After reaching the optimal adhesion locations, the cells maintained their equilibrium state for the duration of the experiment. The average time taken to reach the equilibrium adhesion location was 42 min for 1.0 µm fiber (N=10) and 16 min for 2.0

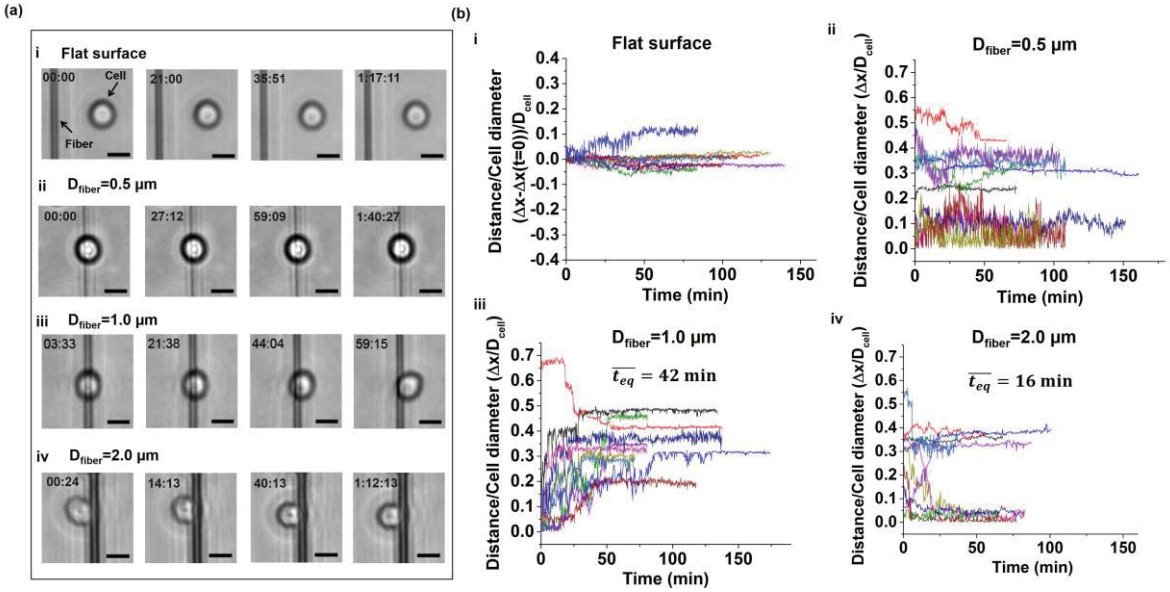

Figure 5. 3 (a) Time-lapse phase contrast microscopy images of a *C. albicans* yeast cell interacting with flat surface, and a 0.5 µm, 1.0 µm or 2.0 µm diameter fiber. Time scales are h:min:sec. Scale bars are 5 µm. (b) Track of the cell position ($\Delta x/D_{cell}$) vs. time. N=10 for each topographical feature.

μm fiber (N=7). We attribute the shorter "seeking period" duration on the 2.0 μm fibers to the significantly steeper spatial energy gradient, as shown in Figure 5.2a.

5.4.2 *C. albicans* yeast interacting with two nanofibers

We next investigated the effect of the fiber spacing on cell adhesion process by studying *C. albicans* yeast on a nanofiber-textured surfaces wherein the edge-to-edge spacing (S) of the parallel nanofibers is smaller than the *C. albicans* yeast diameter, and the cell can interact with more than one fiber. The fiber diameter was kept constant (D_{fiber} = 1.0 μm) and the fiber spacing was varied (S=1.0-4.0 μm). Our theoretical analyses suggest E_{tot} to be dependent on D_{fiber} and S, as well as the relative position of the cell with respect to the two fibers, which was represented by the distance (δ) between the cell center and the fiber spacing center (Figure 5.4a). When S = 1.0 μm, E_{tot} increased with a decrease in δ; however, for S= 2.0-4.0 μm, E_{tot} increased when δ increased. The different optimal attachment location for small and large spacing is because the cell wall needs a higher deformation when the fiber spacing is small. We next normalized S and δ to the cell diameter (D_{cell}) to exclude the effect of different cell sizes, as shown in the Figure 5.4b. For each S/D_{cell}, there is the corresponding theoretical value of δ/D_{cell} associated with the minimum E_{tot}. The corresponding δ/D_{cell} decreases with an increase in S/D_{cell} for $S/D_{cell} \leq 0.6$ (Figure 5.4b). For $S/D_{cell} \geq 0.6$, the corresponding δ/D_{cell} is equal to zero, which means that the optimal adhesion location is the middle of the two fibers. Then, we carried out experiments in which *C. albicans* yeast was introduced on PS nanofiber-textured PS substrate with 1.0 μm fiber diameter and varying fiber spacing. Similar to the single fiber experiments, when the cell adhesion location was maintained for at least 0.5 h, we determined the cell to be at the equilibrium adhesion location and

measured δ. Our experimental results are in close agreement with our theoretical predictions, showing that when the cell interacts with two fibers, the equilibrium adhesion location is associated with the minimum E_{tot} which is dependent on the two fiber spacing (Figure 5.4b). As was the case for interaction with single fibers, the equilibrium adhesion locations were reached through continual adjustment of the cell adherent position to a lower E_{tot} region, which was also observed by the microscopy videos (Figure 5.4c). For S=1.0 μm, the cell moved from the middle of the two fibers to one side; for S=3.0 μm, the cell moved from the side to the middle. After reaching the minimum energy regions, the cell did not move further or back. If the yeast cell has an oval morphology, instead of its typically spherical shape, the cell achieves energetically optimal adherent positions through either linear translation or rotation. The orientation of the cell relative to the fiber is also adjusted in response to the nanofibers until an orientation of minimum E_{tot} is achieved. As shown in Figure S5.4, an oval-shaped *C. albicans* yeast with its major axis along the nanofibers upon attachment (θ = 0°), gradually rotates until its major axis is perpendicular to the nanofibers (θ = 90°). From the track of the cell-fiber angle, the cell retained its 90°orientation with respect to the fibers for the remainder of the experiment duration (over 1 h), indicating that the cell was in an equilibrium state.

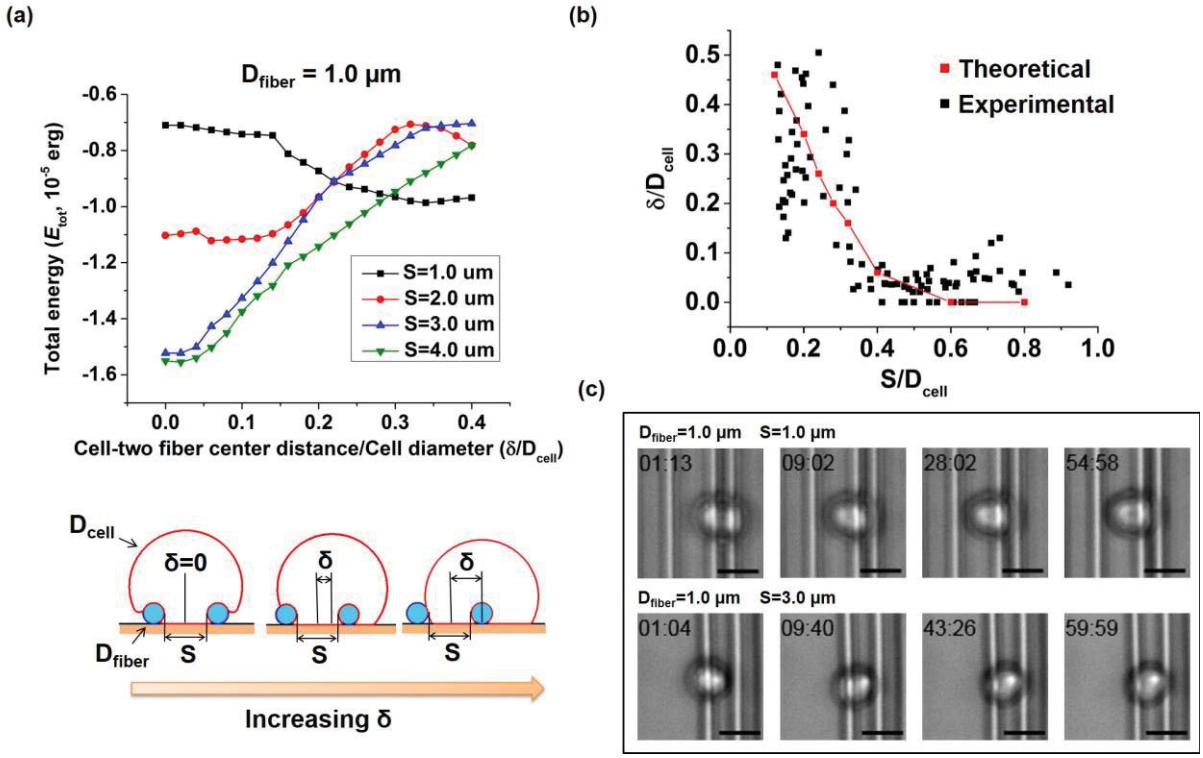

Figure 5. 4 (a) Total energy of *C. albicans* yeast interacting with two fibers of diameter of 1.0 μm and spacing of 1.0 μm, 2.0 μm, 3.0 μm and 4.0 μm vs. the cell center and the two-fiber center distance (δ), (b) Comparison of the theoretically predicted optimal δ/D_{cell} (red) and experimentally obtained equilibrium δ/D_{cell} (black, N=98) as a function of S/D_{cell}, (c) Time-lapse phase contrast microscopy images of a cell interacting with two fibers of diameter of 1.0 μm and spacing of 1.0 μm or 3.0 μm. Time scales are min:sec. Scale bars are 5 μm.

5.4.3 UV treated *C. albicans* yeast as a control

To investigate whether the preferred attachment of *C. albicans* yeast in locations of minimum energy is a biologically driven process, we treated the yeast cells with UV light to induce cell death (see methods) and then introduced the dead cells onto the nanofiber-textured substrates. In contrast to the live cells, we observed the UV-treated cells to distribute fairly uniformly in every adherent position in the equilibrium adherent state (Figure 5.5a). Most of the cells maintained their original adherent position after initial attachment, contrary to live cells (Figures 5.3 and 5.4c, and S5.4-S5.6 (live cells), and Figure 5b-c (dead cells)). We used propidium iodide (PI) stain to confirm the

integrity of the cell membrane, as PI can only penetrate into damaged cell membrane. As shown in Figure S5.5, almost all of the UV-treated cells were not stained by PI, which indicated that the cell membrane was intact after UV treatment (cell death was confirmed by lack of growth of UV-treated cell cultures). Furthermore, we compared the cell wall property of the UV-treated cell and live cell by zeta potential measurement. Zeta potential of the live cell was measured to be -11.6±1.1 mV (N=10), and zeta potential of the UV-treated cell was measured to be -10.8±1.1 mV (N=10), indicating that the cell wall property was not significantly altered after UV-treatment. Thus, we conclude that the UV-treatment does not cause substantial change in the cell membrane and cell wall integrity, and therefore the difference in live and dead cell equilibrium adherent position distribution was due to the cessation of biological function. This suggests that the living cells actively seek to adhere in positions of minimal total energy.

To further investigate the mechanism of this process, we used high frame rate (60 fps) microcopy videos to study the vibrational behavior of the live and UV-treated cell during the adhesion process (Figure 5.6). Both the live and the UV-treated cells showed 0.1-0.3 μm vibration amplitude without significant difference (N=10 for live cells and UV-treated cells). The Fast Fourier Transform (FFT) analysis of the vibration data indicated that both the live and UV-treated cells have large amplitude (>10 nm) of motion at low frequency (< 5 Hz). However, no obvious peak was observed in higher frequency range (> 5 Hz). This vibrational behavior is similar to other adhered microorganisms (i.e. bacteria) and is caused by Brownian motion[137]. This indicates that the sliding and rotating of the live cell is not due to an active bio-actuation or the bio-actuation cannot be detected by optical microscope. For instance, high frequency (0.8 to 1.6 kHz) and low amplitude (3 nm) nanomechanical motion in *Saccharomyces cerevisiae* cell wall has been previously measured using atomic force microscopy (AFM), while such motion was not detectable in metabolically

inhibited yeasts[138]. .The biological underpinnings of the observed behavior will be investigated in a future study.

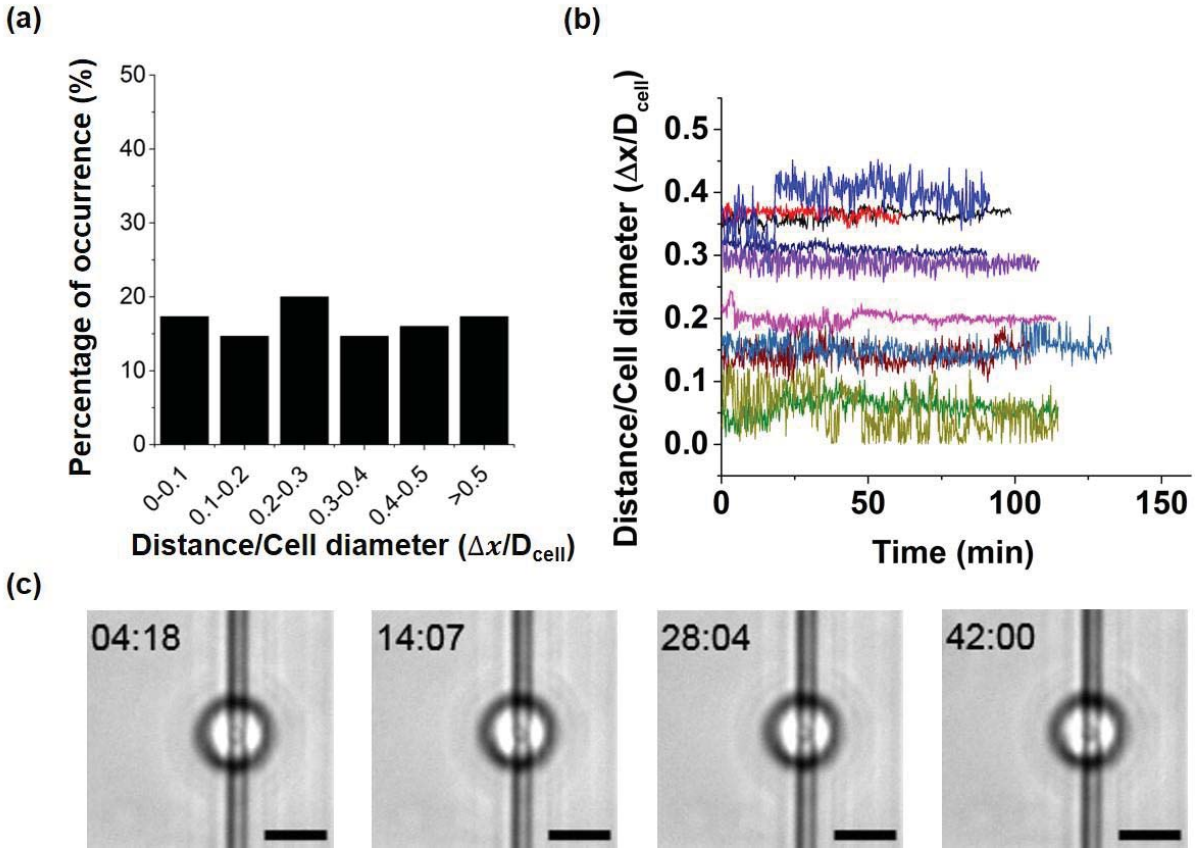

Figure 5. 5 (a) Percentage of occurrence of UV-treated *C. albicans* adhered to a single fiber of diameter of 1.0 µm at different distance/cell diameter ($\Delta x/D_{cell}$), N=75, (b) Track of the UV-treated *C. albicans* yeast cell position relative to a single fiber ($\Delta x/D_{cell}$) vs. time, N=10, (c) Representative time-lapse phase contrast microscopy images. Time scales are min:sec. Scale bars are 5 µm.

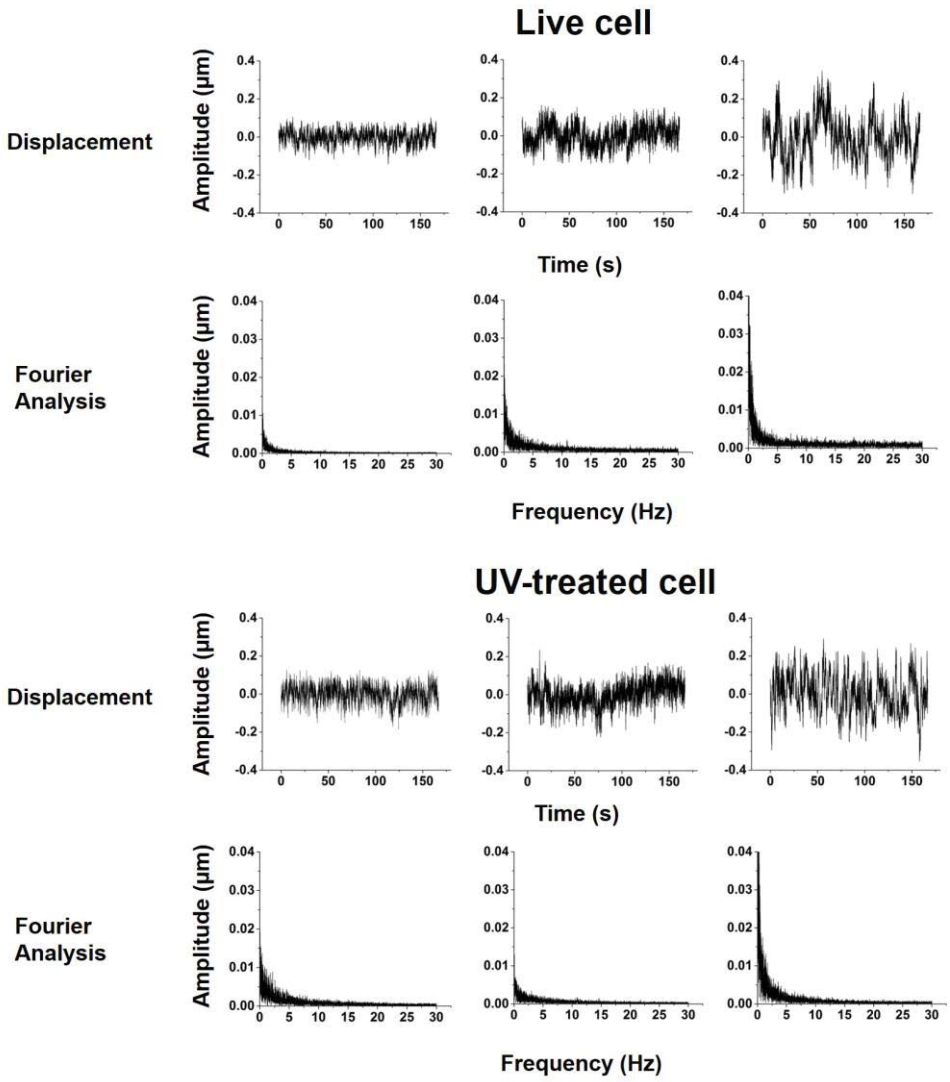

Figure 5. 6 Representative time series of vibrational displacement and corresponding Fourier transforms of three different live and UV-treated cells at the equilibrium adherent positions.

5.5 Conclusion

We investigated *C. albicans* yeast interactions with a nanofiber-textured surface from the initial to the equilibrium state at high spatiotemporal resolution. We report a non-Brownian biologically-driven motion that enables the cells to seek to adhere in distinctly preferred locations. Through biophysical modeling of yeast cell-nanofiber textured surface interactions, we demonstrate that

these preferred adhesion locations minimize the total energy of the adherent cells. The cell total energy was quantified as a function of the fiber diameter and spacing, and the relative position between the cell and the fibers. We have observed the sliding and rotating of *C. albicans* yeast after initial adhesion to the substrate. The duration of this motion from the initial attachment location to the equilibrium adhesion location is shorter for a high spatial energy gradient. This adherent position adjustment behavior was only observed in live cells, whereas the UV-treated cells stayed in the initial adhesion position upon attachment to the substrate. This directional movement may be facilitated by the nanomechanical motion of the cell wall. Our findings highlights the challenge associated with the antibiofilm surface nanopattern design, since the microbe can adjust the adhesion site from an energetically unfavorable state to an energetically more favorable state, which could increase the retention density. In order to design more efficient antibiofilm surfaces, the number of the sites that can lower the cell total energy should be minimized. Our work also suggests an interaction between the microorganism and the topographic microenvironment, which is important in the application of biosensors and biomedical devices.

5.6 Supplementary information

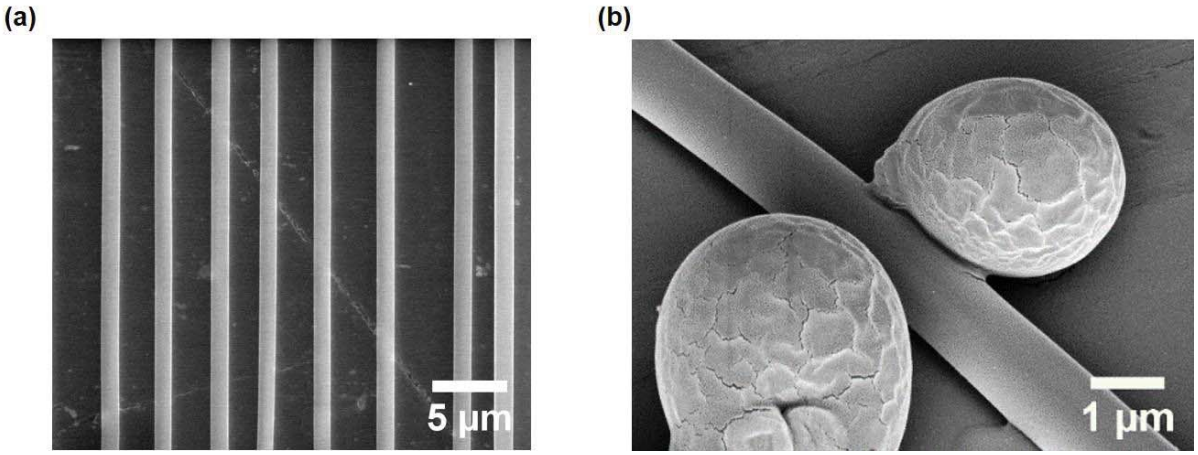

Figure S5. 1 (a) Scanning electron microscope (SEM) image of highly aligned 1 µm nanofibers (b) SEM of *C. albicans* yeast on 1 µm fiber in equilibrium adhesion state.

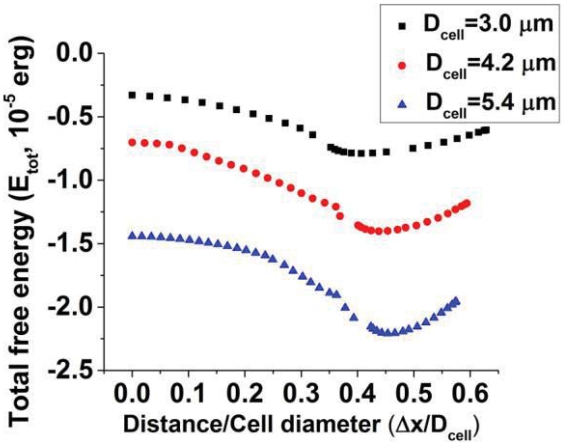

Figure S5. 2 Total free energy vs. $\Delta x/D_{cell}$ with cell diameters of 3.0 µm, 4.2 µm, and 5.4 µm on 1 µm fiber.

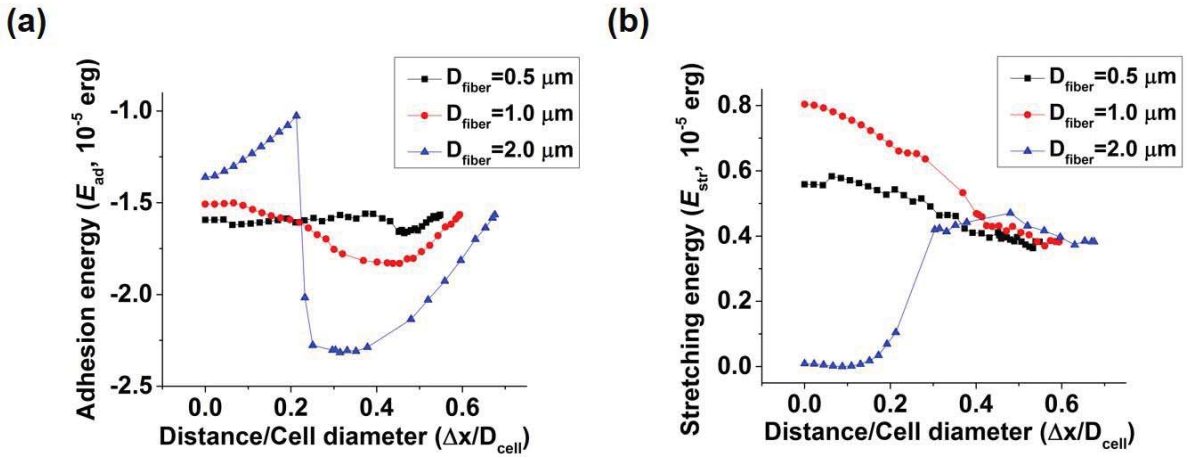

Figure S5. 3 Adhesion energy (a) and stretching energy (b) vs. $\Delta x/D_{cell}$ with fiber diameters of 0.5, 1.0 μm and 2.0 μm.

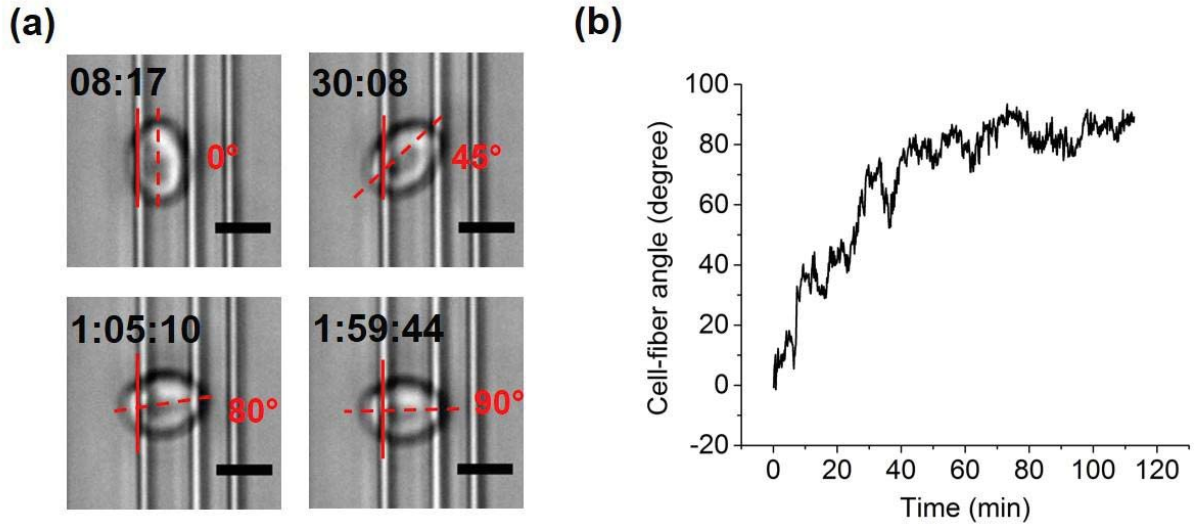

Figure S5. 4 (a) Time-lapse phase contrast microscopy images of an oval shaped *C. albicans* yeast cell interacting with two fibers, (b) Cell-fiber angle vs. time. Time scales are h:min:sec. Scale bars are 5 μm.

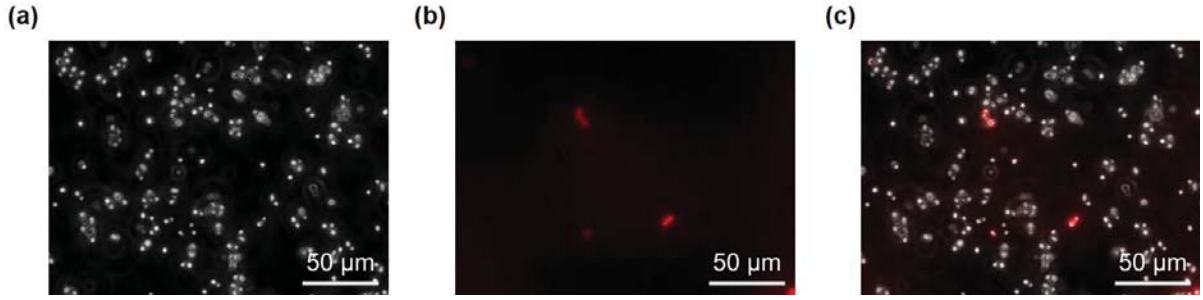

Figure S5. 5 Bright field (a), fluorescent (b) and merged (c) microscopy images of UV-treated cells with PI staining.

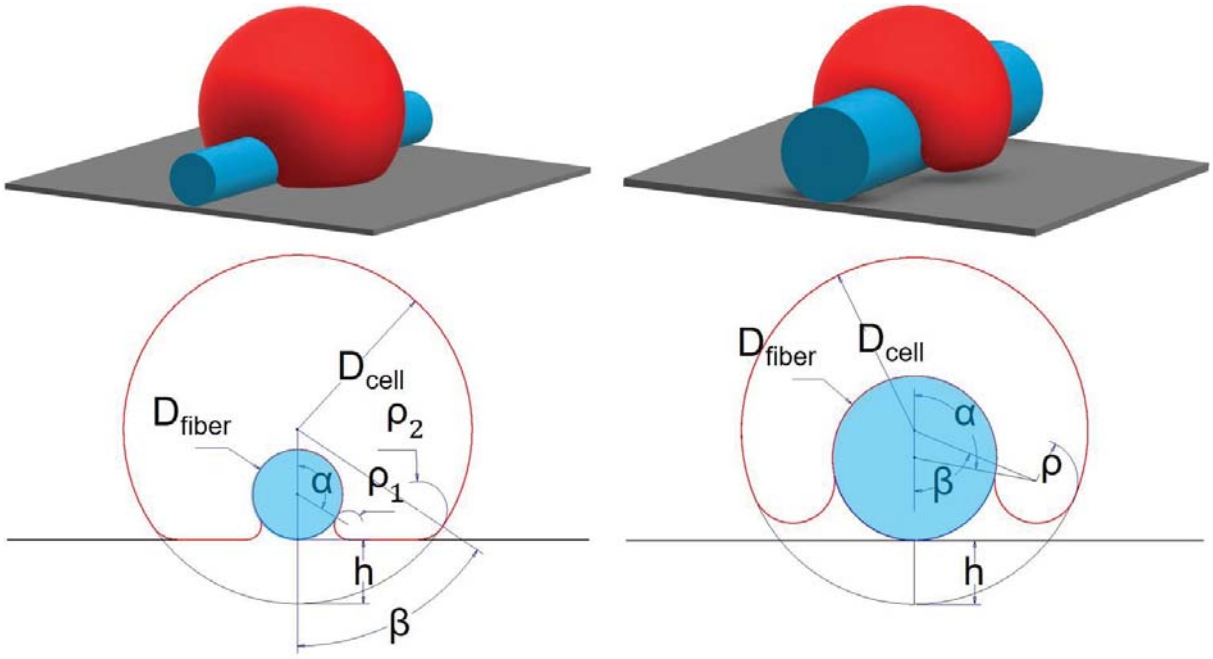

Figure S5. 6 3D and section view of a *C. albicans* yeast cell interacting with a single fiber.

Chapter 6: Conclusions and Future Directions

6.1 Concluding remarks

This research has focused on improving the understanding of the role of nanostructure characteristics on microbial adhesion and biofilm formation. The main accomplishments of this work are: **(1)** the development and characterization of the spun-wrapped aligned nanofiber (SWAN) lithography to fabricate micro/nano scale features on 3D objects. **(2)** the evaluation of the effect of the electrode surface feature size on the current production of microbial fuel cells. **(3)** he development and validation of a biophysical model of the total energy of *Candida albicans* yeasts on nanofiber-textured surfaces to predict the cell attachment density. **(4)** the evaluation of a single *Candida albicans* yeast cell motion on nanofiber-textured surfaces with the developed biophysical model. A brief summary of the work associated with each of these areas is outlined below:

- **Develop a versatile and scalable method for fabrication of nanostructures on 3D objects**

Spun-Wrapped Aligned Nanofiber lithography (SWAN lithography) was developed and shown to be able to nanopattern bulk (glassy carbon) and thin film (gold) materials on macroscale 3D objects, including cylinder, cube, and hyperbola-shaped substrate, at high-throughput ($> 10^{-7}$ m^2/s) in standard laboratory setting. Linear features with width of sub-50 nm to a few microns were fabricated with high fidelity and no defects over large areas. We also characterized the feature width and height fabricated by the SWAN lithography. We demonstrated that different feature widths can be obtained by either controlling the diameter of fibers, or by controlling the size of the fiber-substrate contact area. Different feature heights were obtained by controlling the etch time.

- **Study the effect of the electrode surface nanotopography on the biofilm formation and current generation of microbial fuel cells (MFCs)**

Glassy carbon electrodes (GCEs) with nanostructures in a grid pattern of different feature heights of 115 nm and 300 nm and common spacing of 3.1 μm were fabricated and characterized. The GCE with the 300 nm pattern had a current production only slightly higher than the unpatterned GCE with the difference proportional to the surface area increase (10.7%) introduced by patterning. On the other hand, the current density increase for the 115 nm patterned GCE was significant (40%) and was due to the increase of the bacterial attachment density, which was 78% higher than the unpatterned GCE. The electrode biofilm was found to be responsible for most of the current production, since the removal of the planktonic bacteria did not significantly reduce the current. Further, the current density dependency on feature size was maintained over the entire 160 h experiment. In a conclusion, the surface feature size itself has a substantial effect on current production that is independent of the change of the surface area.

- **Develop a biophysical model to predict *Candida albicans* attachment density on nanofiber-textured surfaces**

The total free energy (E_{tot}) of *Candida albicans* adhered to a substrate is comprised of adhesion energy (E_{ad}) and stretching energy (E_{str}), which is dependent on the surface nanostructure geometry (i.e. nanofiber diameter) and configuration (i.e. spacing). A biophysical model was developed to characterize the average total energy of cells adhered over a patterned surface. Though an energy-based approach has previous been employed to describe cell-adhesion on surfaces, herein , for the first time, the combination of adhesion energy and stretching energy is applied in the prediction of the microbial adhesion density trend on nanostructured surfaces. The

model was validated by the population-level cell attachment density of *Candida albicans* on polystyrene (PS) nanofiber coated PS substrate. The highly aligned PS nanofibers with diameters of 0.5 μm -2.0 μm were deposited by the Spinneret-based Tunable Engineering Parameters (STEP) technique. Further, this model was also demonstrated by the application in medical catheters. The attachment density on three different catheters (i.e. polyurethane, latex and silicone) were compared before and after depositing the PS nanofibers, and the results for population density were found to correspond to the simulation results for the total energy.

- ***Candida albicans* yeast seeking of the energetically optical adhesion locations**

We observed an energetically and biologically driven seeking movement of *Candida albicans* yeast to the optimal adhesion location with the minimum total energy. A majority of the cells were retained in the optimal adhesion location after reaching the equilibrium state. This phenomenon was demonstrated by a cell attached on a single fiber or two fibers with different diameters (i.e. 0.5 μm, 1.0 μm, and 2.0 μm). The energy change in different locations should be large enough to drive the cells to adjust the location, thus the cells predominantly adhere to the minimum energy locations on 1.0 μm and 2.0 μm fibers but not on 0.5 μm fibers. Further, this behavior was only observed for live cells, where the UV-treated cells did not adjust the attachment location.

6.2 Future directions

The work presented in this dissertation can be expanded to help solve nanoscience and bioengineering problems of significance. A few possible directions are outlined as below:

1. **Engineering bacteria for higher current production of MFCs**

Chapter 3 has demonstrated the effect of the electrode nanostructures on the bacterial attachment density. The different attachment density could be affected by the different expression of certain proteins on the bacteria surface. If such proteins can be identified, then synthetic biology methods can be taken to increase the levels of the specific protein expression. The planktonic bacteria and the biofilm on different electrodes could be collected and examined by transcriptomic data analysis to identify the differences of certain proteins. This information could guide the design of an engineered bacteria mutant which should have stronger adhesion and higher adhesion density on the MFC electrodes, which may lead to a significantly higher current and power production.

2. Designing highly efficient antifouling biomaterials

Chapter 4 presents a biophysical model that can be utilized to design nanofiber-coated surfaces to reduce the mitigation of *Candida albicans* yeast. However, the efficiency of this design could be improved by changing the geometry of the nanostructures. It has been shown that high aspect ratio nanostructures (e.g. nanotubes) can effectively reduce cell attachment density. So this biophysical model could be modified and improved to study cell adhesion on high aspect ratio nanostructures. The combination of this biophysical model and finite element methods could be applied to describe the large deformation of the cell wall on high aspect ratio nanostructures. Result from this work could be used to guide the design and experimental validation of high aspect ratio surface features.

3. Investigating the effect of the nanostructures on the adhesion strength

This research has shown the effect of the nanostructures on the cell attachment density as well as a single cell optimal adhesion location. This work could be extended by investigating the adhesion strength of a single cell on nanopatterned surfaces. Atomic force microscopy (AFM) could be

utilized to experimentally measure the adhesion force of a single yeast cell on flat surfaces and on nanofiber-coated surfaces. The experimental results would be compared to the simulation results from the biophysical model. In order to test different values of adhesion strength, the surface could also be coated with different polymers to change the surface energy. Also, the adhesion energy of a cell attached on nanofiber-coated surfaces could also be experimentally determined from the force-distance curve of the AFM measurement. These experimental results can be compared to the adhesion energy calculated from the biophysical model, thus confirming the model or suggesting areas for refinement.

References

1. Flemming, H.-C. & Wingender, J. The biofilm matrix. *Nat. Rev. Microbiol.* **8,** 623–633 (2010).
2. Mah, T. F. C. & O'Toole, G. A. Mechanisms of biofilm resistance to antimicrobial agents. *Trends in Microbiology* **9,** 34–39 (2001).
3. O'Toole, G., Kaplan, H. B. & Kolter, R. Biofilm formation as microbial development. *Annu. Rev. Microbiol.* **54,** 49–79 (2000).
4. Davies, D. G. *et al.* The involvement of cell-to-cell signals in the development of a bacterial biofilm. *Science* **280,** 295–298 (1998).
5. Donlan, R. M. Biofilms: Microbial life on surfaces. *Emerging Infectious Diseases* **8,** 881–890 (2002).
6. Verran, J. & Boyd, R. D. The relationship between substratum surface roughness and microbiological and organic soiling: A review. *Biofouling* **17,** 59–71 (2001).
7. Whitehead, K. A. & Verran, J. The Effect of Surface Topography on the Retention of Microorganisms. *Food Bioprod. Process.* **84,** 253–259 (2006).
8. Verran, J., Packer, A., Kelly, P. & Whitehead, K. A. The retention of bacteria on hygienic surfaces presenting scratches of microbial dimensions. *Lett. Appl. Microbiol.* **50,** 258–263 (2010).
9. Whitehead, K. A., Colligon, J. & Verran, J. Retention of microbial cells in substratum surface features of micrometer and sub-micrometer dimensions. *Colloids Surfaces B Biointerfaces* **41,** 129–138 (2005).
10. Kargar, M., Wang, J., Nain, A. S. & Behkam, B. Controlling bacterial adhesion to surfaces using topographical cues: a study of the interaction of Pseudomonas aeruginosa with nanofiber-textured surfaces. *Soft Matter* **8,** 10254–10259 (2012).
11. Chung, K. K. *et al.* Impact of engineered surface microtopography on biofilm formation of Staphylococcus aureus. *Biointerphases* **2,** 89–94 (2007).
12. Hochbaum, A. I. & Aizenberg, J. Bacteria pattern spontaneously on periodic nanostructure arrays. *Nano Lett.* **10,** 3717–3721 (2010).
13. Jeong, H. E., Kim, I., Karam, P., Choi, H. J. & Yang, P. Bacterial recognition of silicon nanowire arrays. *Nano Lett.* **13,** 2864–2869 (2013).
14. Kargar, M., Pruden, A. & Ducker, W. A. Preventing bacterial colonization using colloidal crystals. *J. Mater. Chem. B* **2,** 5962–5971 (2014).
15. Singh, A. V. *et al.* Quantitative characterization of the influence of the nanoscale morphology of nanostructured surfaces on bacterial adhesion and biofilm formation. *PLoS One* **6,** (2011).
16. Ivanova, E. P. *et al.* Natural bactericidal surfaces: Mechanical rupture of pseudomonas aeruginosa cells by cicada wings. *Small* **8,** 2489–2494 (2012).
17. Pogodin, S. *et al.* Biophysical model of bacterial cell interactions with nanopatterned

cicada wing surfaces. *Biophys. J.* **104,** 835–840 (2013).

18. Mitik-Dineva, N. *et al.* Impact of nano-topography on bacterial attachment. *Biotechnol. J.* **3,** 536–544 (2008).
19. Díaz, C., Cortizo, M. C., Schilardi, P. L., Saravia, S. G. G. de & Mele, M. A. F. L. de. Influence of the nano-micro structure of the surface on bacterial adhesion. *Materials Research* **10,** (2007).
20. Hsu, L. C., Fang, J., Borca-Tasciuc, D. A., Worobo, R. W. & Moraru, C. I. Effect of micro- and nanoscale topography on the adhesion of bacterial cells to solid surfaces. *Appl. Environ. Microbiol.* **79,** 2703–2712 (2013).
21. Rizzello, L. *et al.* Impact of nanoscale topography on genomics and proteomics of adherent bacteria. *ACS Nano* **5,** 1865–1876 (2011).
22. Nain, A. S. S. & Wang, J. Polymeric nanofibers: isodiametric design space and methodology for depositing aligned nanofiber arrays in single and multiple layers. *Polym. J.* 1–6 (2013). doi:10.1038/pj.2013.1
23. Nain, A. S., Sitti, M., Jacobson, A., Kowalewski, T. & Amon, C. Dry spinning based spinneret based tunable engineered parameters (STEP) technique for controlled and aligned deposition of polymeric nanofibers. *Macromol. Rapid Commun.* **30,** 1406–1412 (2009).
24. Shalaev, V. M. Optical negative-index metamaterials. *Nat. Photonics* **1,** 41–48 (2007).
25. Wang, X., Summers, C. J. & Wang, Z. L. Large-scale hexagonal-patterned growth of aligned ZnO nanorods for nano-optoelectronics and nanosensor arrays. *Nano Lett.* **4,** 423–426 (2004).
26. Halas, N. J., Lal, S., Chang, W.-S., Link, S. & Nordlander, P. Plasmons in strongly coupled metallic nanostructures. *Chem. Rev.* **111,** 3913–61 (2011).
27. Priolo, F., Gregorkiewicz, T., Galli, M. & Krauss, T. F. Silicon nanostructures for photonics and photovoltaics. *Nat. Nanotechnol.* **9,** 19–32 (2014).
28. Das, J. & Kelley, S. O. Tuning the bacterial detection sensitivity of nanostructured microelectrodes. *Anal. Chem.* **85,** 7333–8 (2013).
29. Zhang, W., Patel, K., Schexnider, A., Banu, S. & Radadia, A. D. Nanostructuring of biosensing electrodes with nanodiamonds for antibody immobilization. *ACS Nano* **8,** 1419–28 (2014).
30. Pisco, M. *et al.* Miniaturized Sensing Probes Based on Metallic Dielectric Crystals Self-Assembled on Optical Fiber Tips. *ACS Photonics* **1,** 917–927 (2014).
31. Aricò, A. S., Bruce, P., Scrosati, B., Tarascon, J.-M. & van Schalkwijk, W. Nanostructured materials for advanced energy conversion and storage devices. *Nat. Mater.* **4,** 366–377 (2005).
32. Castner, D. G. & Ratner, B. D. Biomedical surface science: Foundations to frontiers. *Surf. Sci.* **500,** 28–60 (2002).
33. Smythe, E. J., Dickey, M. D., Whitesides, G. M. & Capasso, F. A technique to transfer metallic nanoscale patterns to small and non-planar surfaces. *ACS Nano* **3,** 59–65 (2009).

34. Lipomi, D. J. *et al.* Patterning the tips of optical fibers with metallic nanostructures using nanoskiving. *Nano Lett.* **11,** 632–6 (2011).

35. Aksu, S. *et al.* Flexible plasmonics on unconventional and nonplanar substrates. *Adv. Mater.* **23,** 4422–4430 (2011).

36. Chanda, D. *et al.* Large-area flexible 3D optical negative index metamaterial formed by nanotransfer printing. *Nat. Nanotechnol.* **6,** 402–407 (2011).

37. Zhang, J., Con, C. & Cui, B. Electron Beam Lithography on Irregular Surfaces Using an Evaporated Resist. *ACS Nano* **8,** 3483–3489 (2014).

38. Han, A., Kuan, A., Golovchenko, J. & Branton, D. Nanopatterning on nonplanar and fragile substrates with ice resists. *Nano Lett.* **12,** 1018–1021 (2012).

39. Paul, K. E., Prentiss, M. & Whitesides, G. M. Patterning spherical surfaces at the two-hundred-nanometer scale using soft lithography. *Adv. Funct. Mater.* **13,** 259–263 (2003).

40. Farshchian, B. *et al.* Soft UV-nanoimprint lithography on non-planar surfaces. *Microelectron. Eng.* **88,** 3287–3292 (2011).

41. Ruchhoeft, P. *et al.* Patterning curved surfaces: Template generation by ion beam proximity lithography and relief transfer by step and flash imprint lithography. *J. Vac. Sci. Technol. B* **17,** (1999).

42. Childs, W. R. & Nuzzo, R. G. Patterning of thin-film microstructures on non-planar substrate surfaces using decal transfer lithography. *Adv. Mater.* **16,** 1323–1327 (2004).

43. Choi, W. M. & Park, O. O. The fabrication of submicron patterns on curved substrates using a polydimethylsiloxane film mould. *Nanotechnology* **15,** 1767–1770 (2004).

44. Li, Z. *et al.* Hybrid nanoimprint-soft lithography with sub-15 nm resolution. *Nano Lett.* **9,** 2306–2310 (2009).

45. Kiema, G. K., Ssenyange, S. & McDermott, M. T. Microfarbrication of Glassy Carbon by Electrochemical Etching. *J. Electrochem. Soc.* **151,** C142–C148 (2004).

46. Duan, X. *et al.* High-Resolution Contact Printing with Chemically Patterned Flat Stamps Fabricated by Nanoimprint Lithography. *Adv. Mater.* **21,** 2798–2802 (2009).

47. Van Dersarl, J. J., Mercanzini, A. & Renaud, P. Integration of 2D and 3D thin film glassy carbon electrode arrays for electrochemical dopamine sensing in flexible neuroelectronic implants. *Adv. Funct. Mater.* **25,** 78–84 (2015).

48. Yao, L. & He, J. Recent progress in antireflection and self-cleaning technology - From surface engineering to functional surfaces. *Prog. Mater. Sci.* **61,** 94–143 (2014).

49. Tu, M. H., Sun, T. & Grattan, K. T. V. LSPR optical fibre sensors based on hollow gold nanostructures. *Sensors Actuators B Chem.* **191,** 37–44 (2014).

50. Barquins, M. Adherence and Rolling Kinetics of a Rigid Cylinder in Contact with a Natural Rubber Surface. *The Journal of Adhesion* **26,** 1–12 (1988).

51. Chaudhury, M. K., Weaver, T., Hui, C. Y. & Kramer, E. J. Adhesive contact of cylindrical lens and a flat sheet. *J. Appl. Phys.* **80,** 30 (1996).

52. Johnson, K. L., Kendall, K. & Roberts, A. D. Surface Energy and the Contact of Elastic Solids. *Proceedings of the Royal Society A: Mathematical, Physical and Engineering*

Sciences **324,** 301–313 (1971).

53. Miller-Chou, B. A. & Koenig, J. L. A review of polymer dissolution. *Progress in Polymer Science (Oxford)* **28,** 1223–1270 (2003).

54. Min, S.-Y. *et al.* Large-scale organic nanowire lithography and electronics. *Nat. Commun.* **4,** 1773 (2013).

55. Bhawalkar, S. P., Qian, J., Heiber, M. C. & Jia, L. Development of a colloidal lithography method for patterning nonplanar surfaces. *Langmuir* **26,** 16662–16666 (2010).

56. Ahn, S. H. & Guo, L. J. High-Speed Roll-to-Roll Nanoimprint Lithography on Flexible Plastic Substrates. *Adv. Mater.* **20,** 2044–2049 (2008).

57. Gates, B. D. *et al.* New approaches to nanofabrication: Molding, printing, and other techniques. *Chemical Reviews* **105,** 1171–1196 (2005).

58. Liddle, J. A. & Gallatin, G. M. Lithography, metrology and nanomanufacturing. *Nanoscale* **3,** 2679–2688 (2011).

59. Manfrinato, V. R. *et al.* Resolution Limits of Electron-Beam Lithography toward the Atomic Scale. *Nano Lett.* **13,** 1555–1558 (2013).

60. Wiley, B. J., Qin, D. & Xia, Y. Nanofabrication at high throughput and low cost. *ACS Nano* **4,** 3554–3559 (2010).

61. Rabaey, K. & Verstraete, W. Microbial fuel cells: Novel biotechnology for energy generation. *Trends in Biotechnology* **23,** 291–298 (2005).

62. Lovley, D. R. Microbial fuel cells: novel microbial physiologies and engineering approaches. *Current Opinion in Biotechnology* **17,** 327–332 (2006).

63. Du, Z., Li, H. & Gu, T. A state of the art review on microbial fuel cells: A promising technology for wastewater treatment and bioenergy. *Biotechnology Advances* **25,** 464–482 (2007).

64. Logan, B. E. & Regan, J. M. Microbial fuel cells--challenges and applications. *Environ. Sci. Technol.* **40,** 5172–5180 (2006).

65. Ieropoulos, I. A., Greenman, J., Melhuish, C. & Horsfield, I. Microbial Fuel Cells for Robotics: Energy Autonomy through Artificial Symbiosis. *ChemSusChem* **5,** 1020–1026 (2012).

66. Logan, B. E. *et al.* Assessment of Microbial Fuel Cell Configurations and Power Densities. *Environ. Sci. Technol. Lett.* **2,** 206–214 (2015).

67. Hou, J., Liu, Z., Yang, S. & Zhou, Y. Three-dimensional macroporous anodes based on stainless steel fiber felt for high-performance microbial fuel cells. *J. Power Sources* **258,** 204–209 (2014).

68. Chen, S. *et al.* Electrospun and solution blown three-dimensional carbon fiber nonwovens for application as electrodes in microbial fuel cells. *Energy & Environmental Science* **4,** 1417 (2011).

69. Ketep, S. F., Bergel, A., Calmet, A. & Erable, B. Stainless steel foam increases the current produced by microbial bioanodes in bioelectrochemical systems. *Energy Environ. Sci.* **7,** 1633–1637 (2014).

70. Liu, M., Zhou, M., Yang, H., Ren, G. & Zhao, Y. Titanium dioxide nanoparticles modified three dimensional ordered macroporous carbon for improved energy output in microbial fuel cells. *Electrochim. Acta* **190,** 463–470 (2016).

71. Tang, J., Yuan, Y., Liu, T. & Zhou, S. High-capacity carbon-coated titanium dioxide core-shell nanoparticles modified three dimensional anodes for improved energy output in microbial fuel cells. *J. Power Sources* **274,** 170–176 (2015).

72. Yu, Y.-Y., Xian Guo, C., Yong, Y.-C., Ming Li, C. & Song, H. Nitrogen doped carbon nanoparticles enhanced extracellular electron transfer for high-performance microbial fuel cells anode. *Chemosphere* **140,** 26–33 (2015).

73. Erbay, C. *et al.* Control of geometrical properties of carbon nanotube electrodes towards high-performance microbial fuel cells. *J. Power Sources* **280,** 347–354 (2015).

74. Yazdi, A. A. *et al.* Carbon nanotube modification of microbial fuel cell electrodes. *Biosens. Bioelectron.* **85,** 536–552 (2016).

75. Mink, J. E. & Hussain, M. M. Sustainable design of high-performance microsized microbial fuel cell with carbon nanotube anode and air cathode. *ACS Nano* **7,** 6921–6927 (2013).

76. Mink, J. E., Rojas, J. P., Logan, B. E. & Hussain, M. M. Vertically grown multiwalled carbon nanotube anode and nickel silicide integrated high performance microsized (1.25 μl) microbial fuel cell. *Nano Lett.* **12,** 791–795 (2012).

77. Lamp, J. L. *et al.* Flame synthesis of carbon nanostructures on stainless steel anodes for use in microbial fuel cells. *J. Power Sources* **196,** 5829–5834 (2011).

78. Yuan, H. & He, Z. Graphene-modified electrodes for enhancing the performance of microbial fuel cells. *Nanoscale* **7,** 7022–7029 (2015).

79. Zhao, S. *et al.* Three-dimensional graphene/Pt nanoparticle composites as freestanding anode for enhancing performance of microbial fuel cells. *Sci. Adv.* **1,** (2015).

80. Tang, J., Chen, S., Yuan, Y., Cai, X. & Zhou, S. In situ formation of graphene layers on graphite surfaces for efficient anodes of microbial fuel cells. *Biosens. Bioelectron.* **71,** 387–395 (2015).

81. Edwards Rutenberg, A. D., K. J. Microbial response to surface microtopography: the role of metabolism in localized mineral dissolution. *Chem Geol* **180,** 19–32 (2001).

82. Ye, Z., Nain, A. S. & Behkam, B. Spun-wrapped aligned nanofiber (SWAN) lithography for fabrication of micro/nano-structures on 3D objects. *Nanoscale* **8,** 12780–12786 (2016).

83. Marsili, E. *et al.* Shewanella secretes flavins that mediate extracellular electron transfer. *Proc. Natl. Acad. Sci. U. S. A.* **105,** 3968–3973 (2008).

84. Daniel Baron Dan Coursolle, Jeffrey A. Gralnick and Daniel R. Bond, E. L. *et al.* Electrochemical Measurement of Electron Transfer Kinetics by Shewanella oneidensis MR-1. *J. Biol. Chem.* **284,** 28865–28873 (2009).

85. Roh, Y. *et al.* Metal reduction and iron biomineralization by a psychrotolerant Fe(III)-reducing bacterium, Shewanella sp strain PV-4. *Appl. Environ. Microbiol.* **72,** 3236–3244 (2006).

86. Murtey, M. Das & Ramasamy, P. in *Modern Electron Microscopy in Physical and Life*

Sciences (2016). doi:10.5772/61720

87. Kotloski, N. J. & Gralnick, J. A. Flavin electron shuttles dominate extracellular electron transfer by Shewanella oneidensis. *MBio* **4,** (2013).

88. Picioreanu, C., Head, I. M., Katuri, K. P., van Loosdrecht, M. C. M. & Scott, K. A computational model for biofilm-based microbial fuel cells. *Water Res.* **41,** 2921–2940 (2007).

89. Whitehead Colligon, J., Verran, J., K. A. Retention of microbial cells in substratum surface features of micrometer and sub-micrometer dimensions. *Colloids Surfaces B Biointerfaces* **41,** 129–138 (2005).

90. Hochbaum, A. I. & Aizenberg, J. Bacteria pattern spontaneously on periodic nanostructure arrays. *Nano Lett.* **10,** 3717–3721 (2010).

91. Edwards, K. J. & Rutenberg, A. D. Microbial response to surface microtopography: the role of metabolism in localized mineral dissolution. *Chem. Geol.* **180,** 19–32 (2001).

92. Dobretsov, S., Dahms, H.-U. & Qian, P.-Y. Inhibition of biofouling by marine microorganisms and their metabolites. *Biofouling* **22,** 43–54 (2006).

93. Kumar, C. G. & Anand, S. K. Significance of microbial biofilms in food industry: a review. *Int. J. Food Microbiol.* **42,** 9–27 (1998).

94. Francolini, I. & Donelli, G. Prevention and control of biofilm-based medical-device-related infections. *FEMS Immunol. Med. Microbiol.* **59,** 227–238 (2010).

95. Marchetti, A. & Rossiter, R. Economic burden of healthcare-associated infection in US acute care hospitals: societal perspective. *J. Med. Econ.* **16,** 1399–1404 (2013).

96. Mah, T. F. C. & O'Toole, G. A. Mechanisms of biofilm resistance to antimicrobial agents. *Trends in Microbiology* **9,** 34–39 (2001).

97. Renner, L. D. & Weibel, D. B. Physicochemical regulation of biofilm formation. *MRS Bull.* **36,** 347–355 (2011).

98. Brzozowska, A. M. *et al.* Biomimicking micropatterned surfaces and their effect on marine biofouling. *Langmuir* **30,** 9165–9175 (2014).

99. Chung, K. K. *et al.* Impact of engineered surface microtopography on biofilm formation of *Staphylococcus aureus*. *Biointerphases* **2,** 89–94 (2007).

100. Ivanova, E. P. *et al.* Natural bactericidal surfaces: Mechanical rupture of pseudomonas aeruginosa cells by cicada wings. *Small* **8,** 2489–2494 (2012).

101. Ye, Z., Ellis, M. W., Nain, A. S. & Behkam, B. Effect of electrode sub-micron surface feature size on current generation of Shewanella oneidensis in microbial fuel cells. *J. Power Sources* **347,** 270–276 (2017).

102. Hermansson, M. The DLVO theory in microbial adhesion. *Colloids and Surfaces B: Biointerfaces* **14,** 105–119 (1999).

103. Zita, A. & Hermansson, M. Effects of ionic strength on bacterial adhesion and stability of flocs in a wastewater activated sludge system. *Appl. Environ. Microbiol.* **60,** 3041–3048 (1994).

104. Rijnaarts, H. H. M., Norde, W., Lyklema, J. & Zehnder, A. J. B. DLVO and steric

contributions to bacterial deposition in media of different ionic strengths. *Colloids Surfaces B Biointerfaces* **14,** 179–195 (1999).

105. Bolster, C. H., Mills, A. L., Hornberger, G. M. & Herman, J. S. Effect of surface coatings, grain size, and ionic strength on the maximum attainable coverage of bacteria on sand surfaces. *J. Contam. Hydrol.* **50,** 287–305 (2001).

106. Truesdail, S. E., Lukasik, J., Farrah, S. R., Shah, D. O. & Dickinson, R. B. Analysis of bacterial deposition on metal (hydr)oxide-coated sand filter media. *J. Colloid Interface Sci.* **203,** 369–78 (1998).

107. Chang, Y.-I. & Chang, P.-K. The role of hydration force on the stability of the suspension of Saccharomyces cerevisiae–application of the extended DLVO theory. *Colloids Surfaces A Physicochem. Eng. Asp.* **211,** 67–77 (2002).

108. Claesson, P., Carmona-Ribeiro, A. M. & Kurihara, K. Dihexadecyl phosphate monolayers: intralayer and interlayer interactions. *J. Phys. Chem.* **93,** 917–922 (1989).

109. Absolom, D. R. *et al.* Surface thermodynamics of bacterial adhesion. *Appl. Environ. Microbiol.* **46,** 90–97 (1983).

110. Busscher, H. J. *et al.* Measurement of the surface free energy of bacterial cell surfaces and its relevance for adhesion. *Appl. Environ. Microbiol.* **48,** 980–983 (1984).

111. Bayoudh, S., Othmane, A., Mora, L. & Ben Ouada, H. Assessing bacterial adhesion using DLVO and XDLVO theories and the jet impingement technique. *Colloids Surfaces B Biointerfaces* **73,** 1–9 (2009).

112. Vilinska, a. & Rao, K. H. Surface Thermodynamics and Extended DLVO Theory of Acidithiobacillus ferrooxidans Cells Adhesion on Pyrite and Chalcopyrite. *Open Colloid Sci. J.* **2,** 1–14 (2009).

113. van Oss, C. J. Hydrophobicity of biosurfaces - Origin, quantitative determination and interaction energies. *Colloids Surfaces B Biointerfaces* **5,** 91–110 (1995).

114. Pogodin, S. *et al.* Biophysical model of bacterial cell interactions with nanopatterned cicada wing surfaces. *Biophys. J.* **104,** 835–840 (2013).

115. Decuzzi, P. & Ferrari, M. Modulating cellular adhesion through nanotopography. *Biomaterials* **31,** 173–179 (2010).

116. Mathé, L. & Van Dijck, P. Recent insights into Candida albicans biofilm resistance mechanisms. *Curr. Genet.* **59,** 251–264 (2013).

117. Finkel, J. S. & Mitchell, A. P. Genetic control of Candida albicans biofilm development. *Nat. Rev. Microbiol.* **9,** 109–18 (2011).

118. Douglas, L. J. Candida biofilms and their role in infection. *Trends Microbiol.* **11,** 30–36 (2003).

119. Seifert, U. & Lipowsky, R. Adhesion of vesicles. *Phys. Rev. A* **42,** 4768–4771 (1990).

120. Deserno, M. & Gelbart, W. Adhesion and Wrapping in Colloid− Vesicle Complexes. *J. Phys. Chem. B* 5543–5552 (2002). doi:10.1021/jp0138476

121. Chandra, J. *et al.* Biofilm formation by the fungal pathogen Candida albicans: Development, architecture, and drug resistance. *J. Bacteriol.* **183,** 5385–5394 (2001).

122. Sundstrom, P. Adhesins in Candida albicans. *Current Opinion in Microbiology* **2,** 353–357 (1999).

123. Comyn, J. *Adhesion Science*. (The Royal Society of Chemistry, 1997). doi:10.1039/9781847550064

124. Dietrich, C., Angelova, M. & Pouligny, B. Adhesion of Latex Spheres to Giant Phospholipid Vesicles: Statics and Dynamics. *J. Phys. II* **7,** 1651–1682 (1997).

125. Smith, A. E., Zhang, Z., Thomas, C. R., Moxham, K. E. & Middelberg, a P. The mechanical properties of Saccharomyces cerevisiae. *Proc. Natl. Acad. Sci. U. S. A.* **97,** 9871–4 (2000).

126. Fradin, C., Satsoura, D. & Andrews, D. W. *Biomembrane Frontiers: Nanostructures, Models, and the Design of Life. Proteins* **1252,** (2009).

127. Chandra, J., Mukherjee, P. K. & Ghannoum, M. a. In vitro growth and analysis of Candida biofilms. *Nat. Protoc.* **3,** 1909–1924 (2008).

128. Dague, E. *et al.* An atomic force microscopy analysis of yeast mutants defective in cell wall architecture. *Yeast* **27,** 673–84 (2010).

129. Ene, I. V. *et al.* Host carbon sources modulate cell wall architecture, drug resistance and virulence in a fungal pathogen. *Cell. Microbiol.* **14,** 1319–1335 (2012).

130. W. Helfrich. Elastic Properties of Lipid Bilayers—Theory and Possible Experiments. *Zeitschrift fur Naturforsch. Tl. C Biochem. Biophys. Biol. Virol.* **28,** 693–703 (1973).

131. Kachalo, S., Naveed, H., Cao, Y., Zhao, J. & Liang, J. Mechanical model of geometric cell and topological algorithm for cell dynamics from single-cell to formation of monolayered tissues with pattern. *PLoS One* **10,** e0126484 (2015).

132. Conrad, J. C. Physics of bacterial near-surface motility using flagella and type IV pili: Implications for biofilm formation. *Res. Microbiol.* **163,** 619–629 (2012).

133. Spormann, A. M. Gliding motility in bacteria: insights from studies of Myxococcus xanthus. *Microbiol. Mol. Biol. Rev.* **63,** 621–41 (1999).

134. Friedlander, R. S. *et al.* Bacterial flagella explore microscale hummocks and hollows to increase adhesion. *Proc. Natl. Acad. Sci. U. S. A.* **110,** 5624–9 (2013).

135. Gow, N. a. R., van de Veerdonk, F. L., Brown, A. J. P. & Netea, M. G. Candida albicans morphogenesis and host defence: discriminating invasion from colonization. *Nat. Rev. Microbiol.* **10,** 112–122 (2011).

136. Miyake, Y. *et al.* Antifungal drugs effect adherence of Candida albicans to acrylic surfaces by changing the zeta-potential of fungal cells. *FEMS Microbiol. Lett.* **69,** 211–214 (1990).

137. Song, L. *et al.* Nanoscopic vibrations of bacteria with different cell-wall properties adhering to surfaces under flow and static conditions. *ACS Nano* **8,** 8457–8467 (2014).

138. Pelling, A. E., Sehati, S., Gralla, E. B., Valentine, J. S. & Gimzewski, J. K. Local nanomechanical motion of the cell wall of Saccharomyces cerevisiae. *Science* **305,** 1147–1150 (2004).